



**UNIVERSIDADE ESTADUAL DE CAMPINAS**

**INSTITUTO DE QUÍMICA**

**BRUNO MORANDI PIRES**

**CYANIDOFERRATE-BASED COORDINATION POLYMERS AS  
ELECTROCATALYSTS FOR HYDROGEN PEROXIDE/DIOXYGEN REDUCTION  
AND WATER OXIDATION**

**POLÍMEROS DE COORDENAÇÃO BASEADOS EM CIANIDOFERRATOS  
COMO ELETROCATALISADORES PARA REDUÇÃO DE PERÓXIDO DE  
HIDROGÊNIO/OXIGÊNIO E OXIDAÇÃO DE ÁGUA**

**CAMPINAS**

**2018**

**BRUNO MORANDI PIRES**

**CYANIDOFERRATE-BASED COORDINATION POLYMERS AS  
ELECTROCATALYSTS FOR HYDROGEN PEROXIDE/DIOXYGEN REDUCTION  
AND WATER OXIDATION**

**POLÍMEROS DE COORDENAÇÃO BASEADOS EM CIANIDOFERRATOS  
COMO ELETROCATALISADORES PARA REDUÇÃO DE PERÓXIDO DE  
HIDROGÊNIO/OXIGÊNIO E OXIDAÇÃO DE ÁGUA**

Tese de Doutorado apresentada ao Instituto de Química da  
Universidade Estadual de Campinas como parte dos requisitos  
exigidos para a obtenção do título de Doutor em Ciências

Doctor's Thesis presented to the Institute of Chemistry of the  
University of Campinas as part of the requirements to obtain the title  
of Doctor in Sciences.

**Supervisor: Prof. Dr. Juliano Alves Bonacin**

**ESTE EXEMPLAR CORRESPONDE À VERSÃO FINAL DA TESE DEFENDIDA PELO  
ALUNO BRUNO MORANDI PIRES E ORIENTADA PELO PROF. DR. JULIANO ALVES  
BONACIN**

**CAMPINAS**

**2018**

Agência(s) de fomento e nº(s) de processo(s): CNPq, 153300/2014-0  
ORCID: <https://orcid.org/0000-0001-7208-1119>

Ficha catalográfica  
Universidade Estadual de Campinas  
Biblioteca do Instituto de Química  
Camila Barleta Fullin - CRB 8462

P665c Pires, Bruno Morandi, 1989-  
Cyanidoferrate-based coordination polymers as electrocatalysts for hydrogen peroxide/dioxygen reduction and water oxidation / Bruno Morandi Pires. – Campinas, SP : [s.n.], 2018.

Orientador: Juliano Alves Bonacin.  
Tese (doutorado) – Universidade Estadual de Campinas, Instituto de Química.

1. Cianidoferratos. 2. Azul da Prússia. 3. Reação de desprendimento de oxigênio. 4. Reação de redução de oxigênio. 5. Eletrocatalise. I. Bonacin, Juliano Alves, 1980-. II. Universidade Estadual de Campinas. Instituto de Química. III. Título.

#### Informações para Biblioteca Digital

**Título em outro idioma:** Polímeros de coordenação baseados em cianidoferratos como eletrocatalisadores para redução de peróxido de hidrogênio/oxigênio e oxidação de água

**Palavras-chave em inglês:**

Cyanidoferrates

Prussian blue

Oxygen evolution reaction

Oxygen reduction reaction

Electrocatalysis

**Área de concentração:** Química Inorgânica

**Titulação:** Doutor em Ciências

**Banca examinadora:**

Juliano Alves Bonacin [Orientador]

Raphael Nagao de Sousa

Paulo Cesar de Sousa Filho

Vitor de Moraes Zamarion

Pedro Henrique Cury Camargo

**Data de defesa:** 10-08-2018

**Programa de Pós-Graduação:** Química

## **BANCA EXAMINADORA**

Prof. Dr. Juliano Alves Bonacin (Orientador)

Prof. Dr. Raphael Nagao de Sousa (IQ-UNICAMP)

Prof. Dr. Paulo Cesar de Sousa Filho (IQ-UNICAMP)

Prof. Dr. Vitor de Moraes Zamarion (IQ-USP-SP)

Prof. Dr. Pedro Henrique Cury Camargo (IQ-USP-SP)

A Ata da defesa com as respectivas assinaturas dos membros encontra-se no processo de vida acadêmica do(a) aluno(a).

Este exemplar corresponde à redação final da Tese de Doutorado defendida pelo(a) aluno(a) **BRUNO MORANDI PIRES**, aprovada pela Comissão Julgadora em 10 de agosto de 2018.

*“Se você quiser  
Se você se esforçar  
Se você treinar  
Se você entrar de cabeça  
Se você se concentrar  
Nada garante que você vai conseguir.”*

Craque Daniel – Falha de Cobertura (2018)

## **Agradecimentos**

Ao meu orientador, Prof. Juliano por todo meu período de pós-graduação, pelas discussões em alto nível e por me incentivar sempre a fazer pesquisa de qualidade.

Aos professores André Formiga, Diego dos Santos e Pedro Corbi, pela convivência e discussões no laboratório.

Aos colegas do grupo: Kalil, Márcio, Pãmyla e Vera pela amizade, pelos trabalhos em equipe e pela união que fez toda a diferença durante este período.

Aos colegas de laboratório: Acácia, Adriana, Anna Karla, Carlos, Dayane, Diego, Douglas, Júlia, Luis, Naheed, Marcos Alberto, Marcos Ribeiro, Mariana, Renan e Raphael pela amizade e pelos ótimos momentos no laboratório.

Aos colegas de Campinas: Ana Thereza, Cecília, Igor, Lucas, Nina, Sergio, Thiago e Victor pela amizade e pelos bons momentos de diversão.

To Stephan for the short but very fruitful stay at Unicamp and for sharing a lot of his experiences with our group.

To my colleagues from ICIQ, specially the Galan's group, for the great time I had in Tarragona and for being exemplary hosts.

À minha família, em especial meu pai Pedro, minha mãe Sueli e meu irmão Vitor, pelo apoio e compreensão desde sempre.

À Marjorie por estar ao meu lado durante essa jornada, por entender esse meu jeito de viver e me ver caminhando sob o sol. Sempre unidos, vamos triunfar!

Ao CNPq pela bolsa concedida.

## RESUMO

Polímeros de coordenação eletroativos representam uma interessante opção de uso em sistemas de conversão de energia, processos eletrocatalíticos e sensores eletroquímicos. Um exemplo desta classe de materiais é o azul da Prússia, que possui propriedades eletroquímicas e eletrocromicas amplamente estudadas e que é conhecido como enzima peroxidase artificial devido à sua capacidade de reduzir peróxido de hidrogênio. Alguns estudos também mostram que este material também tem atividade na redução de oxigênio (ORR). Além disso, análogos de azul da Prússia baseados em cobalto têm atividade quando aplicados na reação de desprendimento de oxigênio (OER), inclusive em soluções neutras, mantendo ótima estabilidade após 100h de utilização. Dessa forma, polímeros de coordenação aparecem como uma opção para atender às necessidades de custo-benefício destes processos eletrocatalíticos. Uma estratégia para melhorar o desempenho destes materiais é aumentar o número de sítios catalíticos em suas estruturas, o que pode ser feito através de defeitos estruturais e diminuindo sua cristalinidade. Essa estratégia pode ser suficiente para aumentar a densidade de corrente produzida pelo material em baixos valores de sobrepotencial. Tipicamente, o azul da Prússia e seus análogos são produzidos a partir de hexacianidoferratos, mas uma maneira interessante é obter estes polímeros de coordenação utilizando como precursores complexos do tipo pentacianidoferrato, considerando que diferentes ligantes que constituem esses complexos podem ser introduzidos na estrutura do polímero e produzir defeitos estruturais. Essas modificações mantêm muitas das propriedades do polímero original e são capazes de introduzir novas características, além de possibilitar a modulação das mesmas de acordo com o ligante escolhido.

Neste projeto foram estudadas as propriedades de polímeros de coordenação produzidos a partir de complexos cianidoferratos aplicados em diversos dispositivos eletroquímicos. A primeira parte dos estudos foi destinada ao estudo da redução eletroquímica de peróxido de hidrogênio utilizando um substrato de FTO modificado com azul da Prússia preparado a partir de um complexo pentacianidoferrato. Este mesmo precursor foi utilizado em conjunto com nanopartículas de ouro em estudos de redução eletroquímica de oxigênio. Na segunda parte deste trabalho, foi investigada a influência do caráter aceptor/doador de ligantes dos pentacianidoferratos quando aplicados à reação de oxidação de água. Os resultados

mostram que um análogo de azul da Prússia produzido a partir de um pentacianidoferrato apresentou um incremento de sua área eletroativa e atividade em pH neutro. Por último, foi avaliada a influência destes mesmos ligantes em um sistema fotoeletroquímico baseado em análogos de azul da Prússia e vanadato de bismuto aplicado à reação de oxidação da água. Os resultados mostram que ligantes mais doadores proporcionam maiores valores de fotocorrente e que a natureza dos mesmos influencia diretamente nas propriedades de transferência eletrônica destes materiais.

## ABSTRACT

Electroactive coordination polymers (ECP) appear as an alternative for use in energy conversion, electrocatalytic processes, and electrochemical sensing. One example is Prussian blue (PB), which is a widely used material with well-known electrochemical and electrochromic properties, known as artificial peroxidase due to its ability to reduce hydrogen peroxide. Some studies have also shown that PB has activity towards oxygen reduction (ORR), and the mechanism involved has already been described. Additionally, some cobalt-based PB analogs have shown activity in oxygen evolution reaction (OER) in neutral solutions with long-term stability for periods higher than 100h in neutral conditions. Thus, electroactive coordination polymers could match the necessity of cost-effectiveness of electrocatalytic processes. A strategy to increase the number of active sites on the material surface is introducing defects and lowering the crystallinity, since in conventional synthesis, Co sites are connected to six cyanide ligands. This would increase the current density at lower overpotentials. Typically, PB and its analogs are produced using hexacyanidometallates, but another interesting strategy to obtain ECPs is using pentacyanidoferrates as precursors of PB-like structures, since defects are introduced in the material framework due to the presence of different ligands. These modifications keep the electrochemical activity of the catalyst and enables the modulation its properties, which showed dependence of the nature of the ligand in pentacyanidoferrate moiety.

In this project, the properties of coordination polymers produced from cyanoferrate complexes in electrochemical devices were studied. Firstly, we focused on studying electrochemical reduction of hydrogen peroxide by an FTO substrate modified with PB films. In addition, using the same precursor, we observed the formation of PB on the surface of gold nanoparticles and consequently its capacity to promote oxygen electrochemical reduction reactions. In the second part, we have proposed an investigation of the influence of acceptor-donor character of different ligands on the properties of electroactive coordination polymer used as a catalyst in water oxidation reaction. Thus, we evaluated the effect of a Prussian blue analog produced using a pentacyanidoferrate complex as precursor towards the electrochemical oxidation of water in neutral conditions. The results showed that a considerable increment of the electroactive area was observed, which can explain the

higher current values obtained when compared to traditional cobalt hexacyanidoferrate. The last approach was the use of a photoelectrochemical system prepared with the Prussian blue analogs and bismuth vanadate as catalysts for water oxidation. The results showed that the pentacyanidoferrate containing the most donor ligand was able to produce higher photocurrents. Also, the ligands influenced in the charge transfer properties of the materials.

## FIGURES LIST

Figure 1. Simplified scheme showing the possible structures adopted by coordination polymers <sup>[4]</sup> . .....	20
Figure 2. Crystal structures of a) Insoluble and b) soluble Prussian blue <sup>[1]</sup> . .....	20
Figure 3. Spin configurations of iron atoms in the PB structure <sup>[8]</sup> . .....	21
Figure 4. General scheme of a Prussian blue-based electrochemical biosensor <sup>[15]</sup> . ..	23
Figure 5. A) Structure of PB and B) proposed structure of PB-mpz, with hydrogens omitted <sup>[27]</sup> . .....	25
Figure 6. Synergistic mechanism of ORR promoted by a PB/Pt system <sup>[29]</sup> . .....	26
Figure 7. Adsorption models proposed for the oxygen molecule on the surface of a (111) face of face centered cubic transition metal catalyst <sup>[31]</sup> . .....	28
Figure 8. Possible tautomers for the ptt molecule. ....	34
Figure 9. Infrared spectra of Na <sub>3</sub> [Fe(CN) <sub>5</sub> (ptt)] and free ptt ligand. ....	35
Figure 10. Comparison of the UV-Vis spectrum of [Fe(CN) <sub>5</sub> (ptt)] <sup>3-</sup> with the precursor complex [Fe(CN) <sub>5</sub> NH <sub>3</sub> ] <sup>3-</sup> . ....	38
Figure 11. Cyclic voltammetry of ptt aqueous solution at different scan rates using KCl 0.1 mol L <sup>-1</sup> as supporting electrolyte. ....	39
Figure 12. A) Cyclic voltammograms of 2.0 x 10 <sup>-3</sup> mol L <sup>-1</sup> [Fe(CN) <sub>5</sub> (ptt)] <sup>3-</sup> aqueous solutions containing KCl 0.1 mol L <sup>-1</sup> as supporting electrolyte at different scan rates. B) Current peaks of the iron redox process as a function of the square root of the scan rate. ....	40
Figure 13. Cyclic voltammeteries of [Fe(CN) <sub>5</sub> (ptt)] <sup>3-</sup> in Britton-Robinson buffer solution in different pH values. Scan rate 50 mv.s <sup>-1</sup> . .....	41
Figure 14. Cyclic voltammograms of FTO / PB modified electrodes using A) potassium ferricyanide and B) FTO / ECP-Fe(III)/Fe(II)/ptt as precursors in aqueous HCl 0.1 mol.L <sup>-1</sup> . Scan rate 100 mV.s <sup>-1</sup> . Supporting electrolyte KCl 0.1 mol.L <sup>-1</sup> . .....	42
Figure 15. SEM micrograph of FTO, FTO modified by PB and ECP-Fe(III)/Fe(II)/ptt	44
Figure 16. Stability of FTO electrodes modified with A) PB and B) ECP-Fe(III)/Fe(II)/ptt after 50 cycles in HCl 0.1 mol L <sup>-1</sup> and KCl 0.1 mol L <sup>-1</sup> . ....	45
Figure 17. Normalized UV-Vis spectra of PB and ECP-Fe(III)/Fe(II)/ptt in water.....	46
Figure 18. FTIR spectra of PB and ECP-Fe(III)/Fe(II)/ptt. ....	46

Figure 19. Basic structure proposed for ECP-Fe(III)/Fe(II)/ptt, with hydrogens omitted for simplification. Gray: carbon; Blue: nitrogen; Red: iron; yellow: sulfur. ....	48
Figure 20. Amperometric response of A) FTO/PB and C) FTO/ECP-Fe(III)/Fe(II)/ptt electrodes after successive additions of $5.0 \times 10^{-3} \text{ mol L}^{-1}$ hydrogen peroxide stock solution. The analytical curves obtained from the two measurements are presented in figures B) and D), for FTO/PB ( $R^2 = 0.986$ ) and FTO/ ECP-Fe(III)/Fe(II)/ptt electrodes ( $R^2 = 0.996$ ), respectively. ....	49
Figure 21. Extinction spectrum of gold nanoparticles produced using the Turkevich method. ....	50
Figure 22. Cyclic voltammetry of FTO / AuNP/ ECP-Fe(III)/Fe(II)/ptt electrode produced by an immersion method in KCl $0.1 \text{ mol L}^{-1}$ aqueous solution. Scan rate: $100 \text{ mV.s}^{-1}$ . ....	51
Figure 23. Electrochemical oxygen reduction by A) FTO; B) FTO + AuNP; C) FTO + AuNP + ECP-Fe(III)/Fe(II)/ptt; D) Comparison among the electrodes. Voltammograms obtained in KCl $0.1 \text{ mol L}^{-1}$ and scan rate of $50 \text{ mV.s}^{-1}$ . ....	52
Figure 24. A) Stability of FTO/AuNP/ ECP-Fe(III)/Fe(II)/ptt electrodes used for oxygen reduction after successive measurements (alternating nitrogen and oxygen purge). Inset: variation of peak current densities after each measurement. Scan rate: $50 \text{ mV.s}^{-1}$ ; B) Stability of FTO/AuNP ECP-Fe(III)/Fe(II)/ptt electrodes used for oxygen reduction after 50 successive cycles. Inset: variation of peak current density after each cycle. Scan rate: $50 \text{ mV.s}^{-1}$ . ....	53
Figure 25. Plot of overpotentials as a function of the current densities, also known as Tafel plots. Higher slope region indicates worst kinetics, since the increment in current with the potential will be lower at a given overpotential <sup>[56]</sup> . ....	59
Figure 26. Mechanism of water oxidation using a cobalt oxide catalyst <sup>[59]</sup> . ....	63
Figure 27. Obtention of the cobalt hexacyanidoferrate from a cobalt hydroxide layer <sup>[73]</sup> . ....	65
Figure 28. Proposed mechanism for water oxidation using cobalt-based PBAs <sup>[75]</sup> . ....	66
Figure 29. Structure of a PBA catalyst prepared from immobilization of a pentacyanidoferrate in a PVP framework <sup>[76]</sup> . ....	67
Figure 30. Optimized structure of the complex $[\text{Fe}(\text{CN})_5(\text{isn})]^{4-}$ modeled by DFT calculations. Iron is shown in orange, carbons in gray, nitrogens in blue, oxygens in red and hydrogens in white <sup>[26]</sup> . ....	68

Figure 31. Cyclic voltammograms of bare and modified FTO substrates in PBS pH 7.1, $\text{KNO}_3$ 1.0 mol.L <sup>-1</sup> . Scan rate 50mV.s <sup>-1</sup> .....	72
Figure 32. Cyclic voltammograms of A) FTO/CoHCF and B) FTO/CoFeisn electrodes at different scan rates in PBS pH 7.1 and $\text{KNO}_3$ 1.0 mol.L <sup>-1</sup> .....	74
Figure 33. Proposed structure of CoFeisn deposited on FTO substrate. Fe: purple; Co: light blue; N: blue; C: gray; O: red. ....	74
Figure 34. Cyclic voltammograms of A) FTO/CoHCF and B) FTO/CoFeisn electrodes in different pH phosphate solutions. Scan rate 50 mV.s <sup>-1</sup> . ....	75
Figure 35. A) Nyquist plots obtained for the FTO modified substrates and equivalent circuits obtained for B) bare FTO, C) FTO/CoHCF and D) FTO/CoFeisn. ....	76
Figure 36. Tafel plots of the modified FTO substrates applied to water oxidation. ....	77
Figure 37. FTIR spectra of the modified substrates before and after application in electrochemical water oxidation. ....	78
Figure 38. XPS spectrum of the Fe 2p range of FTO/CoHCF electrode before and after water electrolysis. ....	79
Figure 39. XPS spectrum of the Co 2p range of FTO/CoHCF electrode before and after water electrolysis. ....	79
Figure 40. XPS spectrum of the Fe 2p range of FTO/CoFeisn electrode before and after water electrolysis. ....	80
Figure 41. XPS spectrum of the Co 2p range of FTO/CoFeisn electrode before and after water electrolysis. ....	80
Figure 42. SEM micrographs and EDS analysis of FTO/CoHCF electrode. ....	81
Figure 43. SEM micrographs and EDS analysis of FTO/CoFeisn electrode .....	82
Figure 44. Micrographs of the substrates used in the electrocatalytic experiments. The substrates FTO/CoHCF and FTO/CoFeisn were evaluated before (A and C) and after the catalysis (B and D), respectively. ....	83
Figure 45. (A) Oxygen evolution and theoretical faradaic production at $j = 0.2 \text{ mA/cm}^2$ . (B) Chronopotentiometry of FTO/CoFeisn with $j = 0.2 \text{ mA.cm}^{-2}$ at PBS pH 7.1 containing 1 mol.L <sup>-1</sup> $\text{KNO}_3$ as supporting electrolyte. ....	84
Figure 46. Sustainable hydrogen fuel community based on PEC systems <sup>[84]</sup> .....	86
Figure 47. Representation of a PEC cell based on a n-type semiconductor and a metal counter electrode <sup>[83]</sup> .....	88
Figure 48. Main processes required for photocatalytic water splitting <sup>[54]</sup> . ....	89

Figure 49. Possible crystal structures of bismuth vanadate prepared in laboratory. a) Tetragonal scheelite. b) Zircon-type structure. (Red: V; purple Bi; Gray: O) <sup>[86]</sup> . .....	90
Figure 50. Band structure proposed for bismuth vanadate in different crystal systems <sup>[86]</sup> . .....	90
Figure 51. The influence of side illumination of FTO/BiVO <sub>4</sub> modified substrates, indicating the difference of the distance that electrons and holes must travel <sup>[86]</sup> . .....	92
Figure 52. Simplified diagram of the photocatalytic process using an FTO/BiVO <sub>4</sub> /CoFe modified substrate <sup>[82]</sup> . .....	94
Figure 53. Structures of the pentacyanidoferrates used as precursors of ECPs. A) [Fe(CN) <sub>5</sub> NH <sub>3</sub> ] <sup>3-</sup> , B) [Fe(CN) <sub>5</sub> (isn)] <sup>4-</sup> , C) [Fe(CN) <sub>5</sub> (mpz)] <sup>2-</sup> . .....	95
Figure 54. SEM microscopies of FTO/BiVO <sub>4</sub> substrates modified with different cyanidoferrate coordination polymers at 20000 X magnification. ....	99
Figure 55. Cyclic voltammograms of FTO/BiVO <sub>4</sub> substrates in the dark and under illumination (1 sun), in PBS pH 7.1. Scan rate 50 mV.s <sup>-1</sup> . ....	101
Figure 56. Cyclic voltammetry under illumination (1 sun) of the FTO substrates modified with BiVO <sub>4</sub> and Prussian blue analogs obtained using different cyanidoferrate precursors. Scan rate 50 mV.s <sup>-1</sup> in PBS buffer pH = 7.1. ....	102
Figure 57. LSV of the modified FTO substrates under illumination. Scan rate 1 mV.s <sup>-1</sup> . .....	102
Figure 58. Linear sweep voltammetry of modified FTO substrates under chopped light (T = 2s). Scan rate 10 mV.s <sup>-1</sup> in PBS pH = 7.1. ....	104
Figure 59. Linear sweep voltammeteries of modified substrates in PBS solution and in the presence of a hole scavenger Na <sub>2</sub> SO <sub>3</sub> 1 mol.L <sup>-1</sup> . Scan rate 10mV.s <sup>-1</sup> . ....	105
Figure 60. Calculated charge transfer efficiency for the different substrates. ....	105
Figure 61. Chronoamperometry of the photoanodes at 1.23 V vs RHE under illumination during several hours. ....	107

## TABLES LIST

Table 1. Assignments and wavenumbers ( $\text{cm}^{-1}$ ) of ptt and $\text{Na}_3[\text{Fe}(\text{CN})_5(\text{ptt})]$ obtained in FTIR spectroscopy <sup>[19]</sup> .....	36
Table 2. Parameters of the iron redox process obtained from cyclic voltammetry of $\text{Na}_3[\text{Fe}(\text{CN})_5\text{NH}_3]$ complex.....	40
Table 3 Parameters of the iron redox process obtained from cyclic voltammetry of $\text{Na}_3[\text{Fe}(\text{CN})_5\text{ptt}]$ complexes. ....	41
Table 4. Wavenumbers ( $\text{cm}^{-1}$ ) of PB and ECP-Fe(III)/Fe(II)/ptt obtained in FTIR spectroscopy. ....	47
Table 5. Onset potentials obtained by cyclic voltammetry analysis. ....	53
Table 6. Redox processes observed in the modified substrates obtained by cyclic voltammetry. Potentials in V vs SCE. ....	73
Table 7. Comparison between onset potentials for $j = 0.1 \text{ mA}\cdot\text{cm}^{-2}$ of the different photoanodes obtained by cyclic voltammetry in PBS 7.1, scan rate $50 \text{ mV}\cdot\text{s}^{-1}$ . Potentials are given in V vs RHE.....	101
Table 8. Onset potentials obtained from the linear scanning voltammetries. ....	103
Table 9. Optimum potentials and maximum charge transfer efficiency obtained for the different photoanodes.....	106

## Summary

1	Electrocatalytic reduction of oxygen by metal coordination polymers produced from pentacyanidoferrate(II) complex .....	19
1.1	Introduction .....	19
1.1.1	Coordination polymers and Prussian blue .....	19
1.1.2	Hydrogen peroxide sensors .....	22
1.1.3	Pentacyanidoferrates .....	24
1.1.4	Oxygen reduction reaction (ORR).....	26
1.2	Motivation.....	28
1.3	Experimental section .....	29
1.3.1	Synthesis of $\text{Na}_3[\text{Fe}(\text{CN})_5\text{NH}_3] \cdot 3\text{H}_2\text{O}$ .....	29
1.3.2	Synthesis of $\text{Na}_3[\text{Fe}(\text{CN})_5(\text{ptt})] \cdot 5\text{H}_2\text{O}$ (ptt = 5-(4-pyridyl)-1H-1,2,4-triazole-3-thiol).....	29
1.3.3	Electronic spectroscopy .....	30
1.3.4	Vibrational Spectroscopy .....	30
1.3.5	Electrochemical characterization of cyanidoferrates .....	30
1.3.6	Electrode modification with Prussian Blue and ECP- $\text{Fe}^{3+}/\text{Fe}^{2+}/\text{ptt}$ films and peroxide electrochemical reduction .....	31
1.3.7	.....	32
1.3.8	Electrode modification for oxygen reduction .....	33
1.4	Results and discussion .....	34
1.4.1	Vibrational and electronic spectroscopy of $[\text{Fe}(\text{CN})_5(\text{ptt})]^{3-}$ .....	34
1.4.2	Electronic spectroscopy of $[\text{Fe}(\text{CN})_5(\text{ptt})]^{3-}$ .....	38
1.4.3	Electrochemical properties of $[\text{Fe}(\text{CN})_5(\text{ptt})]^{3-}$ .....	39
1.4.4	Electrochemical and spectroscopic properties of ECP- $\text{Fe}(\text{III})/\text{Fe}(\text{II})/\text{ptt}$ .....	42
1.4.5	Electrochemical response of the ECPs towards hydrogen peroxide reduction .....	48

1.4.6 Deposition of ECP-Fe(III)/Fe(II)/ptt on FTO/AuNP substrates and response towards the electroreduction of oxygen .....	49
1.5 Conclusion .....	54
2. Cobalt cyanidoferrates applied to oxygen evolution reaction (OER) .....	55
2.1 Introduction .....	55
2.1.1 Energy situation and renewable fuels .....	55
2.1.2 Electrochemical Water splitting .....	56
2.1.3 Oxygen evolution reaction (OER) .....	60
2.1.4 Catalysts for OER .....	62
2.1.5 Prussian-blue analogs (PBAs) .....	64
2.2 Motivation.....	67
2.3 Experimental section.....	68
2.3.1 Synthesis of $\text{Na}_4[\text{Fe}(\text{CN})_5(\text{isn})] \cdot 5\text{H}_2\text{O}$ (isn = pyridine-4-carboxylate) .....	68
2.3.2 Preparation of chemically modified FTO electrodes.....	69
2.3.3 FTIR spectroscopy.....	70
2.3.4 SEM microscopy .....	70
2.3.5 XPS.....	70
2.3.6 Electrochemical properties of the modified electrodes.....	70
2.3.7 Water oxidation studies.....	71
2.3.8 Oxygen evolution measurements.....	71
2.4 Results and discussion .....	72
2.4.1 Electrochemistry of the modified substrates .....	72
2.4.2 Water oxidation studies.....	76
2.4.3 Oxygen production measurements .....	83
2.5 Conclusion .....	84
3. Pentacyanidoferrate-based coordination polymers applied to photoanodes for water oxidation reaction .....	85

3.1 Introduction .....	85
3.1.1 Solar energy .....	85
3.1.2 Photochemical water splitting .....	87
3.1.3 Bismuth vanadate .....	89
3.1.4 Prussian blue and photocatalysis.....	93
3.2 Motivation.....	94
3.3 Experimental part .....	95
3.3.1 Synthesis of pentacyanidoferrates precursors .....	95
3.3.2 Preparation of FTO/BiVO <sub>4</sub> substrates .....	96
3.3.3 Deposition of cobalt cyanidoferrates on FTO/BiVO <sub>4</sub> .....	97
3.3.4 SEM microscopy .....	97
3.3.5 Photoelectrochemical studies .....	97
3.4 Results and Discussion.....	98
3.4.1 SEM microscopy .....	98
3.4.2 Photoelectrochemical studies .....	100
3.4.3 Photoelectrochemistry in hole scavenger solution .....	104
3.4.4 Long term stability .....	106
3.5 Conclusion .....	107
4. General Conclusions and perspectives .....	108
5. References .....	110

# 1 Electrocatalytic reduction of oxygen by metal coordination polymers produced from pentacyanidoferrate(II) complex

## 1.1 Introduction

### 1.1.1 Coordination polymers and Prussian blue

Inorganic materials with defined compositions, variable morphologies, and monocrystalline frameworks have received attention for several applications in material science and engineering. These materials can be represented by porous coordination polymers (PCPs) and metal–organic frameworks (MOFs). These materials have definite compositions of metal cations, which act as nodes that are linked by organic or inorganic ligands as bridges or linkers. They have interesting properties desired for the aforementioned applications like high specific surfaces areas porosity, tunable fluorescence, electrochemical activity, magnetic susceptibility, adsorption and biocompatibility. As main application of these materials, it is possible to highlight advanced catalysis, drug delivery systems, energy conversion and storage systems, fluorescence sensing, synthesis and separation and others<sup>[1][2][3]</sup>. PCPs are also interesting subject of research due to the possibility of tuning its properties by modifying their composition and morphology. For example, one can control the synthetic procedure in order to obtain coordination polymers with 1D (nanotubes), 2D (nanosheets and nanoflakes) or 3D (nanocubes) materials. (Figure 1). Tuning of the synthetic parameters makes it possible to manufacture several crystalline shapes, sizes, and compositions.

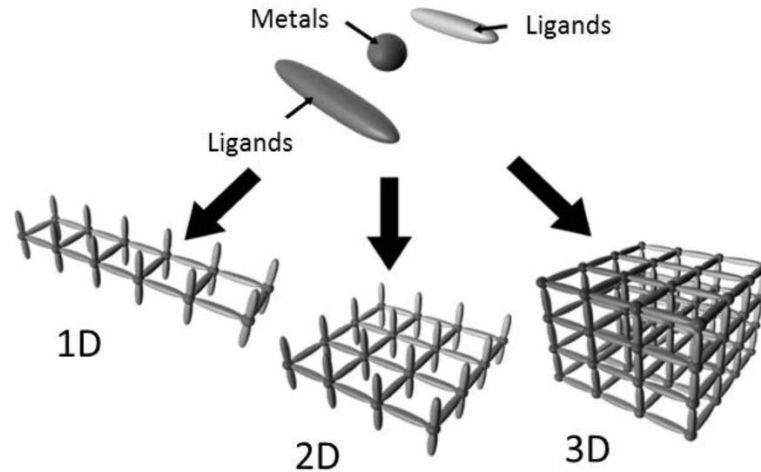


**Figure 1.** Simplified scheme showing the possible structures adopted by coordination polymers<sup>[4]</sup>.

PB is an inorganic material of mixed valence in a tridimensional network formed by Fe(II) bound to Fe(III) through a cyanide bridge. Hence PB can reach different oxidation states, either by reduction of Fe(III) or oxidation of Fe(II) <sup>[5]</sup>. PB has a face-centered cubic unit cell, as shown in Figure 2.

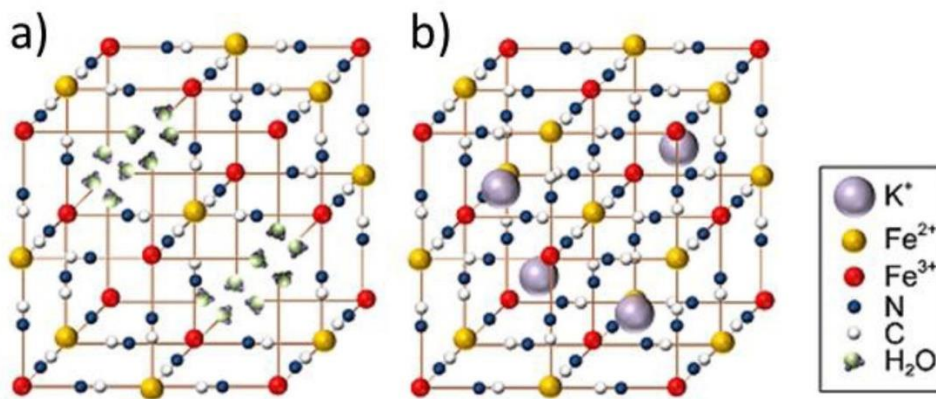


**Figure 2.** Crystal structures of a) Insoluble and b) soluble Prussian blue<sup>[1]</sup>.

Ludi and coworkers successfully grew single crystals of Prussian blue and first determined its crystal structure by X-ray diffraction<sup>[6]</sup>. The iron atoms define a simple cubic lattice, alternating Fe(II) and Fe(III), and are linked by linear cyanide groups, with their carbon atoms coordinated to the Fe(II). This open framework leaves large cavities throughout the lattice, allowing the centers of the cubic cells to be

occupied by ions or molecules up to 182 pm in radius<sup>[7]</sup>. PB can be obtained in two forms known as insoluble and soluble, even though both forms are highly insoluble ( $K_{ps} = 10^{-40}$ ). In soluble Prussian blue, half of these cavities are usually occupied by alkali metal ions such as  $K^+$  or  $Na^+$ . In insoluble form ( $Fe^{III}_4[Fe^{II}(CN)_6]_3 \cdot xH_2O$ ) there are interstitial water molecules in the framework, which cause some structural defects. Water molecules can be found coordinated to M(II) or inside cavities, not coordinated to the metal site. The oxygen atoms of the water molecules may occupy the regular lattice positions instead of C or N in order to complete the octahedron causing random defects.

Because of the strong ligand field of the cyanide, Fe(II)-CN always adopts a diamagnetic low-spin (ls)  $d^6$  configuration with  $S=0$ . Fe(III)-NC is found in a paramagnetic high-spin (hs)  $d^5$  state ( $S = 5/2$ ) in the weaker field of the N-ligand (Figure 3). Upon electromagnetic irradiation or changes in pressure or temperature, the iron centers might undergo transitions between their hs and ls states, making PB a spin-crossover (SCO) compound. The strong intervalence charge-transfer (CT) absorption between ls  $d^6$   $t_{2g}$  Fe(II)-C and hs  $d^5$   $t_{2g}$  Fe(III)-N at  $\sim 1.75$  eV causes the intense blue color of the compound<sup>[8]</sup>.

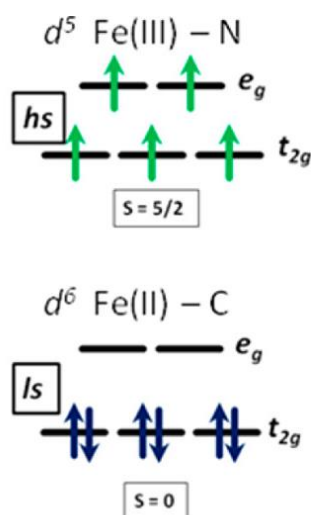


**Figure 3.** Spin configurations of iron atoms in the PB structure<sup>[8]</sup>.

PB has also attracted attention due to the possibility of creating particles with different shapes and morphologies by template assisted methods. It was possible

to obtain cubes, truncated cubes, cuboctahedrons, truncated octahedrons, hexapods, and star-like hexapods. This was reflected in different reactivities and stabilities of the material according to the synthetic method. The main methods for the obtention of PB include precipitation, microemulsion, sonochemical, hydrothermal, microwave-assisted, selective chemical etching, and electrodeposition<sup>[1]</sup>.

### 1.1.2 Hydrogen peroxide sensors

PB is known as artificial peroxidase due to its ability to reduce hydrogen peroxide at low potentials, which minimizes the effects of possible interfering species that may be present in biological samples<sup>[9,10]</sup>. H<sub>2</sub>O<sub>2</sub> also plays an important role in the expanding area of clinical diagnostics. Firstly, it is a valuable marker for oxidative stress, recognized as one of the major risk factors in progression of pathophysiological complications in diabetes, atherosclerosis, renal disease, cancer, and aging<sup>[11]</sup>. Thus, it has been extensively used in biosensors as a modifier of working electrodes coupled to oxidase enzymes, enabling the electrochemical determination of several species of biological interest or in point-of-care devices<sup>[12][13]</sup>. Compared to platinum, which is the mostly used material for detection of hydrogen peroxide, PB modified electrodes are more active in H<sub>2</sub>O<sub>2</sub> reduction and oxidation in neutral media, more selective for hydrogen peroxide reduction in the presence of oxygen and have higher sensitivity<sup>[14]</sup>. The choice of metals to be used in the electrochemical reduction of hydrogen peroxide is inspired by the Fenton reaction. Thus, hexacyanoferrates of iron, copper, cobalt, and nickel ions have been employed but their activities are orders of magnitude lower than PB<sup>[11]</sup>.

Due to this behavior, PB have received attention in the development of several biosensors coupled to oxidase enzymes. This class of enzymes acts by oxidising the substrate and then returning to their original active state by transferring electrons to molecular oxygen, so that the final products of these enzymes are the oxidised form of the substrate and, as a side product, hydrogen peroxide. Thus, the determination of hydrogen peroxide can give information of the initial concentration of the substrate. However, a great drawback in this approach is the high overpotential

needed for hydrogen peroxide oxidation (ca. 0.7 V versus Ag/AgCl) where many electroactive substances (i.e. ascorbic acid, uric acid, etc.) present in real biological samples can oxidize and act as interfering agents<sup>[15]</sup>. A strategy to avoid this problem is to use a redox mediator system in order to promote the reduction of hydrogen peroxide. Horseradish peroxidase (HRP) is an enzyme that catalyse this reaction and has been used with this function. However, it has drawbacks such as its high cost, low stability and poor binding to the surface of substrates. In this sense, PB has the advantages due to its low cost, easy preparation methods and possibility of modification of many different substrates. A typical scheme of a PB-based biosensor is shown in Figure 4 and represent an indirect method to quantify a biologic analyte based on the determination of hydrogen peroxide.

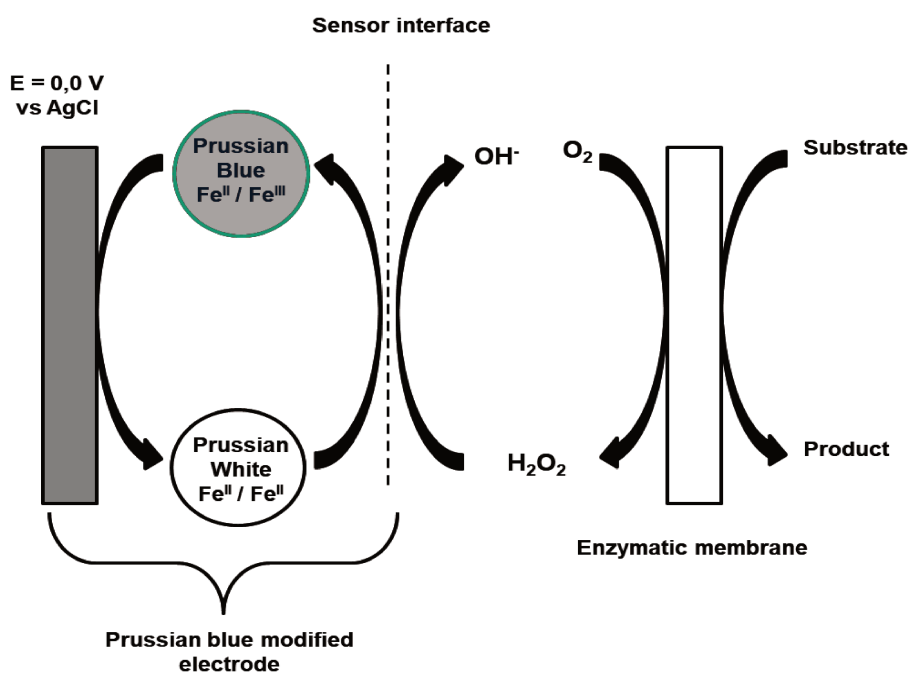


**Figure 4.** General scheme of a Prussian blue-based electrochemical biosensor<sup>[15]</sup>.

Itaya *et al* first showed that the reduced form (Prussian white) was active for the reduction of O<sub>2</sub> and hydrogen peroxide. Also, the oxidized form of Prussian Blue (Berlin green) showed a catalytic activity for the oxidation of hydrogen peroxide<sup>[16]</sup>. The catalytic effect of PB towards oxygen and hydrogen peroxide was attributed to the zeolitic structure of PB which allows the diffusion of small molecules through the

crystal. When hydrogen peroxide (or oxygen) penetrates the PB lattice structure, it will be located in the center of each vacancy being surrounded by four divalent high spin iron ions on average, which can bring about a catalytic reduction of H<sub>2</sub>O<sub>2</sub> via a four electron reaction<sup>[15]</sup>. Still, the mechanism is not clear.

### 1.1.3 Pentacyanidoferrates

An alternative method to modify the structure of PB is using complexes able to form five cyanide bridges along the structure, instead of six observed in the classical Prussian blue structure. Because of this, the pentacyanidoferrates(II) ( $[\text{Fe}(\text{CN})_5\text{L}]^{n-}$ ) complexes are promising candidates<sup>[17,18]</sup>. Pentacyanidoferrates (II) represent a class of classic complexes whose electronic, spectroscopic and kinetic properties have been widely studied<sup>[19–22]</sup>. The properties of these complexes are very dependent of the nature of the ligand L, which allows one to modulate their reactivity and redox activities<sup>[21,23]</sup>. These species have a great affinity for N-heterocyclic ligands and this was explored to obtain functionalized films for the electrochemical determination of analytes such as cysteine<sup>[24]</sup> and creatinine<sup>[25]</sup>.

A modified PB structure produced from a pentacyanidoferrate precursor was first reported by Toma *et. al* and was described as a mixed-valence complex containing the pentacyanidoferrate moiety and an isonicotinamide ligand. The obtained material showed reversible electrochromic behavior as denoted by the variation of the observed intervalence charge transfer band by applying constant potentials<sup>[18]</sup>.

Recently, our research group described the use of an electrochemically active polymer based on pentacyanidoferrate complex applied in the electrochemical oxidation of ascorbic acid. The pentacyanidoferrate had a negative-charged isonicotinate as N-heterocyclic ligand. The material was electrodeposited on the surface of a glassy carbon electrode and showed good stability in acid solutions, which is in agreement with the expected behavior of PB films, since in neutral and basic solutions the iron atoms may react with hydroxyl ions in solution and disrupt the framework. The electrochemical oxidation of ascorbic acid was very efficient in both

pH 3.0 and 5.0 and proved that the coordination polymer maintain its activity even in the presence of an organic moiety on the structure<sup>[26]</sup>.

Our group also reported the use of a very stable pentacyanidoferrate complex (named PCF-mpz) containing a positive-charged ligand, N-methylpyrazinium, which is also a strong acceptor ligand. The corresponding PB analog was deposited on the surface of a glassy carbon electrode by drop-casting method. The electroactive film was stable in acid solutions, where the electrochemical response to hydrogen peroxide was tested. The novel coordination polymer provided a considerable enhancement of the catalytic current when compared to traditional Prussian blue operating at low potentials, and this also reflects that the peroxidase behavior of the material was preserved. From the data obtained from Job's plot it was possible to propose a 2:1PCF-mpz/Fe(III) ratio in the material structure, which is represented by the model in Figure 5 <sup>[27]</sup>.

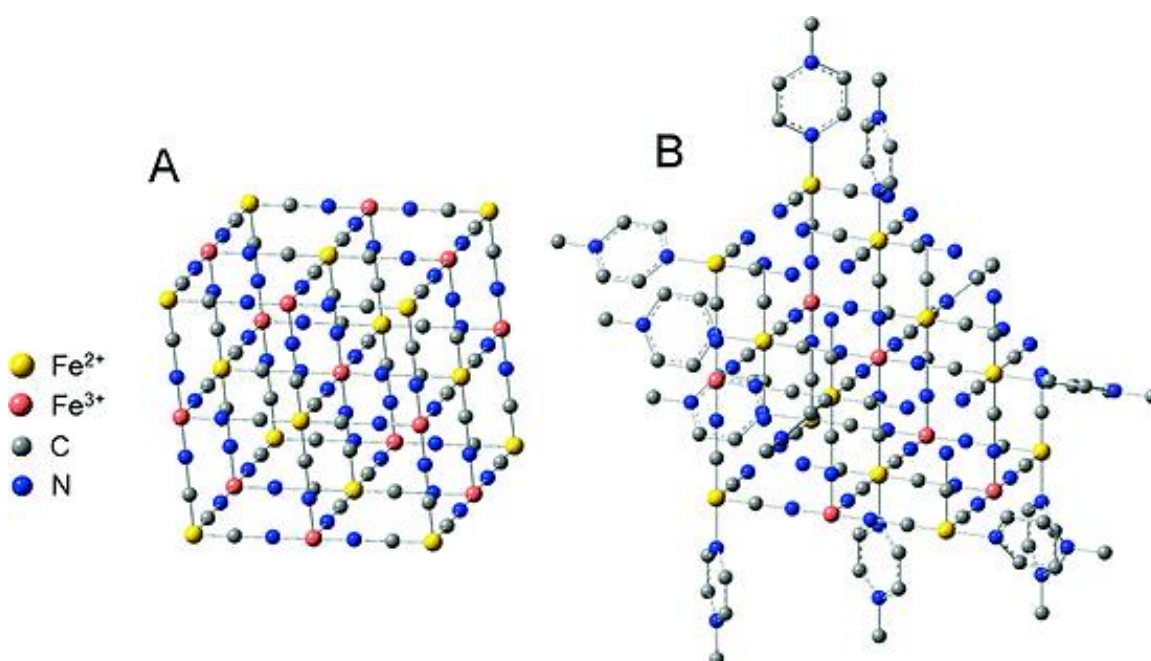


**Figure 5.** A) Structure of PB and B) proposed structure of PB-mpz, with hydrogens omitted<sup>[27]</sup>.

### 1.1.4 Oxygen reduction reaction (ORR)

The electrochemical properties of PB and its analogs can also be used in studies of electrochemical oxygen reduction reaction (ORR). This is a very important reaction that occurs at the cathode of fuel cells, such as in proton exchange membrane fuel cell (PEMFC). At the anode of a PEMFC, hydrogen is oxidized to produce electrons and protons that are transferred to the cathode through an external circuit and the proton exchange membrane, respectively ( $\text{H}_2 \rightarrow 2\text{H}^+ + 2\text{e}^-$ ). At the cathode, oxygen is reduced by reaction with protons and electrons to produce water. In these cells, both the anode and the cathode electrodes consist of highly dispersed Pt-based nanoparticles on carbon black to promote the reaction rates of the hydrogen oxidation reaction (HOR) and the ORR. The reaction rate of HOR on Pt is extremely fast so that the Pt loading at the anode can be reduced to less than  $0.05 \text{ mg cm}^{-2}$ . On the other hand, at the cathode, the sluggish reaction kinetics of ORR even on the best Pt-based catalyst requires much higher Pt loading ( $\sim 0.4 \text{ mg.cm}^{-2}$ ) to achieve a desirable fuel cell performance<sup>[28]</sup>. Since Pt is a high-cost noble metal, it would be interesting to find substitutes for this application.

Some strategies to minimize the use of noble metals have been studied and include the use of PB in a synergistic system with platinum nanoparticles, enhancing the kinetics of the ORR reaction<sup>[29]</sup>. PB was also used as electroactive layer of chemically modified electrodes in order to promote tetraelectronic reduction of dioxygen to water (Figure 6) <sup>[16]</sup>.

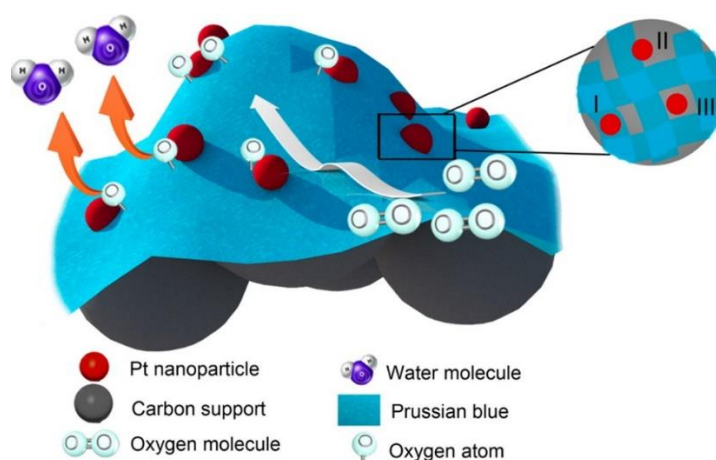
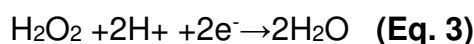
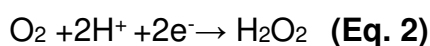
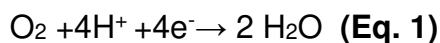


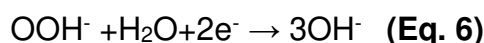
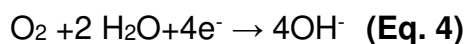
**Figure 6.** Synergistic mechanism of ORR promoted by a PB/Pt system<sup>[29]</sup>.

The overall ORR may involve either a single four-electron ( $4e^-$ ) or two-step two-electron transfer ( $2e^-$ ), in a pH dependent reaction<sup>[30]</sup>:

**Acidic solution:**



**Basic solution:**



In fuel cell operations, a direct  $4e^-$  pathway is highly preferred to get high efficiency, while selective  $2e^-$  reduction is used in industrial  $\text{H}_2\text{O}_2$  production. The detailed mechanisms of ORR are complicated and depend on the surface properties of the electrode.

The mechanism for the ORR in acid media has already been described by Prakash *et. al.* After diffusion of oxygen to the surface of the catalyst, two different types of adsorption may occur. Depending on the interaction of  $\text{O}_2$  with the catalyst surface, the oxygen reduction will either proceed via a two-site adsorption leading to the direct four-electron reduction of oxygen to water or terminal adsorption for the peroxide route, which may rearrange to yield a double bond in a single site adsorption. The adsorption models for the oxygen on the surface of a metallic catalyst is presented in Figure 7. For each adsorption type, protonation may either precede or follow adsorption, depending on the degree of proton solvation and the distance between the oxygen molecule and the surface<sup>[31]</sup>.

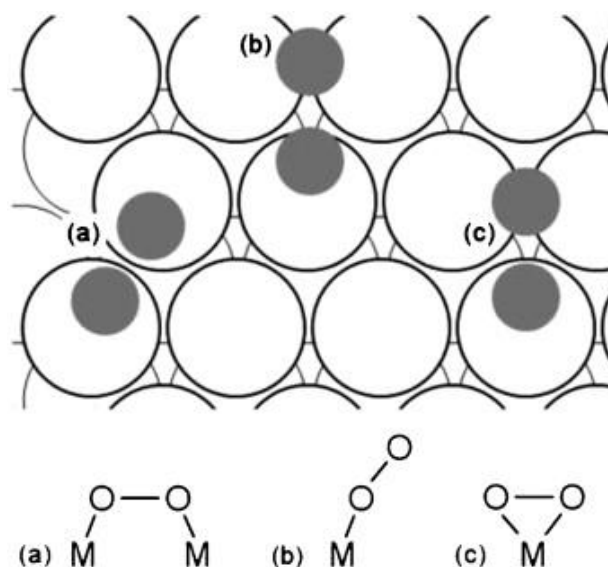


**Figure 7.** Adsorption models proposed for the oxygen molecule on the surface of a (111) face of face centered cubic transition metal catalyst<sup>[31]</sup>.

Whether the reaction takes a dissociative or an associative pathway depends mainly on the initial  $O_2$  dissociating energy barrier on a given surface. For example, several DFT calculation studies showed that this dissociation energy barrier value for carbon surfaces is normally very high, accordingly not favorable for the  $4e^-$  dissociative pathway. Therefore, the experimentally measured electron transfer numbers on almost all carbon materials are smaller than four. In contrast, ORR on most metal surfaces normally takes a dissociative pathway due to the strong adsorption of  $O_2$ . This theoretical result is also consistent with experimental finding that Pt-based materials always show perfect  $4e^-$  reduction selectivity. One of the exceptional cases among metals is Ag (111), on which the  $O_2$  adsorption is weak, which results in high  $O_2$  dissociation barrier of 41 eV. For this reason the reaction pathway on the Ag surface obeys generally the associative mechanism with strong  $2e^-$  pathway selectivity<sup>[30]</sup>.

## 1.2 Motivation

Since PB has shown interesting activity towards the electrochemical reduction of oxygen and hydrogen peroxide, we wanted to evaluate the possible effects of an electroactive coordination polymer (ECP) produced from a pentacyanidoferrate when

applied in these reactions. Thus, possible effects of different organic moieties can be evaluated, including changes in the active surface area and redox potentials of the catalytic sites. The following results were also published in the journal *Inorganica Chimica Acta* in an article entitled “Electrocatalytic reduction of oxygen by metal coordination polymers produced from pentacyanidoferrate(II) complex”<sup>[32]</sup>.

## 1.3 Experimental section

### 1.3.1 Synthesis of $\text{Na}_3[\text{Fe}(\text{CN})_5\text{NH}_3] \cdot 3\text{H}_2\text{O}$

The procedure was adapted from the literature<sup>[33]</sup>. The complex was obtained by adding 28% ammonium hydroxide ( $\text{NH}_4\text{OH}$  m/v, Sigma–Aldrich; 40 mL) to an 250 mL Erlenmeyer flask containing sodium nitroprusside ( $\text{Na}_2[\text{Fe}(\text{CN})_5\text{NO}] \cdot 2\text{H}_2\text{O}$ , 99%, Acros Organics; 6.0 g, 20 mmol). The flask was stirred until the complete solubilization of sodium nitroprusside. Some bubbles appeared in the flask during this procedure. Then, the flask was covered with aluminum foil and the top of the flask covered with cotton to allow the gas to exit. After 3 h in the dark, the solution had a dark-yellow color. Sodium iodide ( $\text{NaI}$  98% Merck; 6.0 g, 40 mmol) was added and a yellow precipitate appeared. Ethanol ( $\text{C}_2\text{H}_6\text{O}$  99.9%, Merck; 100 mL) was slowly added to ensure complete precipitation. The solid was filtered, washed with ethanol, and dried on a vacuum line until constant weight. Yield: 93%. Elemental analysis calculated for  $\text{C}_5\text{H}_9\text{FeN}_6\text{Na}_3\text{O}_3$ : C 18.42%; H 2.78%; N 25.78%. Found: C 18.50%; H 2.07 %; N 26.06%.

### 1.3.2 Synthesis of $\text{Na}_3[\text{Fe}(\text{CN})_5(\text{ptt})] \cdot 5\text{H}_2\text{O}$ (ptt = 5-(4-pyridyl)-1H-1,2,4-triazole-3-thiol)

In a beaker, ptt (455 mg, 2.55 mmol) (Sigma-Aldrich) was added to 50 mL of water. The solution was heated in a water bath at 70 ° C to increase solubility of the ligand. In another beaker, 130 mg (0.4 mmol) of  $\text{Na}_3[\text{Fe}(\text{CN})_5\text{NH}_3] \cdot 3\text{H}_2\text{O}$  were added to 13 mL of water. The ligand solution was added dropwise over the complex solution

under stirring. After completion of the addition, the solution was stirred in an ice bath for 30 minutes, filtered under vacuum and the solid was washed with cold water. Subsequently, the filtered solution was centrifuged for about 5 minutes. Finally, the solvent was removed using a rotary evaporator in mild heating conditions. The resulting solid was dried in a vacuum line until constant weight. Yield: 90 %. Elemental analysis calculated for  $C_{12}H_{16}FeN_9Na_3O_5S$ : C 27.55%; H 3.08%; N 24.09%. Found: C 27.92%; H 2.59 %; N 24.01%.

### 1.3.3 Electronic spectroscopy

Spectra of aqueous solutions of the complexes in the UV-Visible region were obtained in a HP8453 UV-visible absorption spectrophotometer, with a 1 cm light path quartz cuvette.

### 1.3.4 Vibrational Spectroscopy

Infrared spectra of the complexes and ptt were recorded as KBr pellets in a MB100 Bomem Spectrometer, with  $2\text{ cm}^{-1}$  resolution in the range of  $4000$  to  $400\text{ cm}^{-1}$ .

### 1.3.5 Electrochemical characterization of cyanidoferrates

Cyclic voltammograms and differential pulse voltammograms were obtained with a Autolab EcoChemie PGSTAT20, using potassium chloride (KCl, Synth)  $0.1\text{ mol L}^{-1}$  as supporting electrolyte in all measurements. A glassy carbon electrode was used as working electrode, Ag/AgCl (KCl saturated) electrode as reference electrode and platinum electrode as auxiliary electrode. In each measurement,  $2.0 \times 10^{-3}\text{ mol L}^{-1}$  solutions of ptt or pentacyanidoferrates were used. All solutions were deaerated by bubbling nitrogen before the measurements. The potential range used was from  $-0.75$  to  $1.25\text{ V}$  vs Ag/AgCl and the scanning rates were 10, 25, 50, 100 and  $200\text{ mV s}^{-1}$ .

Studies involving controlled pH were performed in Britton-Robinson buffer solutions<sup>[34]</sup>, and pH adjustments were done using a concentrated potassium hydroxide solution. Electrochemical behavior of the complex in solution was studied by  $i_p$  vs  $v$  plots, according to the Randles-Sevcik equation<sup>[35]</sup>:

$$i_p = 2,69 \times 10^5 n^{3/2} AD^{1/2} C v^{1/2} \text{ (Eq. 7)}$$

where  $i_p$  is the current peak of the cyclic voltammograms,  $A$  is the electroactive area ( $\text{cm}^2$ ),  $c$  is the concentration of  $\text{Fe}(\text{CN})_6^{4-/3-}$  solution ( $\text{mol}\cdot\text{cm}^{-3}$ ),  $D$  is the diffusion coefficient of the species ( $\text{cm}^2\cdot\text{s}^{-1}$ ),  $n$  is the number of electrons involved in the redox process (ex:  $n = 1$  for  $[\text{Fe}(\text{CN})_6]^{4-/3-}$ ) and  $v$  is the scan rate ( $\text{V}\cdot\text{s}^{-1}$ ).

### 1.3.6 Electrode modification with Prussian Blue and ECP- $\text{Fe}^{3+}/\text{Fe}^{2+}/\text{ptt}$ films and peroxide electrochemical reduction

Fluorine-doped tin oxide coated glasses substrates (FTO, Sigma-Aldrich, Resistivity  $8\Omega/\text{sq}$ ) with  $1 \text{ cm}^2$  active area were previously immersed in a 1:3  $\text{H}_2\text{O}_2:\text{H}_2\text{SO}_4$  solution for 10 min. After that, FTOs were immersed in a  $\text{NH}_4\text{OH}$ ,  $\text{H}_2\text{O}_2$  and water solution (1:1:5) for 15 min and so rinsed with water. PB films were deposited from both potassium ferricyanide and pentacyanidoferrate (II) in order to compare the electrochemical features of the different coverages.

PB produced from potassium ferricyanide was deposited by using a solution containing  $1.0 \times 10^{-3} \text{ mol L}^{-1} \text{ K}_3[\text{Fe}(\text{CN})_6]$  (Acros Organics),  $1.0 \times 10^{-3} \text{ mol L}^{-1} \text{ FeCl}_3$  (Synth),  $0.1 \text{ mol L}^{-1} \text{ HCl}$ , and  $0.1 \text{ mol L}^{-1} \text{ KCl}$ . Deposition was made by cycling the FTO substrates in the range of  $-0.2$  to  $0.6 \text{ V}$  vs  $\text{Ag}/\text{AgCl}$  at  $20 \text{ mV s}^{-1}$  scan rate. Then the films were dried in a desiccator prior to their use in electroanalytical measurements.

PB films produced from pentacyanidoferrate (II) complex  $[\text{Fe}(\text{CN})_5(\text{ptt})]^{3-}$  were used to modify the substrates also using electrochemical deposition. In an electrochemical cell a solution was prepared containing  $1.0 \times 10^{-3} \text{ mol L}^{-1} [\text{Fe}(\text{CN})_5(\text{ptt})]^{3-}$ ,  $0.1 \text{ mol L}^{-1} \text{ KCl}$  and  $1.0 \times 10^{-2} \text{ mol L}^{-1} \text{ HCl}$ . A potassium peroxydisulfate solution (Merck) was added in order to obtain a final concentration of  $1.0 \times 10^{-2} \text{ mol L}^{-1}$  of this compound. The solution was kept under stirring for 10 minutes and after that, ferric chloride was added in order to obtain a final concentration of 1.0

$\times 10^{-3}$  mol L<sup>-1</sup>. The deposition method used was the same as described for the potassium ferricyanide precursor.

Thicknesses (d) of the cyanidoferrates films were estimated using the equation 8, accounting the number of unit cells of PB present on the surface of the modified electrodes<sup>[36]</sup>.

$$\mathbf{d} = \left( \frac{Q_{\text{ox}}}{nFA} \right) \left( \frac{l^3 N_A}{4} \right) \text{ (Eq. 8)}$$

$Q_{\text{ox}}$  is the charge involved in the oxidation from PW to PB, obtained by integrating the anodic peak,  $n$  is the number of electrons involved in the electrochemical process,  $F$  is Faraday's number,  $A$  is the electrode geometrical area,  $l$  is the length of PB unit cell (1.02 nm) and  $N_A$  is Avogadro's number.

Electroactive areas of the electrodes were calculated using Equation 7, where  $[\text{Fe}(\text{CN})_6]^{4/3-}$  was used as redox probe. The slope of the plot  $i_p$  vs  $v^{1/2}$  should provide the electroactive area of the different electrodes. An interesting feature observed was the fact that the  $[\text{Fe}(\text{CN})_5(\text{ptt})]^{3-}$  complex produced modified electrodes with a higher electroactive area than ferricyanide.

### **1.3.7 Electrochemical response of ECP-Fe<sup>3+</sup>/Fe<sup>2+</sup>/ptt towards hydrogen peroxide reduction**

ECPs based on cyanidoferrates are widely known as catalysts of hydrogen peroxide reduction. Thus, in order to evaluate the electrochemical activity of the film of ECP-Fe<sup>3+</sup>/Fe<sup>2+</sup>/ptt, studies of electrochemical reduction of H<sub>2</sub>O<sub>2</sub> using chronoamperometry were performed. The measurements were performed in a HCl/KCl 0.1 mol L<sup>-1</sup> solution, in an electrochemical cell containing the modified substrates as the working electrodes, Ag/AgCl as the reference electrode and platinum wire as the auxiliary electrode. During the measurements, a potential of -0.1 V vs Ag/AgCl was

applied and additions in the range of 20-80  $\mu\text{L}$  of the  $5 \times 10^{-3} \text{ mol L}^{-1} \text{ H}_2\text{O}_2$  stock solution were added to the electrochemical cell under constant stirring. FTO substrates modified with PB were also used for comparison purposes.

### 1.3.8 Electrode modification for oxygen reduction

As a strategy to increase the electroactive surface area of FTO and enhance the charge transfer between solution and the modified electrode, gold nanoparticles were deposited on the substrates<sup>[37]</sup>.

Gold nanoparticles were obtained using the traditional Turkevich method<sup>[38]</sup>. 100 mL of a 1 mM  $\text{HAuCl}_4$  (Sigma-Aldrich) solution were boiled under vigorous stirring. To this solution, 3 mL of a 1% (w/w) sodium citrate (Synth) solution were added. The mixture was stirred until a red color appeared. After that, it was stirred for 30 more minutes and then cooled slowly to room temperature under continuous stirring. Then the gold nanoparticles suspension was centrifuged at 4000 rpm for 5 minutes and stored in a refrigerator prior to use.

Firstly, the FTO substrates were immersed in a  $1 \times 10^{-3} \text{ mol L}^{-1}$  methanolic solution of 3-mercaptopropyltrimethoxysilane (Aldrich) for 12 h. After this period, they were rinsed with water and immersed in an AuNP dispersion for 12 h. Finally, the substrates were rinsed with water, immersed in a  $1 \times 10^{-3} \text{ mol L}^{-1}$  solution of  $\text{Na}_3[\text{Fe}(\text{CN})_5(\text{ptt})]$  for 1 hour, rinsed again with water and stored in a desiccator prior to use in electrochemical experiments. Electroactive areas were calculated as in the previous section.

The oxygen reduction experiments were performed by cyclic voltammetry using  $0.1 \text{ mol L}^{-1} \text{ KCl}$  solutions saturated with oxygen or deaerated with nitrogen, in the range of -1.0 to 0.2 V vs Ag/AgCl, at the scan rate  $50 \text{ mV.s}^{-1}$ .

## 1.4 Results and discussion

### 1.4.1 Vibrational and electronic spectroscopy of $[\text{Fe}(\text{CN})_5(\text{ptt})]^{3-}$

The ligand, 5-(4-pyridyl)-1H-1,2,4-triazole-3-thiol (ptt), has a pyridyl ring able to coordinate to pentacyanidoferrate(II), a triazole ring and a thiol group attached directly to an aromatic ring that contributes to the occurrence of tautomerism <sup>[39][40]</sup>. Thus, before synthesizing the pentacyanidoferrate complex, it is important to determine which tautomer is the most stable<sup>[41]</sup>. Vibrational spectroscopy is a technique that provides information about chemical bonding and help identifying the occurrence of the tautomers of ptt, which are presented in Figure 8. The infrared spectrum obtained for the ptt is presented in Figure 9. It is possible to assign the vibrational frequencies to S-H stretching and according to the literature <sup>[40]</sup>, the tautomer 1 is the most stable form in the solid state and in the experimental conditions.

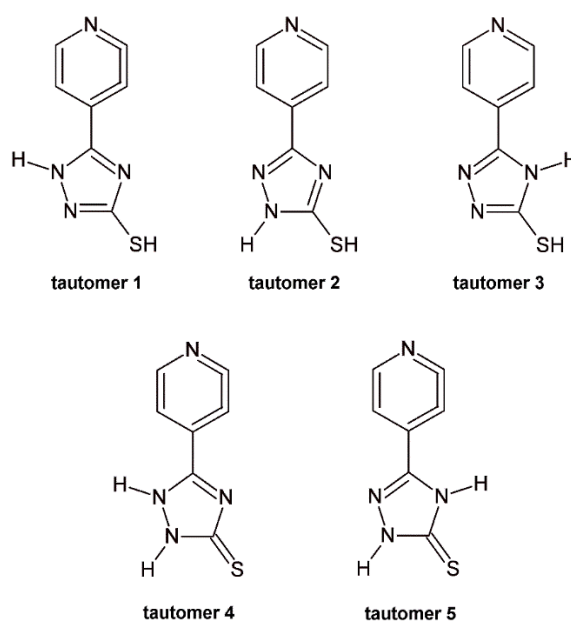


**Figure 8.** Possible tautomers for the ptt molecule.

FT-IR technique was used to confirm the coordination mode of the ligand ptt in the complex. Pentacyanidoferrates(II) are known to form stable complexes with

N-heterocycles, amino acids, sulfoxides, thioethers and thioamides [42]. Thus, the interaction with ptt could occur through nitrogen atoms of pyridine or sulfur from the thiol group. From the infrared spectra (Figure 9) of the free ligand and complex, it is possible to observe that the band ( $\nu(\text{C-C}) + \nu(\text{N-C})$ ) attributed to pyridine ring stretching in  $1588 \text{ cm}^{-1}$  shifts to  $1614 \text{ cm}^{-1}$  in the spectrum of  $[\text{Fe}(\text{CN})_5(\text{ptt})]^{3-}$ , indicating the coordination to the metal through the pyridine ring<sup>[43]</sup>. The complete attributions of the spectra are presented in

Table 1.

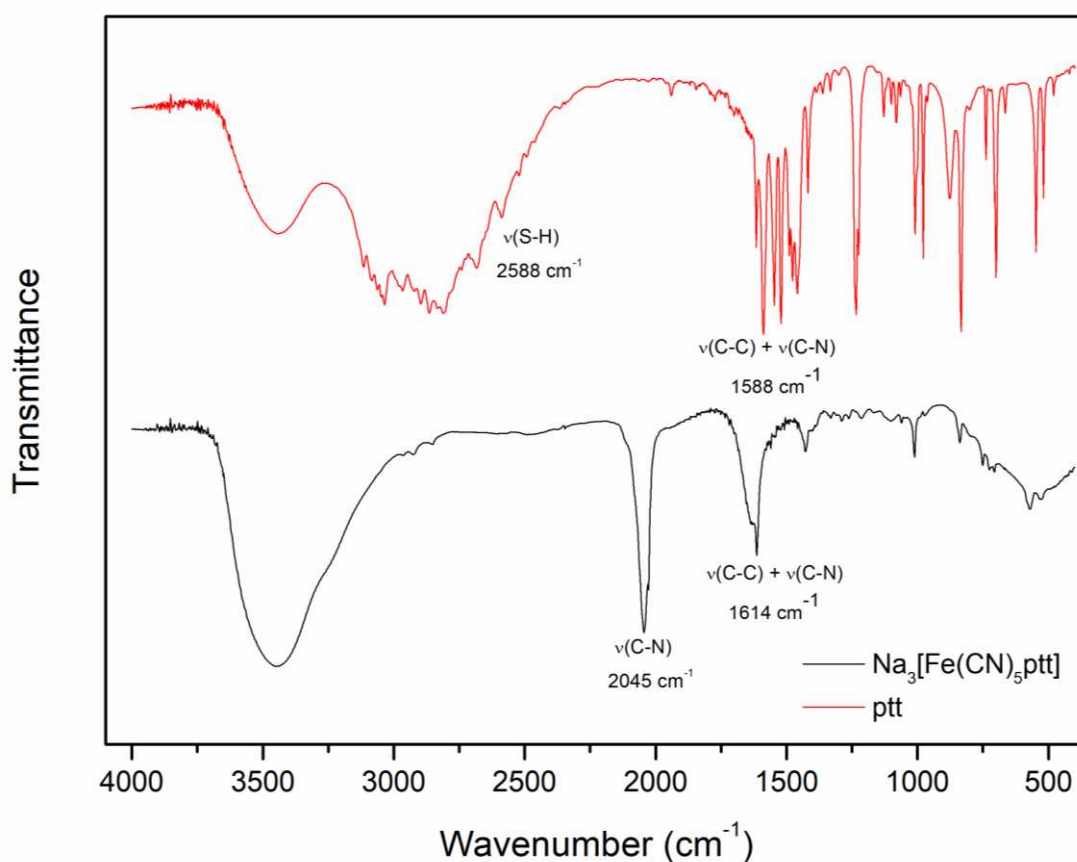


**Figure 9.** Infrared spectra of  $\text{Na}_3[\text{Fe}(\text{CN})_5(\text{ptt})]$  and free ptt ligand.

**Table 1.** Assignments and wavenumbers (cm<sup>-1</sup>) of ptt and Na<sub>3</sub>[Fe(CN)<sub>5</sub>(ptt)] obtained in FTIR spectroscopy [19].

Assignment	ptt	Na <sub>3</sub> [Fe(CN) <sub>5</sub> (ptt)]
v(N-H)	3446s	
v(O-H)		3445vs
v(C-H)	3035vs	
v(C-H)	2969vs	
v(C-H)	2866vs	
v(C-H)	2810vs	
v(S-H)	2588vw	
v(C-N)		2045s
v(Pyridine ring)	1616s	1635vs
Pyridine ring v(C-C) + v(N-C)	1588vs	1614vs
v(Pyridine ring) + v(triazole ring)	1547vs	
δHCN + δHCC	1521vs	
v(Triazole ring)	1477s	
Triazole v(N-C)	1459s	1428m
v(Triazole ring)	1418m	
v(Triazole ring)	1360w	1387w
δ(Triazole ring)	1333w	1331w
v(Triazole ring)	1296w	1290w

v = stretching; δ = in-plane bending; τ = torsion; vs = very strong; s = strong; m = medium; w = weak; sh = shoulder

**Table 1. (cont.)** Assignments and wavenumbers (cm<sup>-1</sup>) of ptt and Na<sub>3</sub>[Fe(CN)<sub>5</sub>(ptt)] obtained in FTIR spectroscopy <sup>[19]</sup>

Assignment	ptt	Na <sub>3</sub> [Fe(CN) <sub>5</sub> (ptt)]
Pyridine ring $\nu$ (C-C) + $\nu$ (N-C)	1234vs	1261w
$\nu$ (Pyridine ring)	1225s	1214w
$\nu$ (N-N)	1129m	1165w
$\nu$ (Pyridine ring)	1100w	1099w
$\delta$ HCC + $\delta$ CCN	1081m	1060w
$\nu$ (Pyridine ring) + $\nu$ (Triazole ring)	1009s	1011m
$\tau$ (Pyridine ring) + $\tau$ (Triazole ring)	996sh	989sh
$\nu$ (Pyridine ring) + $\nu$ (triazole ring)	978s	970w
$\tau$ HCCC	877s	
$\tau$ (HCCC +CNCC)	834vs	838m
$\nu$ (Triazole ring)	739m	751w
$\delta$ (Pyridine ring)	705s	725w
$\delta$ (Pyridine ring)	699s	704w
$\delta$ (Pyridine ring)	664m	
$\delta$ Fe-CN		573m
$\tau$ (Pyridine ring)	546s	
$\nu$ (S-C) + $\delta$ (Pyridine ring)	519s	526w
$\tau$ (HNCC) + $\tau$ (Pyridine ring)	480w	

$\nu$  = stretching;  $\delta$  = in-plane bending;  $\tau$  = torsion; vs = very strong; s = strong; m = medium; w = weak; sh = shoulder

### 1.4.2 Electronic spectroscopy of $[\text{Fe}(\text{CN})_5(\text{ptt})]^{3-}$

Pentacyanidoferrate(II) complexes,  $[\text{Fe}(\text{CN})_5(\text{L})]^{n-}$ , have different properties according to the nature of the ligand L<sup>[23]</sup>. Complexes containing ligands such as NO or  $\text{NH}_3$  show weak absorption bands in the visible region in the range of 360 nm to 425 nm<sup>[22,23]</sup>. However, for complexes containing N-heterocyclic ligands, a strong band is expected in the range of 400 to 500 nm, due to metal-to-ligand charge transfer (MLCT)<sup>[23]</sup>. Ligands with S-donor groups can also coordinate with iron, however, the maximum absorption expected in this case appears in the range of 600-700 nm<sup>[42]</sup>. The electronic spectrum of  $[\text{Fe}(\text{CN})_5(\text{ptt})]^{3-}$  is presented in Figure 10. The maximum absorption at 430 nm ( $\epsilon = 2.7 \times 10^3 \text{ L mol}^{-1} \text{ cm}^{-1}$ ) can be observed, which agrees with the MLCT reported in the literature for similar complexes and indicates the coordination through the nitrogen from the N-heterocyclic portion of the ptt ligand.

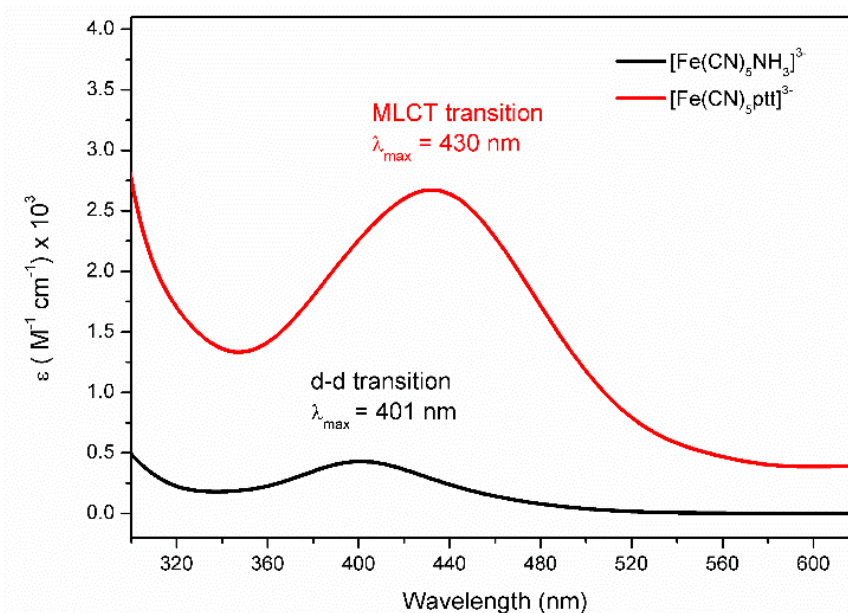


**Figure 10.** Comparison of the UV-Vis spectrum of  $[\text{Fe}(\text{CN})_5(\text{ptt})]^{3-}$  with the precursor complex  $[\text{Fe}(\text{CN})_5\text{NH}_3]^{3-}$  in aqueous solution.

### 1.4.3 Electrochemical properties of $[\text{Fe}(\text{CN})_5(\text{ptt})]^{3-}$

The redox potential of iron in  $[\text{Fe}(\text{CN})_5\text{L}]^{n-}$  complexes is directly influenced by the nature of different ligands (L), as described in previous studies [21,26]. Comparing a series of different N-heterocyclic ligands, the formal reduction potential of the  $\text{Fe}^{3+}/\text{Fe}^{2+}$  redox pair shifts to higher values as the acceptor ability of the ligand increases. The same was observed for the substitution of ligands between  $\text{NH}_3$  and ptt, where the former showed  $E_0' = 0.15 \text{ V vs Ag/AgCl}$ , while the last showed  $E_0' = 0.32 \text{ V vs Ag/AgCl}$ . Furthermore, it is possible to observe a peak in the cathodic region of the voltammogram ( $E_{\text{pc}} = -0.5 \text{ V}$ ), and another peak in the anodic region ( $E_{\text{pa}} = 0.8 \text{ V}$ ) which are assigned to a ligand centered redox process, as confirmed by cyclic voltammograms of the free ligand (Figure 11). Both the oxidation and reduction of the complex were proven to be diffusion controlled, due to the linear behavior of the current peaks with the square root of the scan rate, as given in Figure 12. Table 2 shows data obtained from the cyclic voltammograms of the complex. The results show that the separation between peak potentials increased with the scan rate, showing a quasi-reversible behavior of the compound.

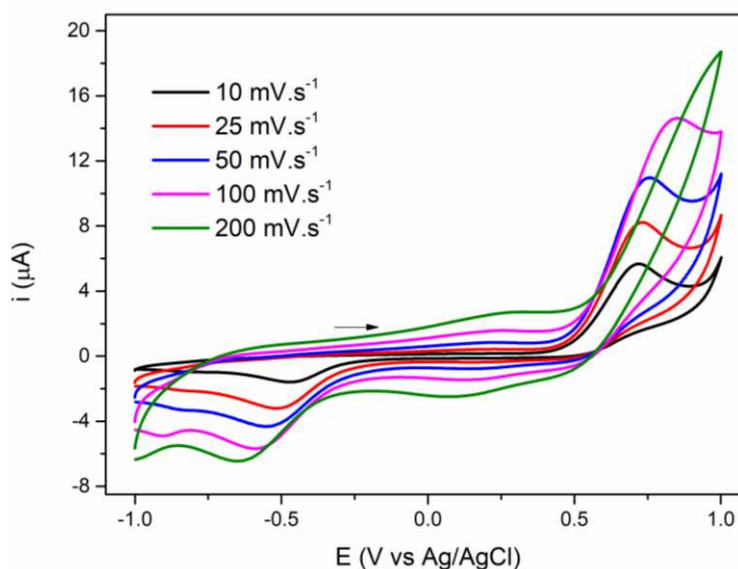


**Figure 11.** Cyclic voltammetry of ptt aqueous solution at different scan rates using  $\text{KCl } 0.1 \text{ mol L}^{-1}$  as supporting electrolyte.

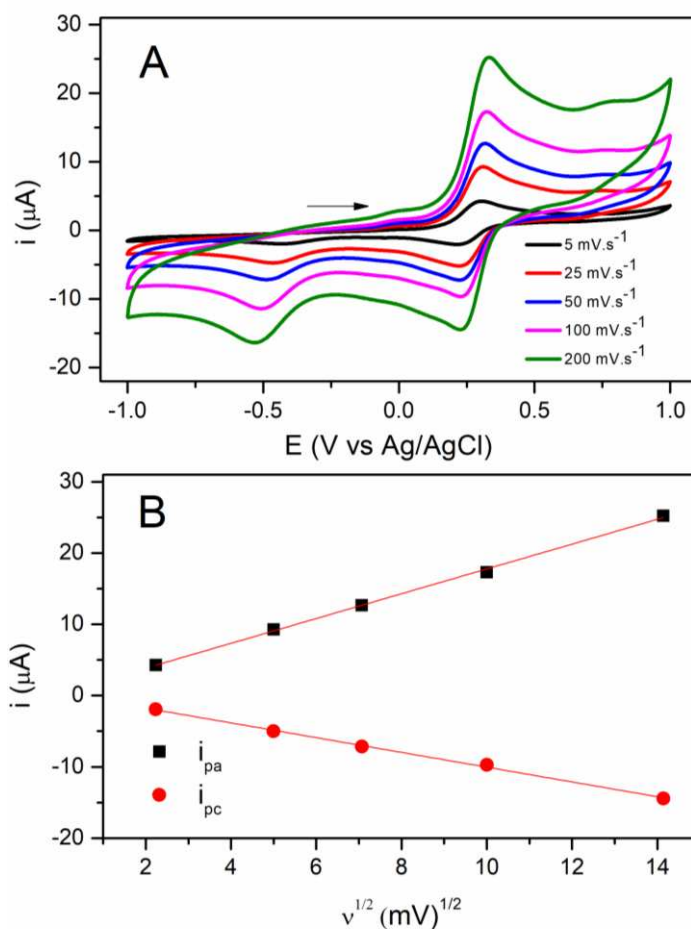


**Figure 12.** A) Cyclic voltammograms of  $2.0 \times 10^{-3} \text{ mol L}^{-1}$   $[\text{Fe}(\text{CN})_5(\text{ptt})]^{3-}$  aqueous solutions containing KCl  $0.1 \text{ mol L}^{-1}$  as supporting electrolyte at different scan rates. B) Current peaks of the iron redox process as a function of the square root of the scan rate.

**Table 2.** Parameters of the iron redox process obtained from cyclic voltammetry of  $\text{Na}_3[\text{Fe}(\text{CN})_5\text{NH}_3]$  complex.

$V$ ( $\text{mV.s}^{-1}$ )	$E_{pc}$ (V vs Ag/AgCl)	$E_{pa}$ (V vs Ag/AgCl)	$\Delta E_p$ (V)	$E_{1/2}$ (V vs Ag/AgCl)
25	0.257	0.049	0.208	0.153
50	0.290	0.033	0.257	0.162
100	0.329	0.007	0.322	0.168
200	0.380	-0.020	0.400	0.180

**Table 3** Parameters of the iron redox process obtained from cyclic voltammetry of  $\text{Na}_3[\text{Fe}(\text{CN})_5\text{ptt}]$  complexes.

$V$ ( $\text{mV}\cdot\text{s}^{-1}$ )	$E_{\text{pc}}$ (V vs Ag/AgCl)	$E_{\text{pa}}$ (V vs Ag/AgCl)	$\Delta E_{\text{p}}$ (V)	$E_{1/2}$ (V vs Ag/AgCl)
25	0.310	0.224	0.086	0.267
50	0.312	0.222	0.090	0.267
100	0.324	0.229	0.095	0.277
200	0.333	0.225	0.108	0.279

In order to evaluate the influence of pH in the redox processes of the complex, cyclic voltammetry studies were performed using solutions of  $[\text{Fe}(\text{CN})_5(\text{ptt})]^{3-}$  in Britton-Robinson buffer varying pH from 2.0 to 8.0. The oxidation or reduction of thiol groups occurs in the ptt molecule in a process influenced by the  $\text{H}^+$  concentration in the electrochemical cell. From the voltammograms (Figure 13), it is possible to observe that the redox potential of this ligand centered shifts to more negative values, whereas the metal centered redox process does not vary significantly. As the pH value increases, the redox activity of the ligand is diminished, until it is completely absent at  $\text{pH} = 10$ .

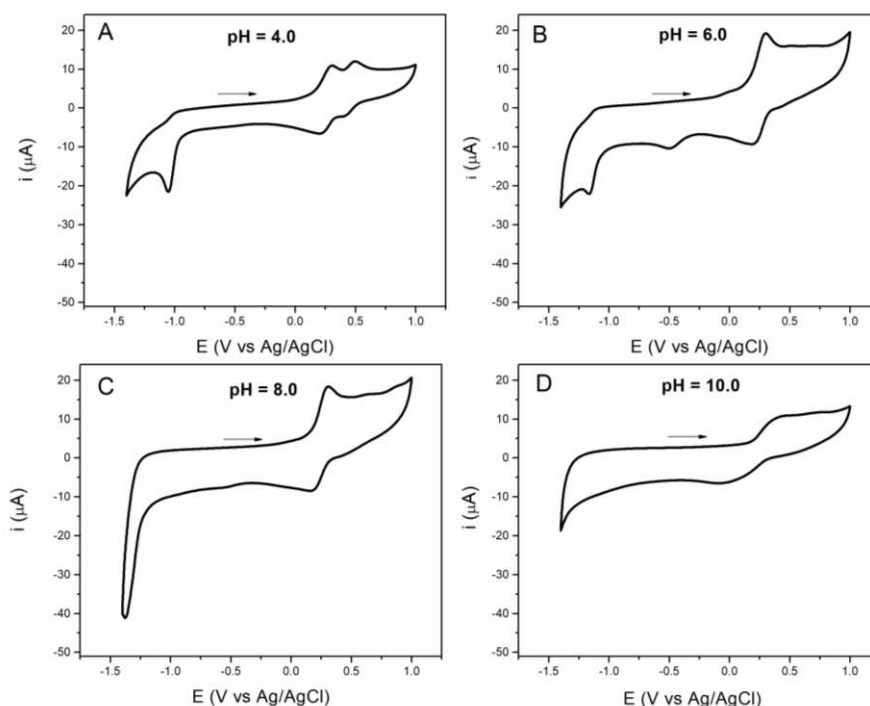


**Figure 13.** Cyclic voltammeteries of  $[\text{Fe}(\text{CN})_5(\text{ptt})]^{3-}$  in Britton-Robinson buffer solution in different pH values. Scan rate  $50 \text{ mv}\cdot\text{s}^{-1}$ .

#### 1.4.4 Electrochemical and spectroscopic properties of ECP-Fe(III)/Fe(II)/ppt

The ECP-Fe(III)/Fe(II)/ppt film was produced from the reaction of  $[\text{Fe}(\text{CN})_5(\text{ppt})]^{3-}$  with Fe(III) cations present in the solution, according to Equation 9.



The  $[\text{Fe}(\text{CN})_5\text{ppt}]^{3-}$  complex is chemically oxidized by sodium persulfate and reduced again in order to promote the reaction described in Equation 3. Cyclic voltammetry is used to produce the ECP-Fe(III)/Fe(II)/ppt structure on the surface of the electrode and to obtain film growth after several cycles. During this process, the insertion of potassium ions in the structure can occur and the films can lose the stability on the electrode <sup>[44]</sup>. Figure 14 shows voltammograms of FTO/PB and FTO/ECP-Fe(III)/Fe(II)/ppt using different cyanoferrate precursors in acidic conditions. It is worth mentioning that the PB films are typically stable in acidic conditions, however, in neutral and basic solutions they can be released from the working electrode.

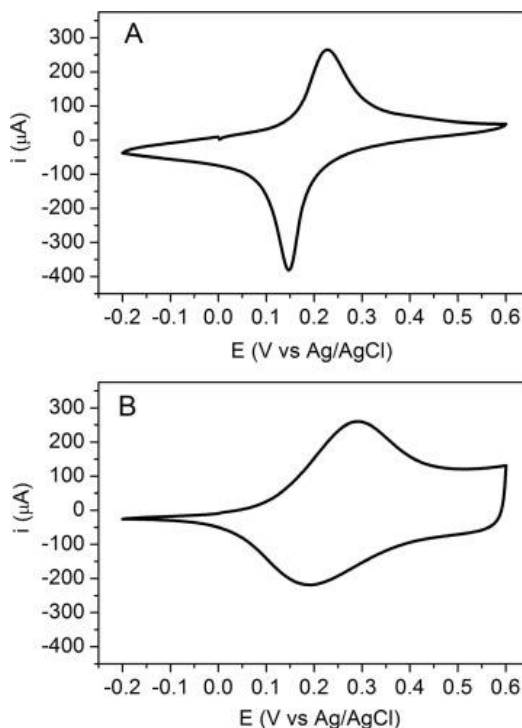


**Figure 14.** Cyclic voltammograms of FTO / PB modified electrodes using A) potassium ferricyanide and B) FTO / ECP-Fe(III)/Fe(II)/ppt as precursors in aqueous HCl 0.1 mol.L<sup>-1</sup>. Scan rate 100 mV.s<sup>-1</sup>. Supporting electrolyte KCl 0.1 mol.L<sup>-1</sup>.

The electrochemical profile observed corresponds to the conversion between Prussian blue (oxidized form) and Prussian white (reduced form) with  $E_0' = 0.19$  V and 0.24 V vs Ag/AgCl for PB and ECP-Fe(III)/Fe(II)/ptt, as represented in the well-known reduction of PB films:



The higher formal potential value is probably due to the influence of the N-heterocyclic ligand which remains coordinated to the iron redox center. Similar behavior was observed for PB films obtained from pentacyanidoferrate(II) containing isonicotinamide as a ligand [18]. The presence of the ligand (in the structure of the ECP-Fe(III)/Fe(II)/ptt) may also be associated with the low crystallinity of the structure produced from pentacyanidoferrates [17], as the N-heterocycles may interfere in the formation of the framework and produce structural defects. N. Ghasdian and collaborators showed that the higher the length of L in pentacyanidoferrate(II), the more amorphous is the metallopolymer obtained and consequently, the larger is the surface area analyzed by BET [17].

The thicknesses of the films were found to be 0.84 and 1.37 nm for PB and ECP-Fe(III)/Fe(II)/ptt, respectively, which are similar to values found in the literature [36]. This was confirmed by SEM, which showed that in FTO/PB the electroactive material was confined to isolated regions on the substrate. (Figure 15).

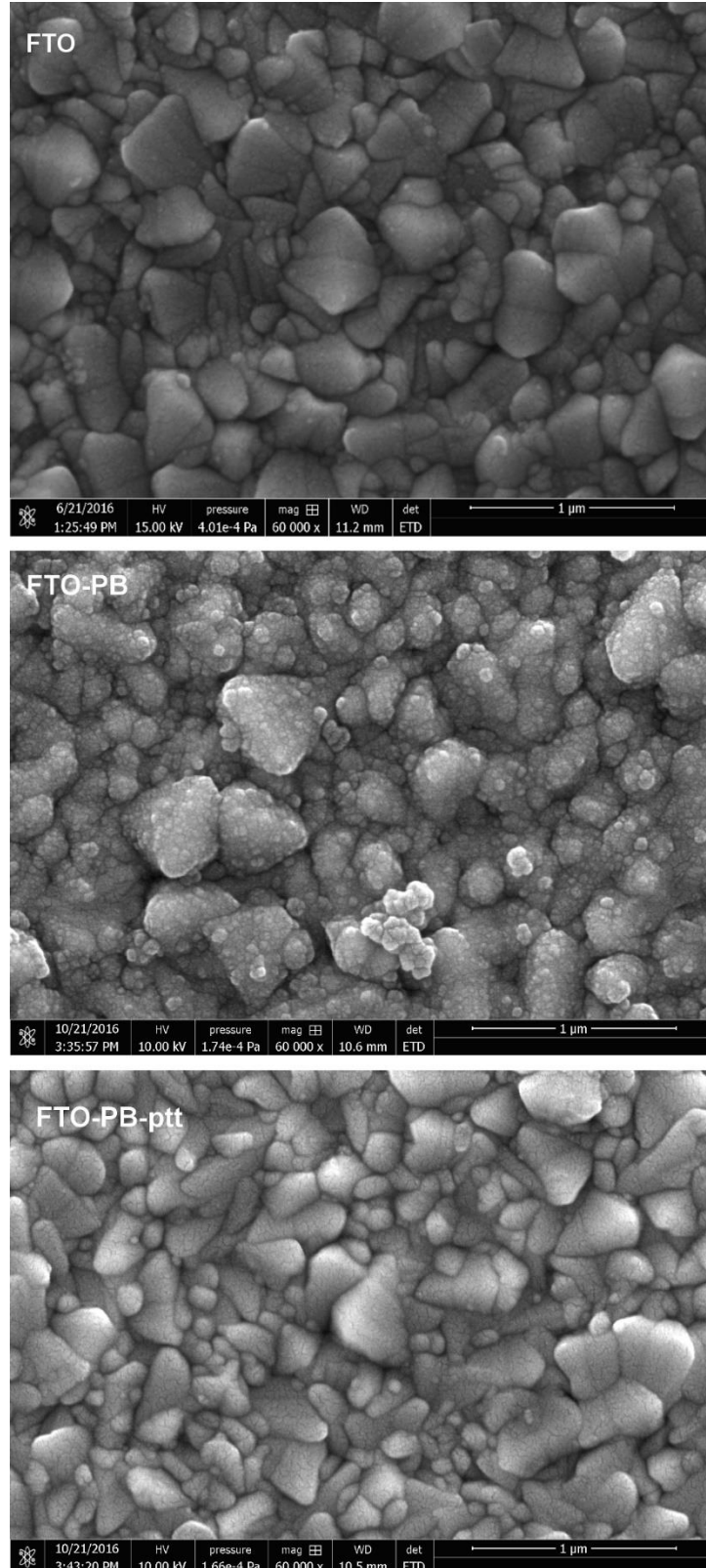


**Figure 15.** SEM micrograph of FTO, FTO modified by PB and ECP-Fe(III)/Fe(II)/ptt

An increase in surface area could represent an interesting feature of this new material. The stabilities of the films were evaluated by cycling the modified

electrodes in a solution containing HCl 0.1 mol L<sup>-1</sup> and KCl 0.1 mol L<sup>-1</sup>. After 50 cycles, 20 % of the ECP-Fe(III)/Fe(II)/ptt film was removed from the electrode surface, in contrast to PB film that lost 35 % of its initial electroactive material (Figure 16).

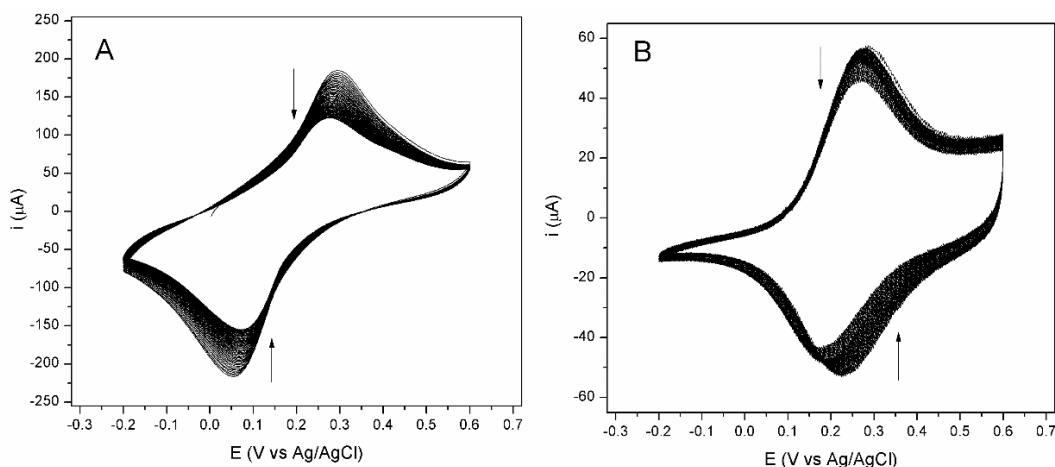


**Figure 16.** Stability of FTO electrodes modified with A) PB and B) ECP-Fe(III)/Fe(II)/ptt after 50 cycles in HCl 0.1 mol L<sup>-1</sup> and KCl 0.1 mol L<sup>-1</sup>.

The ECPs were also studied using electronic and vibrational spectroscopies. PB and ECP-Fe(III)/Fe(II)/ptt solutions were obtained by using equimolar amounts of FeCl<sub>3</sub> and cyanidoferrate complexes and their electronic spectra were obtained (Figure 17), where it is possible to observe intense absorptions attributed to an intervalence charge transfer in both compounds, indicating similar structures<sup>[18]</sup>. The increase in the absorbance maxima for the ECP-Fe(III)/Fe(II)/ptt is a result of the influence of the acceptor ligand on its structure, lowering the energy difference between the orbitals of iron centers, which are responsible for the intervalence charge transfer.

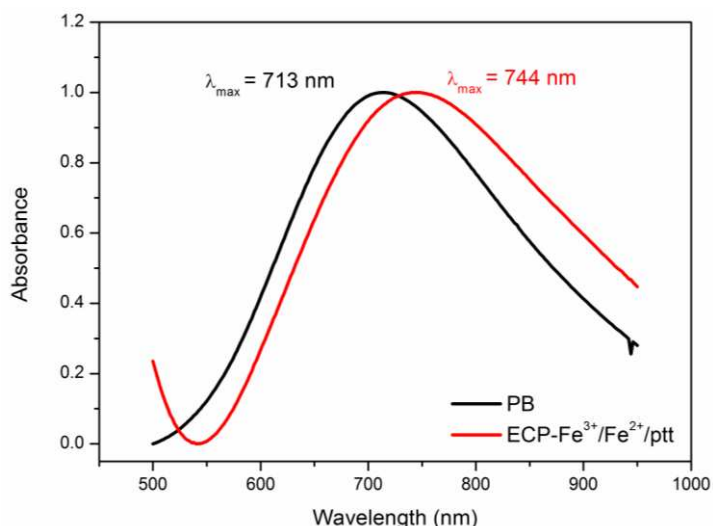


**Figure 17.** Normalized UV-Vis spectra of PB and ECP-Fe(III)/Fe(II)/ptt in water.

For the infrared spectroscopy experiments, an excess of iron was added to the solutions of cyanidoferrates, in order to obtain the insoluble form of the ECPs, which were separated by centrifugation. The results showed that ECP-Fe(III)/Fe(II)/ptt presents vibrational modes of the N-heterocyclic ligand, confirming its identity and the presence of this moiety in the material (Figure 18 and Table 4).

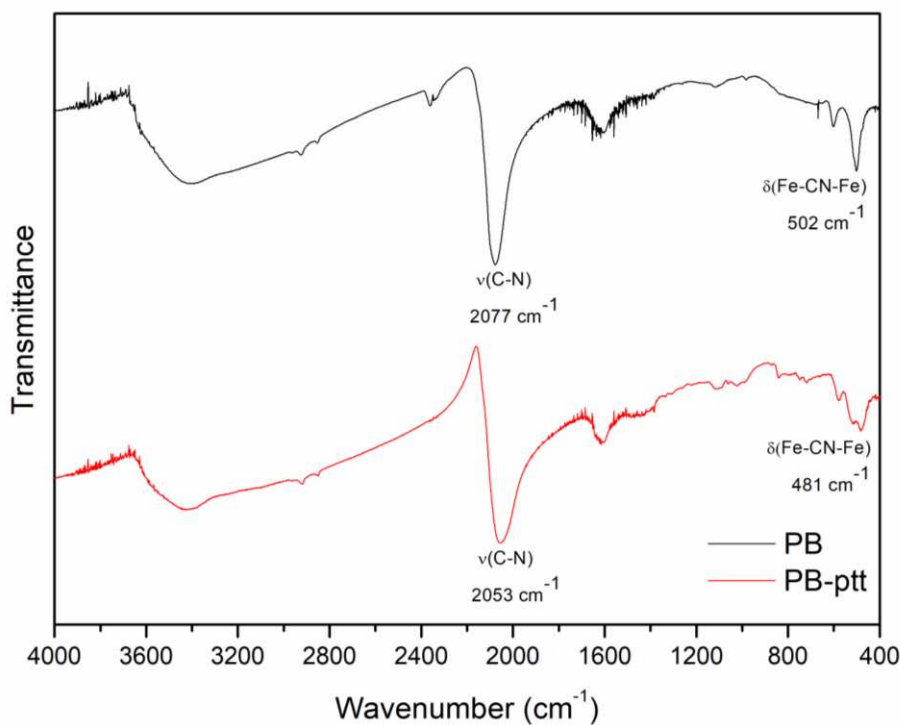


**Figure 18.** FTIR spectra of PB and ECP-Fe(III)/Fe(II)/ptt.

**Table 4.** Wavenumbers ( $\text{cm}^{-1}$ ) of PB and ECP-Fe(III)/Fe(II)/ppt obtained in FTIR spectroscopy.

<b>Assignment</b>	<b>PB</b>	<b>ECP-Fe(III)/Fe(II)/ppt</b>
$\nu(\text{OH})$	3409s	3418s
$\nu(\text{CN})$	2077vs	2053vs
$\delta(\text{H-O-H})$	1602m	1603m
ring deformation	-	1102w
$\delta(\text{Fe}^{\text{II}}\text{-CN-Fe}^{\text{III}})$	602, 502m	577, 481m

$\nu$  = stretching;  $\delta$  = in-plane bending; vs = very strong; s = strong; m = medium; w = weak;

XRD experiments of ECP-Fe(III)/Fe(II)/ppt were performed, however no diffraction peaks were observed. Thus, we concluded that the presence of the N-heterocycle introduced a high concentration of structural defects in the compound and this can be related to other features of the ECP modified electrodes such as the increment in the electroactive surface area of the modified substrates. Based on these results, we proposed the basic unit of ECP-Fe(III)/Fe(II)/ppt, which is presented in Figure 19, where  $[\text{Fe}(\text{CN})_5(\text{ppt})]^{3-}$  groups are connected in a 3D framework through iron atoms and cyanide groups. Due to the presence of ppt in the structure it is more difficult to create a regular structure as the ligand occupies a larger space than cyanide. Also, one of the PB network is interrupted in the positions where cyanide is substituted by the N-heterocycle.

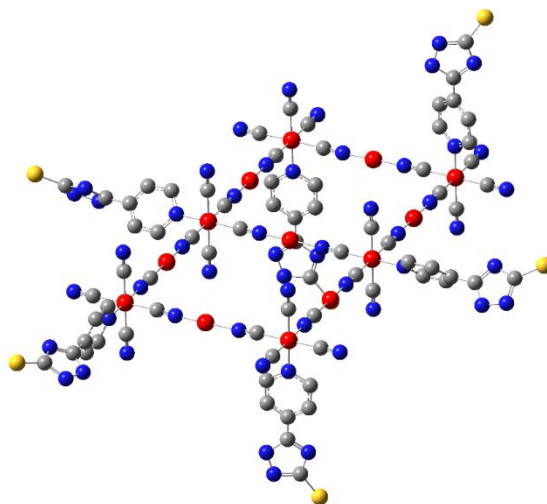


**Figure 19.** Basic structure proposed for ECP-Fe(III)/Fe(II)/ptt, with hydrogens omitted for simplification. Gray: carbon; Blue: nitrogen; Red: iron; yellow: sulfur.

#### 1.4.5 Electrochemical response of the ECPs towards hydrogen peroxide reduction

The comparison between the ECPs was conducted using the same hydrogen peroxide concentration range, analysis time and applied potential. As presented in Figure 20, ECP-Fe(III)/Fe(II)/ptt showed a linear response in the range of 70-450  $\mu\text{M}$ . On the other hand, the FTO/PB electrode showed a linear response in the range of 90-350  $\mu\text{M}$ . The sensibility values found were practically the same for the two electrodes ( $0.05 \mu\text{A} \cdot \mu\text{mol}^{-1} \cdot \text{L}^{-1} \cdot \text{cm}^{-2}$ ). The limits of detection calculated for the two different modifiers were 36 and 30  $\mu\text{mol L}^{-1}$  for PB and ECP-Fe(III)/Fe(II)/ptt, respectively. These results are compatible with the concentration range of several other electrochemical hydrogen peroxide sensors <sup>[45-47]</sup>. Thus, it is possible to assume that the ECP-Fe(III)/Fe(II)/ptt film has a very similar activity for the reduction of hydrogen peroxide when compared to the traditional PB film.

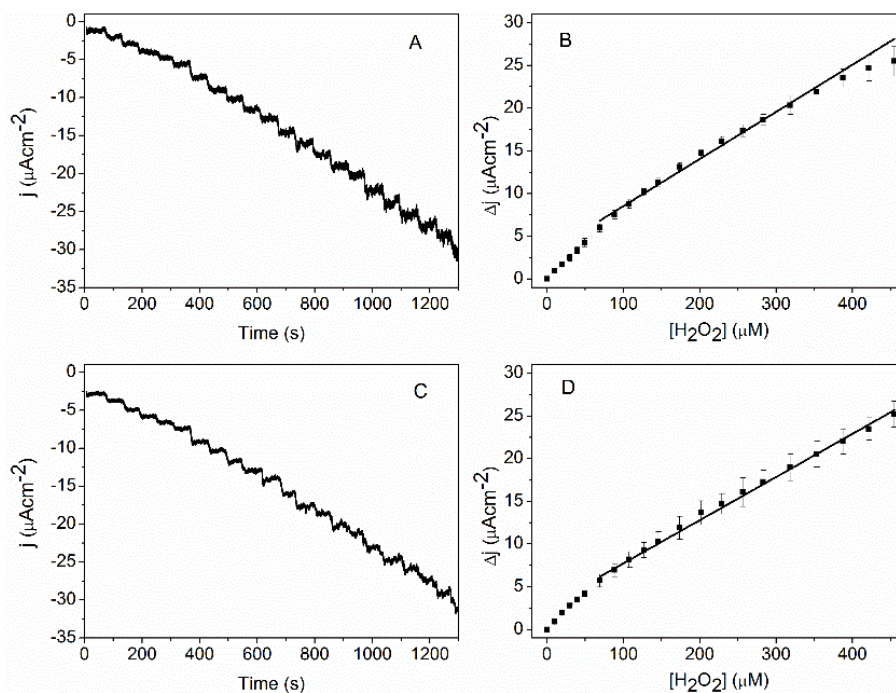


**Figure 20.** Amperometric response of A) FTO/PB and C) FTO/ECP-Fe(III)/Fe(II)/ptt electrodes after successive additions of  $5.0 \times 10^{-3} \text{ mol L}^{-1}$  hydrogen peroxide stock solution. The analytical curves obtained from the two measurements are presented in figures B) and D), for FTO/PB ( $R^2 = 0.986$ ) and FTO/ ECP-Fe(III)/Fe(II)/ptt electrodes ( $R^2 = 0.996$ ), respectively.

#### 1.4.6 Deposition of ECP-Fe(III)/Fe(II)/ptt on FTO/AuNP substrates and response towards the electroreduction of oxygen

Previous studies have demonstrated that pentacyanidoferrates(II) can produce coordination polymers under acidic conditions [26]. The same behavior is observed in the formation of Prussian blue from the acid solution of hexacyanidoferrate. In addition, it is known that gold nanoparticles can act like catalysts during the formation of Prussian blue from the decomposition of the cyanidoferrates precursors. Furthermore, the low interfacial pH due to the presence of aqueous  $\text{HAuCl}_4$  induces the precursor decomposition. The formation of gold oxide/hydrated oxide consumes  $\text{OH}^-$  ions, decreasing the local pH<sup>[48]</sup>.





The extinction spectrum of gold nanoparticles synthesized using the Turkevich method presented a maximum at 520 nm (Figure 21), corresponding to an average diameter of 20 nm. This can be stated due to this well-known synthetic method, but DLS experiments could also be used to determine the size distribution of these AuNPs<sup>[19]</sup>. The FTO electrodes were modified by AuNP, then immersed in a solution of  $[\text{Fe}(\text{CN})_6]^{4-}$  and  $[\text{Fe}(\text{CN})_5(\text{ptt})]^{3-}$  during 2h. According to the cyclic voltammetry experiments, only the  $[\text{Fe}(\text{CN})_5(\text{ptt})]^{3-}$  solution was able to produce a film on the surface of the electrode. The redox process observed at  $E^0 \sim 0.15$  V vs Ag/AgCl is attributed to the ECP-Fe(III)/Fe(II)/ptt / ECP-Fe(II)/Fe(II)/ptt redox pair, which indicates that deposition of the electroactive material occurred during the immersion step (Figure 22). The cyclic voltammogram of the electrodes immersed in potassium ferrocyanide showed no difference in the electrochemical profile when compared to the bare FTO, suggesting that there was no formation of PB on the surface of the electrode.

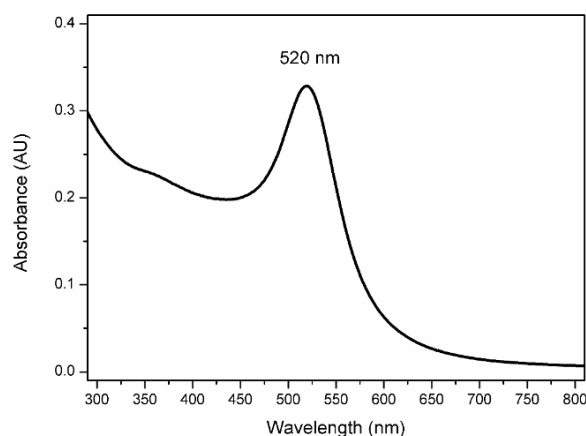


**Figure 21.** Extinction spectrum of gold nanoparticles produced using the Turkevich method.

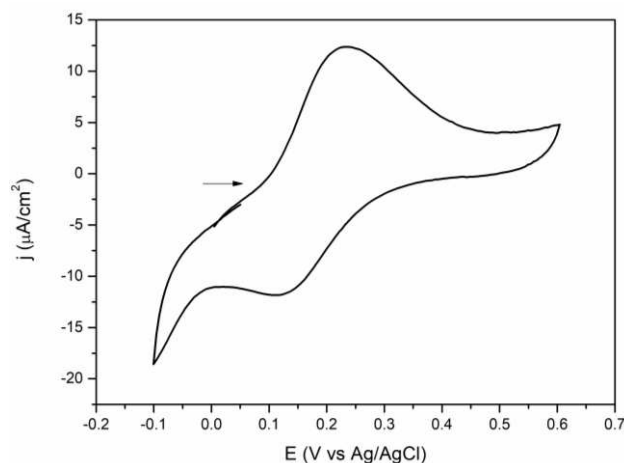


**Figure 22.** Cyclic voltammetry of FTO / AuNP/ ECP-Fe(III)/Fe(II)/ptt electrode produced by an immersion method in KCl 0.1 mol L<sup>-1</sup> aqueous solution. Scan rate: 100 mV.s<sup>-1</sup>.

In order to confirm the electrochemical activity of the modified electrode, a qualitative study of oxygen reduction was performed. The mechanism of the reduction of dioxygen by electroactive films of Prussian blue and their composites is well-understood [16,49]. First, it is necessary to reduce ECP-Fe(III)/Fe(II)/ptt to ECP-Fe(II)/Fe(II)/ptt. After this, the reduced form of the ECP acts as a redox mediator for oxygen reduction, producing the initial form and water as products, as described by Equations 13 and 14.



The results obtained for the ORR are presented in Figure 23. FTO showed low activity towards oxygen reduction (Figure 23 A), as expected [50]. An increase of current observed using the FTO electrode modified with AuNP can be associated to the increase of charge transfer between solution and the substrate (Figure 23 B). However, higher current density was obtained for the substrate FTO/AuNP containing ECP-Fe(III)/Fe(II)/ptt, as can be observed in Figure 23 C. A comparison of the electrochemical responses of the bare FTO, FTO + AuNP and FTO + AuNP + ECP-Fe(III)/Fe(II)/ptt is found in Figure 23 D.

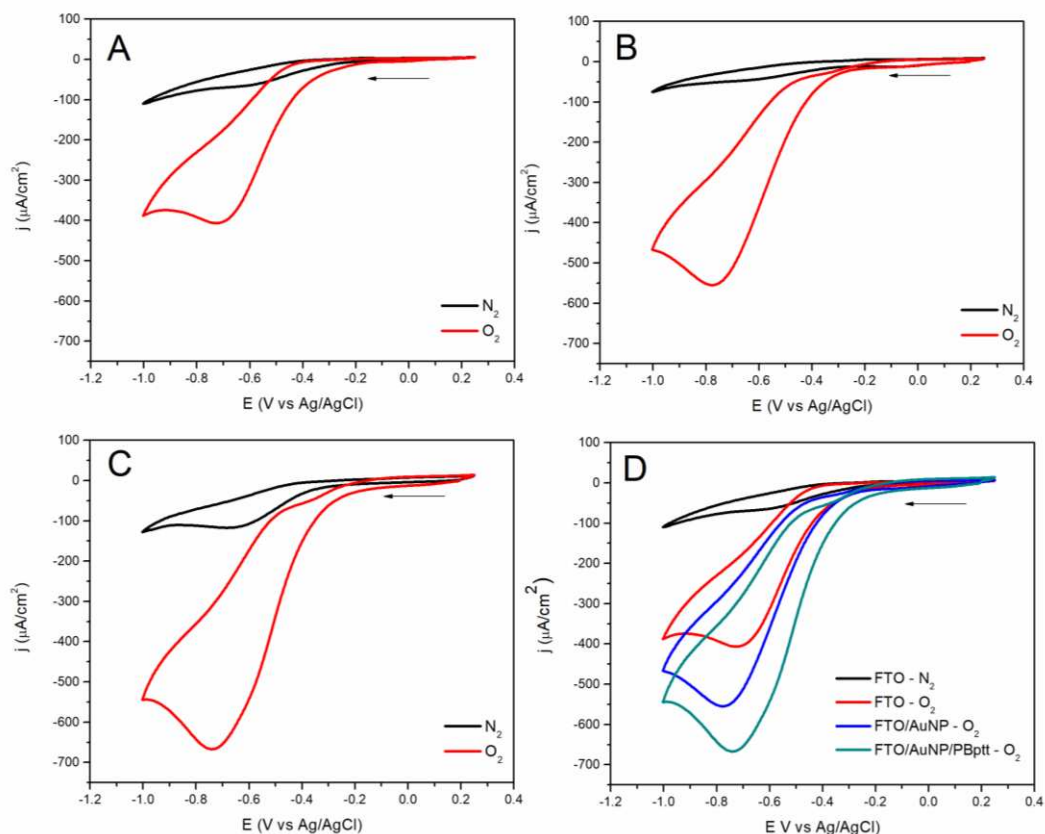


**Figure 23.** Electrochemical oxygen reduction by A) FTO; B) FTO + AuNP; C) FTO + AuNP + ECP-Fe(III)/Fe(II)/ptt; D) Comparison among the electrodes. Voltammograms obtained in KCl 0.1 mol L<sup>-1</sup> and scan rate of 50 mV.s<sup>-1</sup>.

The values reported in Figure 23 D are presented in terms of current density and indicate a better activity of the substrate modified with gold nanoparticles and the coordination polymer. In addition, the current density of oxygen reduction reaction obtained by ECP-Fe(III)/Fe(II)/ptt is increased by about 64% when compared to bare FTO and by 20 % when compared to FTO+AuNP. The charge transfer from the electrode to the solution started at a lower potential value for this substrate, suggesting a catalytic behavior of the film, as can be seen in Table 5. The onset potentials ( $V_{\text{onset}}$ ) for oxygen reduction obtained by cyclic voltammetry analysis showed that FTO/AuNP/ECP-Fe(III)/Fe(II)/ptt has an onset potential 80 mV lower than bare FTO.

**Table 5.** Onset potentials obtained by cyclic voltammetry analysis.

Substrate	Onset potential (V vs Ag/AgCl) ( $j = -1.5\mu\text{A}/\text{cm}^2$ )
FTO	-0.133
FTO/AuNP	-0.109
FTO/AuNP/ ECP-Fe(III)/Fe(II)/ptt	-0.053

The stability of the modified electrodes (FTO/AuNP/ ECP-Fe(III)/Fe(II)/ptt) towards oxygen reduction was evaluated by performing successive cyclic voltammetry scans, alternating nitrogen and oxygen purge in the electrochemical cell. Current peaks had a larger decrease (14%) between the first two scans, however, they stabilized in the following measurements (Figure 24 A). The behavior of the film was also evaluated after purging the solution with oxygen to saturate it and carrying out 50 successive scans. It was possible to observe the decrease of the current peak as oxygen was consumed from the solution and the stabilization of the current peak as oxygen in the solution equilibrated with oxygen from atmosphere (Figure 24 B).

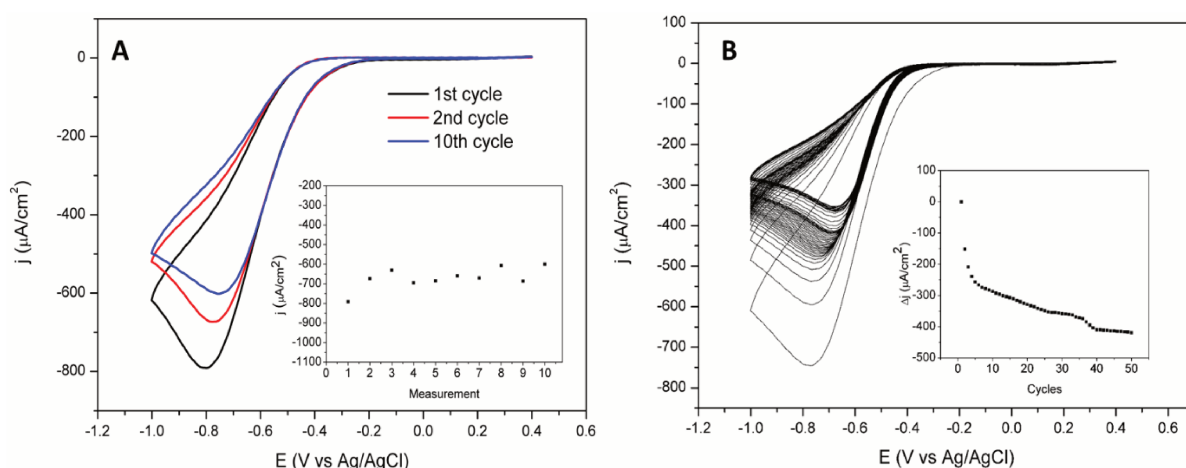


**Figure 24.** A) Stability of FTO/AuNP/ ECP-Fe(III)/Fe(II)/ptt electrodes used for oxygen reduction after successive measurements (alternating nitrogen and oxygen purge). Inset: variation of peak current densities after each measurement. Scan rate:  $50\text{ mV}\cdot\text{s}^{-1}$ ; B) Stability of FTO/AuNP ECP-Fe(III)/Fe(II)/ptt electrodes used for oxygen reduction after 50 successive cycles. Inset: variation of peak current density after each cycle. Scan rate:  $50\text{ mV}\cdot\text{s}^{-1}$

## 1.5 Conclusion

The coordination polymer (ECP-Fe(III)/Fe(II)/ptt) prepared from  $[\text{Fe}(\text{CN})_5(\text{ptt})]^{3-}$  showed formal potential about 50 mV higher than Prussian blue, which confirms the influence of the N-heterocycle over the properties of the ECP. In addition, the ECP-Fe<sup>3+</sup>/Fe<sup>2+</sup>/ptt presents a response to the electroreduction of hydrogen peroxide which is equivalent to Prussian blue, suggesting a catalytic response of the material. The synergistic effect between high surface area and the electrochemical activity of the ECP-Fe(III)/Fe(II)/ptt contributed to reach the catalytic effect observed that is represented by an increase of 64 % in the current density of reduction of oxygen and a decrease of 80 mV in the onset potential of oxygen reduction when compared to the bare FTO electrode.

## 2. Cobalt cyanidoferrates applied to oxygen evolution reaction (OER)

### 2.1 Introduction

#### 2.1.1 Energy situation and renewable fuels

Strategies to obtain new sources of green and sustainable energy that supply the global demand is a challenge for the scientific community. Energy demand of the world has grown particularly in developing countries due to industrialization and economic growth. The world energy demand by the year 2050 is anticipated to be in the range of 600–1000 EJ. Also, climate change is in evidence since the increase in frequency of weather calamities such as drought, heat waves, deluge and hurricanes are being observed. Recent reports have shown that these phenomena can be related to the increase of anthropogenic greenhouse gases<sup>[51]</sup>.

Many efforts have been made to develop substitutes to fossil fuels due to the emission of greenhouse gases and the limitation of their sources. In order to maintain CO<sub>2</sub> at acceptable levels, it is estimated that the generation of 12, 25 and 30 TW of carbon-free power is required to stabilize atmospheric CO<sub>2</sub> concentrations at 550, 450 and 350 ppm levels respectively by 2050. To reach this goal, a drastic change in the energetic technologies is required<sup>[51]</sup>

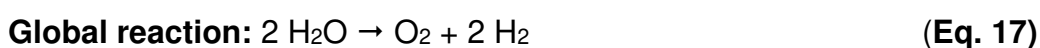
Among the possible alternative fuels, hydrogen can be considered of one the most advantageous, due to its high combustion efficiency, non-toxicity, clean exhaust products, renewable and storable nature<sup>[52]</sup>. The efficiency of hydrogen fuel cell vehicles is three times more than gasoline engines. Being a gas at normal pressures and temperatures, hydrogen also presents greater storage and transportation barriers than exist for the liquid fuels<sup>[51]</sup>. It was predicted that renewable resources share of 36% and 69% of the total global energy demand by 2025 and 2050 respectively, with hydrogen shares of 11% in 2025 and 34% in 2050. When hydrogen production technology receives moderate or strong support, the use of crude oil and coal will drop to 40.5% and 36.7%, respectively by 2030<sup>[53]</sup>.

Hydrogen can be obtained from different sources, but still is produced using coal, oil or natural gas. Production from renewable and sustainable energy sources, including electricity and biomass and have attracted interest, because it can avoid the production of CO<sub>2</sub> as it occurs in the fuel-based production. In this sense, we can highlight several processes that match the requirements of sustainability such as biomass gasification, fermentation, water splitting, photoelectrolysis and others. However, these methods are still not being used in large-scale hydrogen production. Furthermore, not all the hydrogen produced is applied in energy purposes<sup>[51]</sup>.

Hydrogen can be obtained effectively through light-driven or electrochemical oxidation of water, also known as water splitting reaction. Another possible way to obtain hydrogen is using the reforming of biomass<sup>[54]</sup>. Since water is a largely available resource in our planet, there is a large interest in using this fuel technology in transportation and portable power generation.

### 2.1.2 Electrochemical Water splitting

In water electrolysis, the hydrogen gas is produced and can be stored for later use. It consists of two half reactions, known as oxygen evolution reaction (OER) and hydrogen evolution reaction (HER).



Hydrogen and oxygen produced can be combined in a fuel cell, for example, to produce energy. The water oxidation reaction is both thermodynamically ( $E^0 = 1.23 \text{ V vs NHE}$ ) and kinetically demanding, and so requires a catalyst to be accomplished<sup>[55]</sup>. Water oxidation, in either acidic or alkaline conditions, is generally limited by the sluggish electrode kinetics associated with the OER at the anode rather by the cathodic hydrogen evolution reaction (HER)<sup>[56][57]</sup>.

At all pH values, the electrode potential for the four-electron, four-proton oxidation of water is substantially lower than that for some of the sequential one-electron steps. At pH 7, the one-electron potential for the oxidation of water to hydroxyl radical ( $\bullet\text{OH}$ ) is 2.32 V, over 1.5 V more positive than the potential for the four-electron concerted oxidation (0.815 V at pH 7).

In electrocatalysis, it is common to compare the efficiency of a catalyst by the overpotential ( $\eta$ ) of a redox reaction, which is the potential above the thermodynamic potential needed to overcome reaction barriers. It is referenced to a given turnover frequency or current density, which is also a very important tool to make benchmarking between different catalysts and methods.

$$\eta = E - E^0 \text{ (Eq. 18)}$$

According to the Nernst equation, the applied potential can be expressed as:

$$E = E^{0'} + \frac{RT}{nF} \ln \frac{C_O}{C_R} \text{ (Eq. 19)}$$

where  $E$  is the applied potential and  $E^{0'}$  is the formal potential of the overall reaction,  $T$  is absolute temperature,  $R$  is the universal gas constant,  $F$  is Faraday constant,  $n$  is the number of transferred electrons in the reaction, and  $C_O$  and  $C_R$  are the concentrations of oxidized and reduced reagents, respectively.

In an ideal world, the applied potential for driving a specific reaction should be equal to the potential of the reaction at equilibrium. In reality, it is always not the case since the applied potential commonly is much higher than that at equilibrium in order to overcome the electrode kinetic barrier of the reaction. The overpotential is commonly referred to a value that has to be applied to achieve a specified current density, and a lower overpotential of an electrocatalyst in the system indicates its superior electrocatalytic ability for the target reaction. Thus, different current densities are referred to different overpotential values.

In general, a smaller overpotential with a faster increase in corresponding current density ( $j$ ) is desired. The current density and the applied overpotential can be related according to the Butler–Volmer equation<sup>[56]</sup>:

$$\mathbf{i} = \mathbf{i}_0 \left[ \exp \left( \frac{nFE\alpha_a}{RT} \right) + \exp \frac{nFE\alpha_c}{RT} \right] \text{(Eq. 20)}$$

Under high anodic overpotential conditions, the overall current is mainly attributed to the anodic end while the contribution from the cathodic part is negligible. Accordingly, the Butler–Volmer equation can be simplified, which is also known as the Tafel equation<sup>[56]</sup>:

$$\mathbf{i} \cong \mathbf{i}_0 \exp \frac{nF\eta\alpha_a}{RT} \text{(Eq. 21)}$$

By translating the Tafel equation to a logarithmic function form, this equation can be re-written, where the exchange current density ( $i_0$ ) and Tafel slope ( $b$ ) can be calculated. The Tafel slope ( $b$ ) can be expressed as equation and from this one can understand that the definition of Tafel slopes “how fast the current increases against overpotential”<sup>[56]</sup> and its value mostly depends on the transfer coefficient ( $\alpha$ )<sup>[56]</sup>:

$$\log i = \log i_0 + \frac{\eta}{b} \text{(Eq. 22)}$$

$$b = \frac{\partial \eta}{\partial \log i} = \frac{2.307RT}{\alpha F} \text{(Eq. 23)}$$

In this regard, a smaller Tafel slope ( $b$ ) as shown in Figure 25 indicates that current density can increase faster with smaller overpotential ( $\eta$ ) change (i.e., faster reaction rate constant), which implies good electrocatalytic kinetics. In addition, Tafel slope provides valuable and insightful information toward the mechanism of the reaction, especially for elucidating the rate-determining step. This can be very helpful for understanding the fundamental behavior between electrocatalyst and reactant<sup>[56]</sup>.

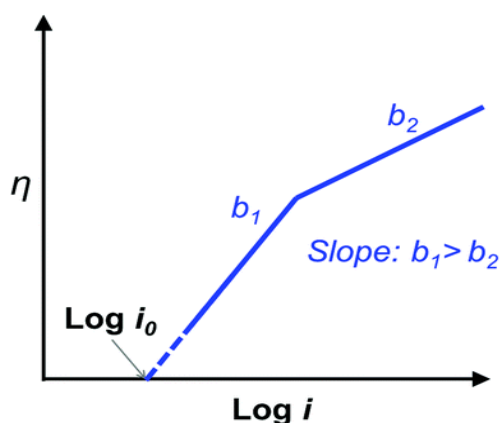


**Figure 25.** Plot of overpotentials as a function of the current densities, also known as Tafel plots. Higher slope region indicates worst kinetics, since the increment in current with the potential will be lower at a given overpotential<sup>[56]</sup>.

The report and comparison of the electrocatalytic activities is sometimes difficult because of different measurements methods. A lot of factors such as elemental composition, surface area, Faradaic efficiency, catalytic activity and stability are important comparison parameters. Faradaic efficiency (FE) should be considered since current densities in some cases may not contribute to the electrocatalysis of OER, which results in overestimating the efficiency of the electrocatalysts for OER. This point could be considered especially in a high oxidizing potential situation while the electrocatalysts or substrates (especially carbon-based materials) may suffer from phase transformation or decomposition. The control of FE can be performed by using probes in order to quantify  $\text{O}_2$  produced during the electrolysis<sup>[56]</sup>. Another point to be considered for catalysts is the surface area, especially for porous substrates. This may lead to errors in evaluating the catalytic ability of a material when deposited on different substrates.

Long term current stability (i.e. the ability of a catalyst to maintain OER current for a specified amount of time) is essential for practical water electrolysis. There are two main deactivation mechanisms, loss of catalyst material (e.g. by dissolution) and/or catalyst conversion to a less-active material (e.g. morphological and/or molecular structure changes). Long-term electrolysis can be performed by controlling the applied current or potential<sup>[58]</sup>.

### 2.1.3 Oxygen evolution reaction (OER)

In heterogeneous catalysts, only a small number of metal centers are active. Inactive sites are likely needed to keep the material intact by providing an environment around an active site that supports high oxidation states required for water oxidation, by acting as hole reservoirs, by assisting in deprotonations, or by tuning redox potentials. Ligands assume this role in molecular catalysts as polypeptide chains in biocatalysts. Robust, highly active, inorganic materials have largely regular, periodic structures, and only a few special sites are catalytically active, rendering their identification during turnover particularly challenging.

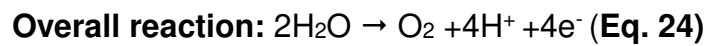
Reactions mechanisms can be investigated by using computational methods such as DFT or by kinetic studies. This can help understand the fundamental steps of the reaction and to design new catalysts<sup>[59]</sup>. However, none of the OER mechanisms proposed for heterogeneous catalysts has been yet fully validated based on experimental results. It was demonstrated that the Tafel slope, observable in an electrocatalytic measurement, is determined by the actual rate determining step (rds) within a certain reaction mechanism. However, a rds cannot unambiguously be identified based on the Tafel slope alone because different rds in different mechanisms can result in similar slopes. Furthermore, the Tafel experiment itself is a somewhat unspecific measure which can be altered by factors besides the electrocatalytic reaction. Thus, precise knowledge about the electrodes material properties especially with respect to conductivity and interfaces, is required in order to obtain valid mechanistic insights from a Tafel slope analysis<sup>[60]</sup>.

In order to determine the mechanism and the active phase responsible for the reaction, *in situ* experiments are commonly carried out. Nevertheless, very few operando experiments have been reported for OER to date, which is probably due to the challenges in measuring the heterogeneous junction between the electrode (immobilized electrocatalysts) and electrolyte when in solution. Also, this kind of research involves designing special devices which further increases the challenges of *in situ* experiments. There are few techniques that can provide such information on the surface of the electrocatalysts (structural and electronic states). For example, Fourier transform infrared spectroscopy (FTIR) and Raman spectroscopy have been demonstrated to achieve this goal. In addition, by using X-ray techniques, *in situ*

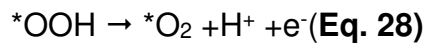
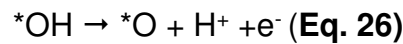
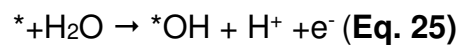
monitoring of electrocatalysts can be realized to probe materials for obtaining information such as oxidation states, coordination environment and crystal structure<sup>[56]</sup>.

The OER pathway is just a reverse version to of the ORR pathway. In the ORR process  $O_2$  is reduced into  $H_2O$  or  $OH^-$ , while in OER  $H_2O$  is oxidized to  $O_2$ . The mechanism of OER is very sensitive to the structure of electrode surface; different materials or one material with different facets can exhibit various reaction mechanisms. The generally accepted overall reaction pathways for OER involves four discrete electron transfer steps, which are<sup>[30]</sup>:

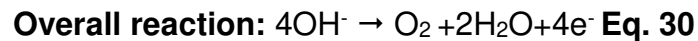
### Acidic solution



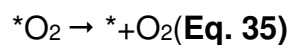
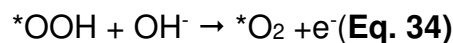
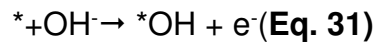
### Reaction pathway



### Alkaline solution:



### Reaction pathway:



### 2.1.4 Catalysts for OER

The most common catalysts used for water oxidation are platinum at the cathode and IrO<sub>2</sub> or RuO<sub>2</sub> at the anode, under acidic or alkaline conditions<sup>[61]</sup>. These materials have the drawback of low availability and high cost. Other metal oxide catalysts were also used in water electrolysis, specially containing transition metals from Groups 7, 8 and 9. Metal and non-metal oxides were able to produce current densities above 1 mA.cm<sup>-2</sup> in a wide range of overpotentials, depending on the substrate and preparation method<sup>[56]</sup>.

Many studies have been performed using earth-abundant metals as catalysts. Manganese oxides showed good results for the OER, with activity similar to noble metals<sup>[62]</sup>. Iron oxide water oxidation materials have also been heavily studied<sup>[63]</sup>. They appear as interesting materials for globally scalable, clean energy conversion applications because of the abundance and low cost of iron.

Cobalt oxide is also known to be stable mainly at high pH at high anodic potentials. However, Nocera *et. al* were able to produce a heterogeneous catalyst based on Co(II) phosphate (CoPi), which was formed *in situ* during electrodeposition on indium tin oxide, which was highly active for water oxidation and stable in phosphate buffer at pH 7<sup>[64]</sup>. Further work on this system demonstrated that Co(IV) was generated at potentials at which water oxidation occurred<sup>[65]</sup>. Cobalt-oxide water oxidation catalysts have received attention, especially in alkaline conditions, where Co<sub>3</sub>O<sub>4</sub> has shown good performance<sup>[66]</sup>.

Mechanisms of cobalt oxide-catalyzed water oxidation have also been studied and a possible mechanism is shown in Figure 26. Currently, there is broad consensus that two cofacial surface Co(O)OH moieties undergo two initial oxidations and deprotonations to generate terminal Co<sup>IV</sup> oxos. A peroxo species is produced on the surface, which converts to a superoxo intermediate that may be bridging. Addition of a second water molecule, together with loss of the fourth proton and electron, leads to O<sub>2</sub> release<sup>[59]</sup>.

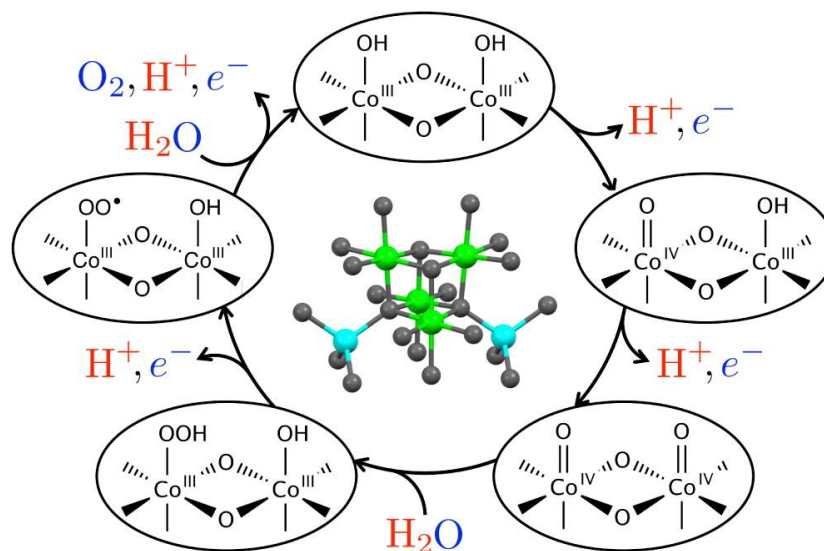


**Figure 26.** Mechanism of water oxidation using a cobalt oxide catalyst<sup>[59]</sup>.

Other transition metal oxides used for water oxidation with interesting results include nickel, scandium, vanadium, chromium, copper and zinc<sup>[59]</sup>. The challenges of developing catalysts for this reaction is to obtain materials that operate in low overpotential, strong oxidizing conditions, and with high stability, robustness and good cost-effectiveness. Furthermore, the characterization and benchmarking of the catalysts are difficult due to dependence of preparation methods, morphology and others<sup>[67]</sup>. In this sense, new catalysts are being pursued, and coordination polymers based on earth abundant metals appeared as good alternative materials for this application. Earth abundant electrocatalysts for OER in alkaline media have been extensively studied. Most of first row transition metal oxides of Co, Fe or Ni usually work well in alkaline media (pH > 13), but are instable at neutral and acid pH, where the water oxidation is easy to occur<sup>[68]</sup>.

Several strategies to stabilize metal oxide catalysts in neutral or acidic media have been attempted, for example a self-repairing process for the CoO<sub>x</sub> OER catalysts in neutral media in the presence of phosphate anions in the electrolyte (Co-Pi). In acid solutions, metal oxides may suffer from corrosion and some techniques have been developed to overcome this limitation. However, these methods are not suitable for large-scale processes. In the search for materials that meet the criteria required for the applications aforementioned, Prussian blue (PB) can be highlighted owing to its unique electrochemical properties.

### 2.1.5 Prussian-blue analogs (PBAs)

It is possible to obtain structures similar to the Prussian blue replacing iron by other transition metals, creating structures known as metal hexacyanidoferrates or Prussian blue analogs (PBAs). They have the general formula  $A_hM_k[Fe(CN)_6]_l \cdot mH_2O$  (h, k, l, m = stoichiometric numbers, A = alkali metal cation, M = transition metal ion) and represent an important class of mixed-valence compounds, of which Prussian blue is the classical prototype. These materials have interesting solid-state chemistry and structural attributes, which is reflected in their electrocatalytic, electrochromic, ion-exchange, ion-sensing, and photomagnetic properties<sup>[69]</sup>.

PBAs have been used in several studies for water splitting. One interesting approach is to use them as precursors of other more active catalysts, for example nickel hexacyanidoferrate that was used to produce Ni/Fe oxides with good activity<sup>[70][71]</sup>. However, their activity as main electrocatalyst have already been proved in several works. An example is cobalt hexacyanoferrate, which is robust and stable catalyst in a large pH range, exhibiting good activity towards the oxygen evolution reaction. Nevertheless, they need some improvements due to low mechanical resistance and current densities. Their catalytic behavior was tested by electrodepositing CoHCF on the surface of a FTO substrate and the results showed that the material remained active for water electrolysis after several hours at neutral conditions, being competitive with the traditional cobalt oxide catalyst<sup>[72]</sup>. An interesting strategy used by Galán-Mascarós et. al was to obtain films of CoFe using a template-assisted method, where a layer of cobalt hydroxide was grown on the surface of FTO substrates, which was used of a precursor for the coordination polymer using a thermochemical procedure (Figure 27). The obtained material showed good stability in a wide pH range and long term stability above  $j = 10mA.cm^{-2}$  for several hours<sup>[73]</sup>.

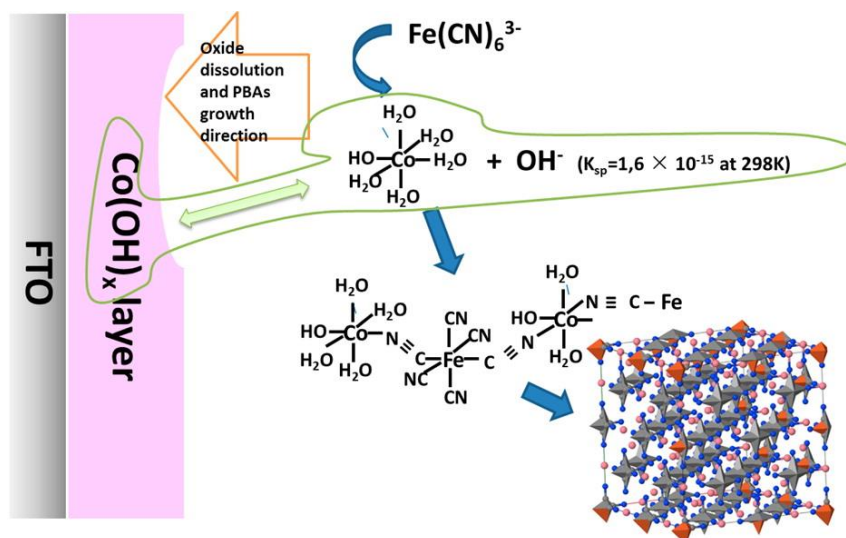


**Figure 27.** Obtention of the cobalt hexacyanidoferrate from a cobalt hydroxide layer<sup>[73]</sup>.

Jaouen *et. al* also used cobalt hexacyanidoferrate nanoparticles supported on a Sb-doped tin oxide substrate applied to polymer electrolyte membrane water electrolysis (PEMWE). The results showed that the materials provided high current densities in the range 50-100 mA.cm<sup>-2</sup> operating at 2.0 V vs RHE, which is comparable to traditional oxide materials. Interestingly, the loss of activity of the electrolyzer at higher potentials was assigned to the leaching of Sb from the substrate, suggesting that the Prussian blue analog might support high anodic potentials when required<sup>[74]</sup>.

Some recent works have explored the mechanisms involved in the oxidation of water using PBAs. The analysis of the reaction pathway was made using DFT calculations and infrared spectroscopy and a proposed mechanism is presented in Figure 28. Oxidation of water requires the proton coupled electron transfer (PCET) steps to afford the formal Co(IV)-oxo/Co(III)-O<sup>·</sup> moiety from the substrate-bound aqua center with a +2 formal charge. Once Co(IV)(O) is produced, it is attacked by water to create the O-O bond. Therefore, the structural and electronic properties of the Co(IV)(O)/Co(III)-(O<sup>·</sup>) center are usually the main focus of quantum chemical calculations<sup>[75]</sup>.

A study of water oxidation using a series of PBAs has come to some conclusions about these materials. The electron density of Co(II) is a decisive electronic criterion for achieving efficient water oxidation electrocatalysis, and this parameter may be tuned by changing the type of hexacyanidometal group. Also, the electron density of Co(II) can be reduced by increasing the oxidation state of the metal

ion of the  $[M(CN)_6]^{n-}$  group. Nucleophilic attack of water on the cobalt-oxo intermediate is considered the rate-determining step for water oxidation catalysis with PBAs (Figure 28)<sup>[75]</sup>.

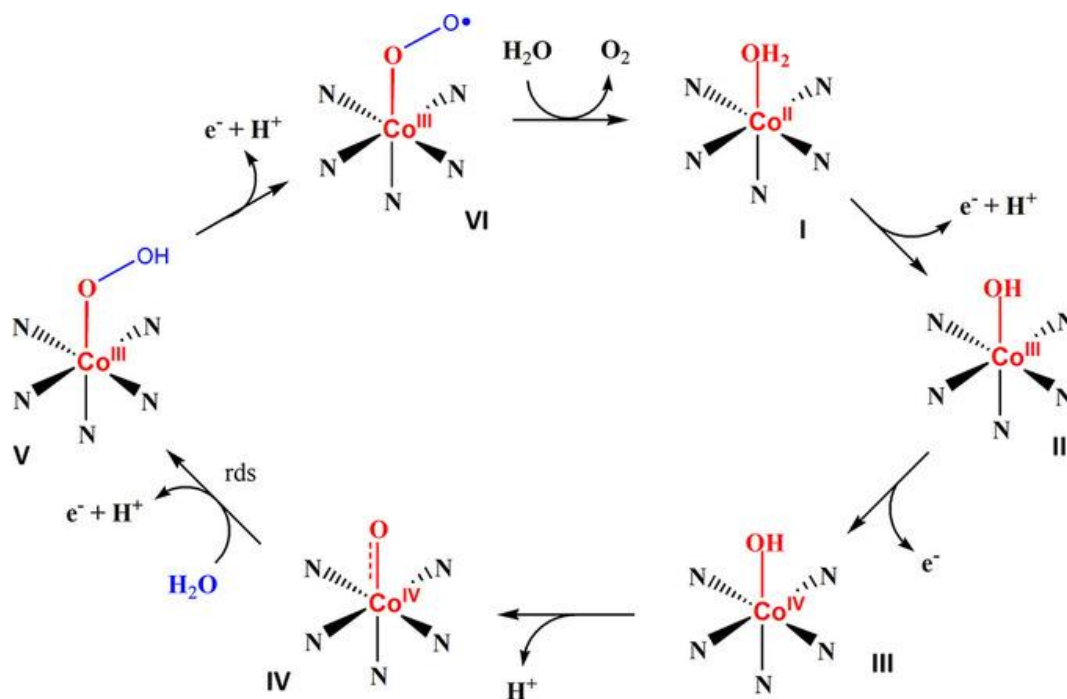


**Figure 28.** Proposed mechanism for water oxidation using cobalt-based PBAs<sup>[75]</sup>.

Despite their high turnover frequencies (TOFs), one of the main drawbacks of cyanide-based systems is their low concentration of electroactive cobalt sites. This is because of the relatively large distances between  $Co^{II}$  sites (ca. 10 Å) compared to oxide-based systems (ca. 3 Å). According to Karadas *et al*, metal cyanide networks are more advantageous regarding their stabilities, easy preparation methods, and competitive catalytic performances when compared to cobalt oxides. However, they still suffer from low current densities, which could be attributed to their low number of active Co sites. The main reason for the relatively low number of active sites in cyanide systems is that most of the Co sites in the crystalline framework are connected to six N atoms of the cyanide group except the ones on the surface and the atoms inside the vacancies created to provide charge balance. An interesting approach of his group was to use a pentacyanidoferrate-bound polymer as a precursor of Co-Fe PBAs

(Figure 29), which resulted in a dramatic decrease in the crystallinities of PBAs, and thus a significant increase in the surface concentration of Co sites<sup>[76]</sup>

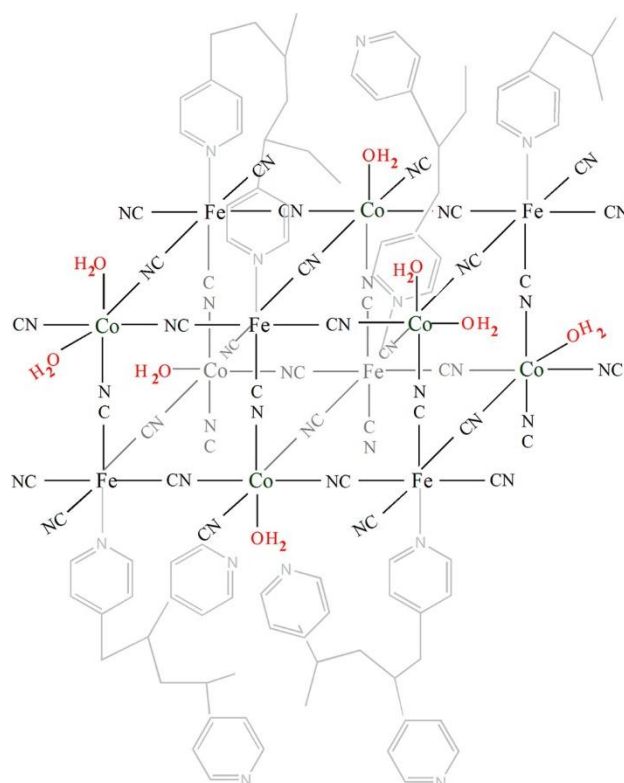


**Figure 29.** Structure of a PBA catalyst prepared from immobilization of a pentacyanidoferrate in a PVP framework<sup>[76]</sup>.

Because the conventional synthetic method to obtain PBAs, which involves the reaction of hexacyanidometallate complexes with transition-metal ions, leads to the formation of highly crystalline compounds, cyanide precursors other than hexacyanidometallate complexes should then be used. In this sense, the pentacyanidoferrate complexes appear as interesting starting points for this application.

## 2.2 Motivation

Considering that cobalt hexacyanidoferrates have shown interesting properties when applied to the electrochemical water splitting, one should consider the effects of a pentacyanidoferrate-based coordination polymer when applied in this reaction. According to previous results, the insertion of different ligands in the structure

may increase the electroactive surface area of the material. Also, one should consider the electronic effects of these ligands over the electrocatalysis, due to variation of electronic densities of the corresponding metals. In this study, a pentacyanidoferrate complex containing the isonicotinate ligand was used (Figure 30), and the corresponding Prussian blue analog was compared with the one produced using the traditional hexacyanidoferrate. Finally, the mechanism of water oxidation using a novel Prussian blue analog can be evaluated and compared with the traditional material.

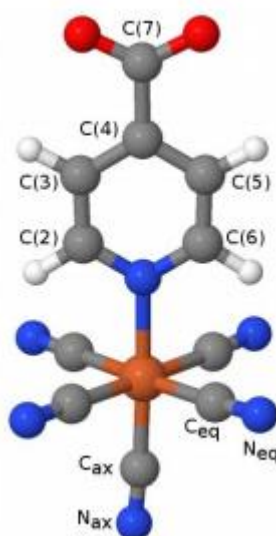


**Figure 30.** Optimized structure of the complex  $[\text{Fe}(\text{CN})_5(\text{isn})]^{4-}$  modeled by DFT calculations. Iron is shown in orange, carbons in gray, nitrogens in blue, oxygens in red and hydrogens in white<sup>[26]</sup>.

## 2.3 Experimental section

### 2.3.1 Synthesis of $\text{Na}_4[\text{Fe}(\text{CN})_5(\text{isn})] \cdot 5\text{H}_2\text{O}$ (isn = pyridine-4-carboxylate)

Isonicotinic acid ( $\text{C}_6\text{H}_5\text{NO}_2$ , Sigma–Aldrich; 0.12 g, 0.97 mmol) was neutralized by adding an aqueous solution of sodium hydroxide ( $\text{NaOH}$ , Synth; 0.0327 g, 0.82 mmol, 20 mL) to produce sodium isonicotinate. The solvent was removed in a rotary evaporator at 40 °C and then the salt was solubilized again in distilled water (20 mL). A sample of this solution (10 mL) was slowly added to an aqueous solution of  $\text{Na}_3[\text{Fe}(\text{CN})_5\text{NH}_3] \cdot 3\text{H}_2\text{O}$  (0.159 g, 0.5 mmol, 10 mL) with stirring. An orange color was

observed in the solution immediately after the addition of the first droplets. The flask was stirred for 30 min and the solvent was removed in a rotary evaporator at 25 °C. The orange precipitate obtained was dried on a vacuum line until constant weight, yield 82 %.  $C_{11}H_{14}FeN_6Na_4O_7$  (490.07): calculated. C 26.96, H 2.88, N 17.15; found C 26.77, H 2.87, N 17.92.

### 2.3.2 Preparation of chemically modified FTO electrodes

Before the electrochemical experiments, FTO substrates of 1 x 2.5 cm area were cleaned using isopropyl alcohol in an ultrasonic bath for 10 minutes, rinsed with distilled water, and cleaned again in a ultrasonic bath using distilled water for 10 minutes. After that, the substrates were annealed in an oven at 400 °C for 30 minutes. In the electrochemical experiments, the geometric areas of the substrates were limited to 1 cm<sup>2</sup>. A potentiostat Metrohm Autolab PGSTAT12 was used in the electrochemical experiments, except in the oxygen measurements. The experiments were performed using in an electrochemical cell using FTO as working electrode, saturated calomel electrode as reference electrode and a platinum wire as auxiliary electrode. The first step of the modification of the FTO substrates was the production of metallic cobalt films using a potentiostatic deposition. The electrolytic solution used in this step was 0.01 mol. L<sup>-1</sup> CoCl<sub>2</sub> containing 0.1 mol.L<sup>-1</sup> KCl as supporting electrolyte. A potential of -0.906 V vs SCE was applied in this cell until a charge of 66 mC cm<sup>-2</sup> was passed through the working electrode. After this step, a dark film was observed in the conductive side of the substrates. The following step was the production of cobalt hexacyanoferrates on the surface of the FTO/Co substrates. The electrolytic solution contained 0.01 mol.L<sup>-1</sup> of different cyanidoferrate (II) precursors (potassium hexacyanidoferrate or Na<sub>4</sub>[Fe(CN)<sub>5</sub>(isn)]) and a potential of 0.3 V vs SCE was applied for 6 hours<sup>[72]</sup>. After this procedure, the modified substrates were dried under vacuum before use in the next experiments.

### 2.3.3 FTIR spectroscopy

Infrared spectra of the modified substrates before and after their application in the electrocatalysis were obtained using a Agilent Cary 660 FTIR spectrometer in the reflectance mode, coupled to a Cary 610 FTIR microscope in the range of 4000-400  $\text{cm}^{-1}$ .

### 2.3.4 SEM microscopy

The morphologies of the samples were examined with a Quanta 250 field emission scanning electron microscope (FEI Co., USA) equipped with an Oxford X-MAX50 energy dispersive spectrometer (EDS) (Oxford, UK). The samples were mounted in a conductive carbon tape followed by carbon sputtered coating in a Bal-Tec MD020 instrument (Balzers).

### 2.3.5 XPS

The XPS spectra were obtained with a VSW HA-100 spherical analyzer and Al  $K_{\alpha}$  radiation ( $h\nu=1486.6$  eV). The high-resolution spectra were measured with constant analyzer pass energies of 44eV, (which produces a full width at half-maximum (FWHM) line width of 1.6 eV for the Au(4f<sub>7/2</sub>) line). The pressure during the measurements was always less than  $6.0 \times 10^{-8}$  mbar. The sample was fixed to a stainless-steel sample holder with double-faced conducting tape and analyzed without further preparation. Curve fitting was performed using Gaussian line shapes, and a Shirley background was subtracted from the data.

### 2.3.6 Electrochemical properties of the modified electrodes

Cyclic voltammetry was used to study the stability and activity of the modified substrates. In these experiments, the electrolytic solutions used were 0.05 mol.L<sup>-1</sup> phosphate buffer solution (PBS) pH 7.1 containing 1.0 mol.L<sup>-1</sup> KNO<sub>3</sub> (Aldrich)

as supporting electrolyte. The properties of the films were also studied by varying the phosphate solution pH adding phosphoric acid or potassium hydroxide solutions in the PBS stock. EIS experiments were performed using a 5 mM  $[\text{Fe}(\text{CN})_6]^{4-/3-}$  solution containing KCl  $0.1 \text{ mol.L}^{-1}$  as supporting electrolyte. The potential used was 0.27 V vs SCE with a frequency range of  $10^5$  to  $10^{-1}$  Hz.

### 2.3.7 Water oxidation studies

Water oxidation studies were performed in a two-compartment electrochemical cell with a glass frit separator. In one compartment the FTO modified substrates were inserted as working electrodes and the saturated calomel electrode as reference electrode. On the other compartment a platinum wire was used as counter electrode. In these studies the electrolytic solution used was PBS pH 7.1 containing  $\text{KNO}_3$   $1.0 \text{ mol.L}^{-1}$  as supporting electrolyte. Before starting the experiments, the uncompensated resistance of the system was measured using electrochemical impedance spectroscopy<sup>[58]</sup>. Values found were usually around  $20\Omega$  and the value was inserted in the NOVA software in order to calculate the  $iR$  drop. Tafel experiment were performed by applying different potentials ( $\eta = 0.23$  to  $0.63$  mV) during 30 minutes under stirring in the anodic compartment.

### 2.3.8 Oxygen evolution measurements

In this experiment, a Bio-Logic VMP3 multichannel potentiostat/Galvanostat was used to perform a cronopotentiometry experiment. A current density of  $0.2 \text{ mA/cm}^2$  was applied to the modified electrodes for 1 hour, with stirring. Oxygen evolution measurements were performed using a Ocean Optics Foxy luminescent probe. The amount of obtained oxygen was compared with the theoretical number of molecules produced, which can be estimated according to the total charge ( $Q$ ) that passed through the cell, according to Equation 36.

$$n_{\text{O}_2} = \frac{Q}{4F} \quad (\text{Eq. 36})$$

where  $F$  is the Faraday constant. The experiments were performed in a gas-tight cell containing PBS pH 7.1 and  $\text{KNO}_3$   $1 \text{ mol.L}^{-1}$  as supporting electrolyte.

## 2.4 Results and discussion

### 2.4.1 Electrochemistry of the modified substrates

Cyclic voltammograms of the modified substrates are presented in Figure 31. In the voltammograms of the modified FTO it is possible to observe typical processes of metal hexacyanoferrates. In both electrodes it is possible to observe typical redox processes of cobalt hexacyanoferrates such as a redox wave with  $E^{0'}$  = 0.96 V vs SCE assigned to the  $\text{Co}^{3+}/\text{Co}^{2+}$  redox pair in the presence of phosphate<sup>[64,77]</sup>. There are also redox waves with  $E^{0'}$  = 0.745 V vs SCE and 0.538 V vs SCE for FTO/CoHCF and FTO/CoFeisn respectively, which can be attributed to  $\text{Co}^{3+}/\text{Co}^{2+}$  when coordinated to water. Thus, we can assume that the N-heterocyclic ligand directly affects the redox activity of the catalytic site. In the FTO/CoFeisn electrode it is also possible to observe a strong redox wave at 0.28 V vs SCE, which is assigned to  $\text{Fe}^{3+}/\text{Fe}^{2+}$  redox pair<sup>[26]</sup> while in the FTO/CoHCF the same electrochemical process appears as a weak wave at 0.55 V vs SCE<sup>[78][79]</sup>. It is also possible to observe the water oxidation starting around 1.05 V vs SCE in both electrodes modified<sup>[73]</sup> with the cyanidoferrates, which does not occur in the bare electrode in the selected potential range. The attribution of the redox processes is also presented in Table 6.

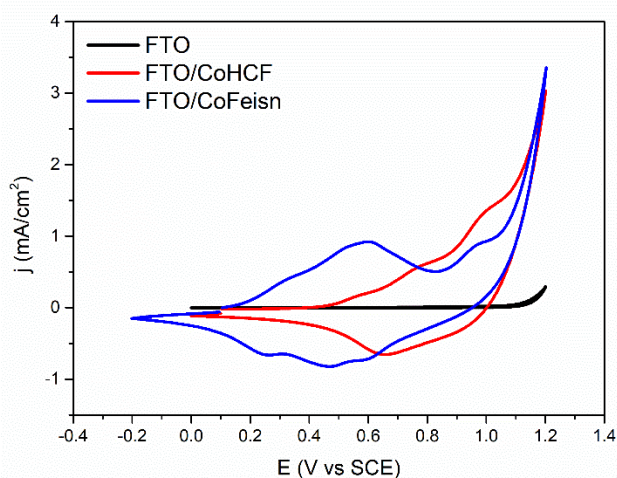


**Figure 31.** Cyclic voltammograms of bare and modified FTO substrates in PBS pH 7.1,  $\text{KNO}_3$  1.0 mol.L<sup>-1</sup>. Scan rate 50mV.s<sup>-1</sup>.

**Table 6.** Redox processes observed in the modified substrates obtained by cyclic voltammetry. Potentials in V vs SCE.

Redox process	CoHCF	CoFeisn
Fe <sup>3+</sup> /Fe <sup>2+</sup>	0.550	0.280
Co <sup>3+</sup> /Co <sup>2+</sup> (water ligand)	0.745	0.548
Co <sup>3+</sup> /Co <sup>2+</sup> (phosphate ligand)	0.960	0.960

Another important feature to be evaluated in the catalysts is the number of the active sites available on the surface of the substrate. In water oxidation using cobalthexacyanidoferrates, the cobalt atoms are considered the main active sites. Considering that it is possible to calculate the number of electroactive sites on the electrode surface using the cathodic current peak of the Co<sup>3+</sup>/Co<sup>2+</sup> redox process, according to Equation 37<sup>[35]</sup>:

$$i_p = \frac{n^2 F^2}{4RT} \Gamma \nu A \text{ (Eq. 37)}$$

Where  $i_{pa}$  is the peak current,  $n$  is the number of electrons involved in the redox process,  $F$  is the Faraday constant,  $R$  is the gas constant,  $T$  is the temperature,  $\Gamma$  is the electroactive surface coverage,  $\nu$  is the scan rate and  $A$  the electrode area. Thus, a plot of the current peak as a function of the scan rate provides a linear graph, which slope provides the value of the active surface for each electrode. Cyclic voltammograms of the modified electrodes were obtained in scan rates varying to 0.3 to 0.5 V.s<sup>-1</sup>. The results are presented in Figure 32. The average electroactive surface coverage found for the substrates were in the order of 1.0 and 6.0 nmol cm<sup>-2</sup> for FTO/CoHCF and FTO/CoFeisn, respectively, which indicates that more cobalt sites are available for the catalysis in the PB structure produced from the pentacyanidoferrate. This effect may be caused by the structural defects created due to the presence of the isonicotinate moiety on the structure<sup>[76]</sup>. A proposed structure of CoFeisn produced on the surface of the FTO substrate is presented in Figure 33, showing the possible defects created by the isn ligand in the material framework.

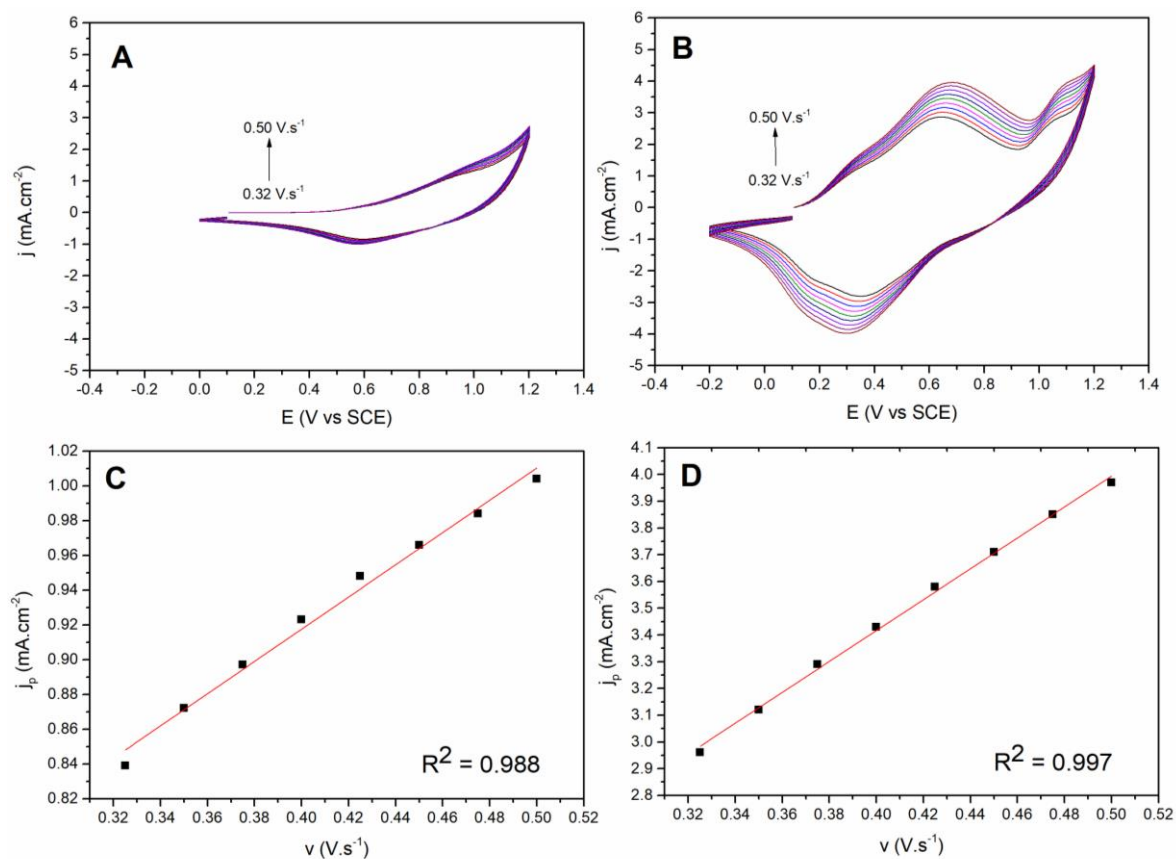


**Figure 32.** Cyclic voltammeteries of A) FTO/CoHCF and B)FTO/CoFeisn electrodes at different scan rates in PBS pH 7.1 and KNO<sub>3</sub> 1.0 mol.L<sup>-1</sup>.

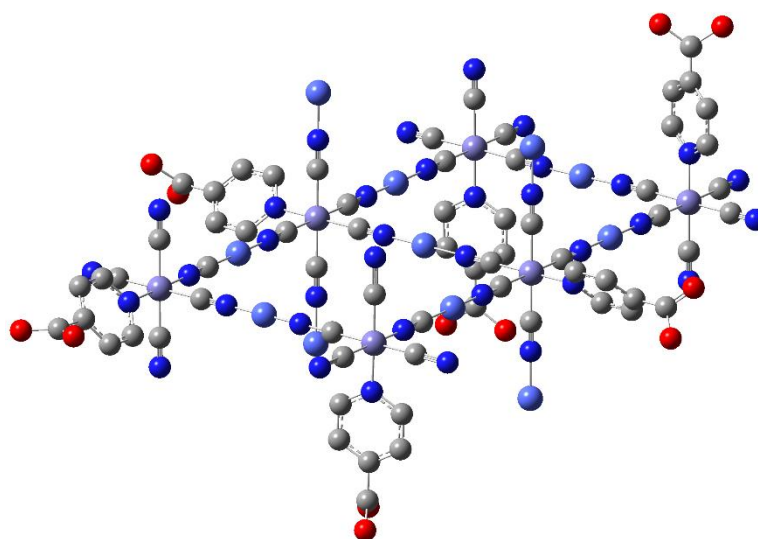


**Figure 33.** Proposed structure of CoFeisn deposited on FTO substrate. Fe: purple; Co: light blue; N: blue; C: gray; O: red.

The potential of electrochemical oxidation of water is depending on the pH of the solution, according to Equation 38<sup>[67]</sup>:

$$E = 1.229 - 0.059 \text{ pH (V vs NHE at } 25 \text{ }^\circ\text{C)} \text{ (Eq. 38)}$$

The effect of the pH was observed using the modified substrates, as presented in Figure 34. Water oxidation occurs with onset potentials higher than 1.0 V vs SCE in every pH range, with a very intense anodic current. Another interesting feature obtained from the voltammograms is the reversibility of the  $\text{Co}^{3+}/\text{Co}^{2+}$  redox pair, which varies significantly with the pH in both substrates. The separation of the peaks for this reaction increases above pH 7.0, indicating that the redox process is directly influenced by the concentration of  $\text{OH}^-$  species in the solution. Thus, it is expected that charge transfer between the electrode and the solution can occur faster in pH 7.0 or below. Also, at high pH conditions there is an extra oxidation peak, which also suggests different coordination spheres of the cobalt sites, probably alternating between  $\text{Co(II)-OH}_2$  and  $\text{Co(II)-OH}$ <sup>[75]</sup>.

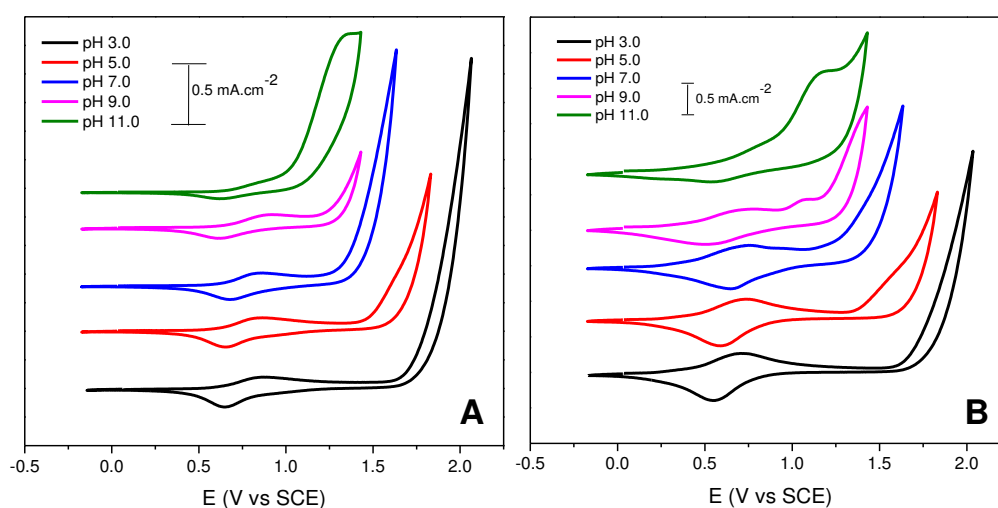


**Figure 34.** Cyclic voltammeteries of A) FTO/CoHCF and B) FTO/CoFeisn electrodes in different pH phosphate solutions. Scan rate  $50 \text{ mV}\cdot\text{s}^{-1}$ .

EIS results indicate that modification of the FTO surface affects drastically the charge transfer efficiency between the substrate and the electrolytic solution. The

equivalent circuits obtained by the analysis of the respective Nyquist plots (Figure 35) showed that, when compared to the bare electrode, FTO/CoHCF showed an increase in the charge transfer resistance ( $R_{CT}$ ), estimated to be  $134 \Omega$ , possibly due to the thickness of the film produced. On the other hand, the FTO/CoFeisn electrode presented the lowest  $R_{CT}$  value of the series ( $18.1 \Omega$ ), indicating that the thin film produced enhanced the charge transfer kinetics when compared to the bare substrate. The different structure of the modifier materials is also reflected in the circuits. Thickness of CoHCF film is higher enough to not allow one to observe the  $R_{CT}$  between the FTO and the cyanidoferrate layer and the result of the analysis is a single resistance. For the FTO/CoFeisn electrode, two different values were obtained by the Nyquist plots, also indicating that a thin film of the material was produced.

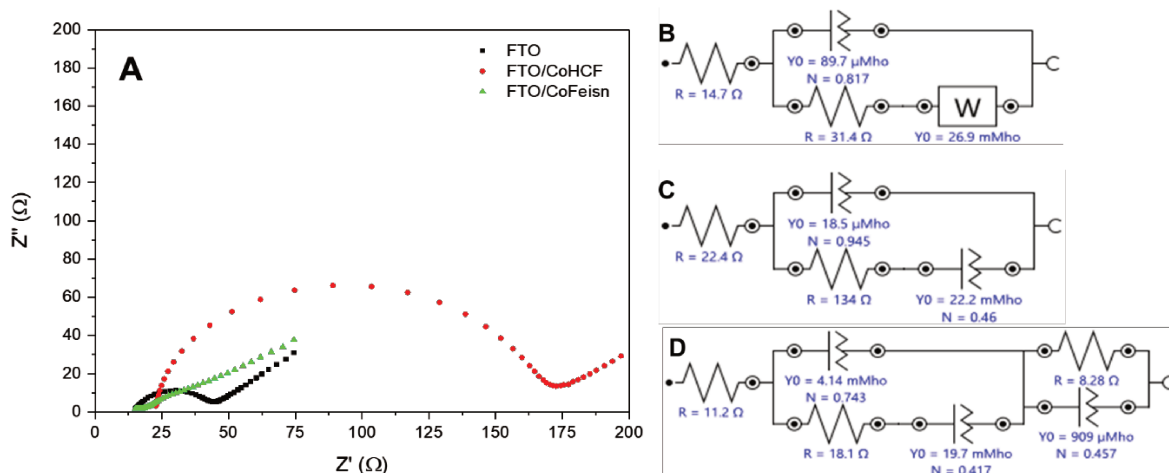


**Figure 35.** A) Nyquist plots obtained for the FTO modified substrates and equivalent circuits obtained for B) bare FTO, C) FTO/CoHCF and D) FTO/CoFeisn.

## 2.4.2 Water oxidation studies

Water can be electrochemically oxidized according to Equation 39 [72].



Efficiency of the catalysis using the modified FTO substrates was evaluated by obtaining the Tafel plots of water oxidation. The corresponding plots are presented

in Figure 36, where it is possible to observe a linear behavior between  $\eta = 0.3$  and  $0.46$  mV, with Tafel slopes of  $132$  and  $146$  mV.dec<sup>-1</sup> for FTO/CoHCF and FTO/CoFeisn respectively. These values indicate that the mechanism of water oxidation using these materials are similar<sup>[75]</sup>, although it is difficult to interpret which pathway occurs for the reaction since surface intermediates, coverage, mechanisms and rate determining steps cannot be stated only from this analysis<sup>[80]</sup>. Also, current density produced using the pentacyanidoferrate (II) precursor was higher than the hexacyanidoferrate at same overpotential values. As discussed before, one of the reasons for this enhancement of current density can be the higher number of cobalt active sites available for the catalysis.

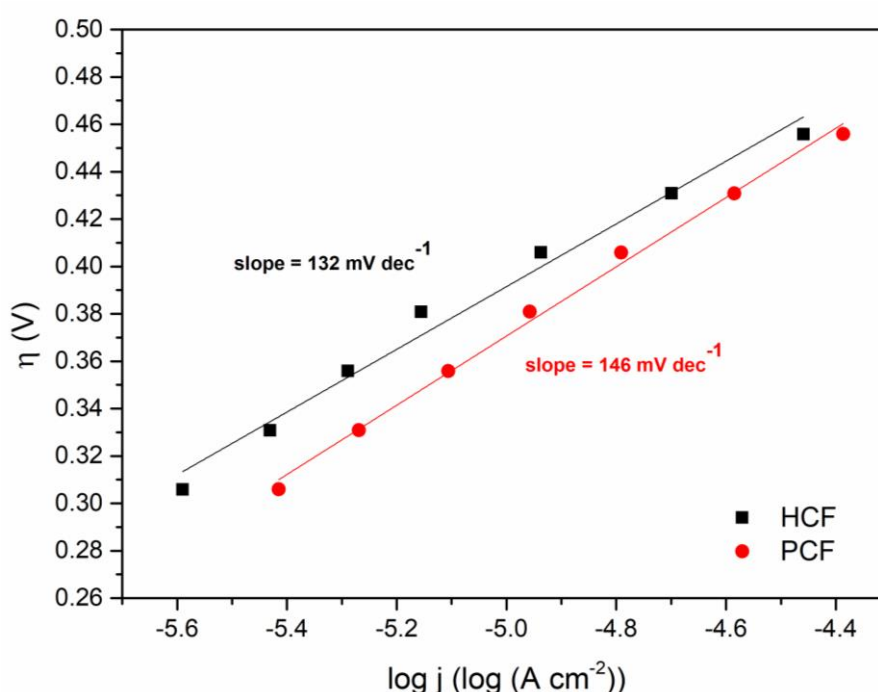


**Figure 36.** Tafel plots of the modified FTO substrates applied to water oxidation.

Figure 37 presents vibrational spectra of the modified substrates obtained before and after applying a potential of  $1.2$  V vs SCE for 1 hour. Both modifiers present strong absorptions at  $2072$  and  $2064$  cm<sup>-1</sup> for FTO/CoHCF and FTO/CoFeisn respectively, which are assigned to cyanide stretching and are very common in Prussian blue analogs. The lower wavenumber value observed of this stretching for the FTO/CoFeisn electrode also reflects a lower number of cyanides bridges in the structure<sup>[27]</sup>. The broadness of the peak in FTO/CoFeisn also indicates that there are more variations in the coordination modes of the iron center, which affects the

electronic density of the metal and the vibrational frequency of the cyanide groups. Furthermore, one should consider that water can partially replace the isonicotinate molecule in the pentacyanidoferrate moiety. After the catalytic tests, it is possible to conclude by the infrared spectra that the structure of the modifier in FTO/CoHCF varies drastically. A new peak appears at  $2123\text{ cm}^{-1}$  as a result of partial oxidation of cobalt sites<sup>[76]</sup> and the initial peak shifted to higher wavenumbers. Lezna *et al.* described a similar behavior in thin CoHCF films, including a participation of potassium cations in the redox process<sup>[81]</sup>. In FTO/CoFeisn this shift also occur, but interestingly the cyanide absorption peak became sharper, indicating that some of the possible coordination modes of iron were lost during the reaction. The peak corresponding to oxidized cobalt in the FTO/CoFeisn electrode after the catalysis was not observed, which may be due the low thickness of CoFeisn films<sup>[81]</sup>.

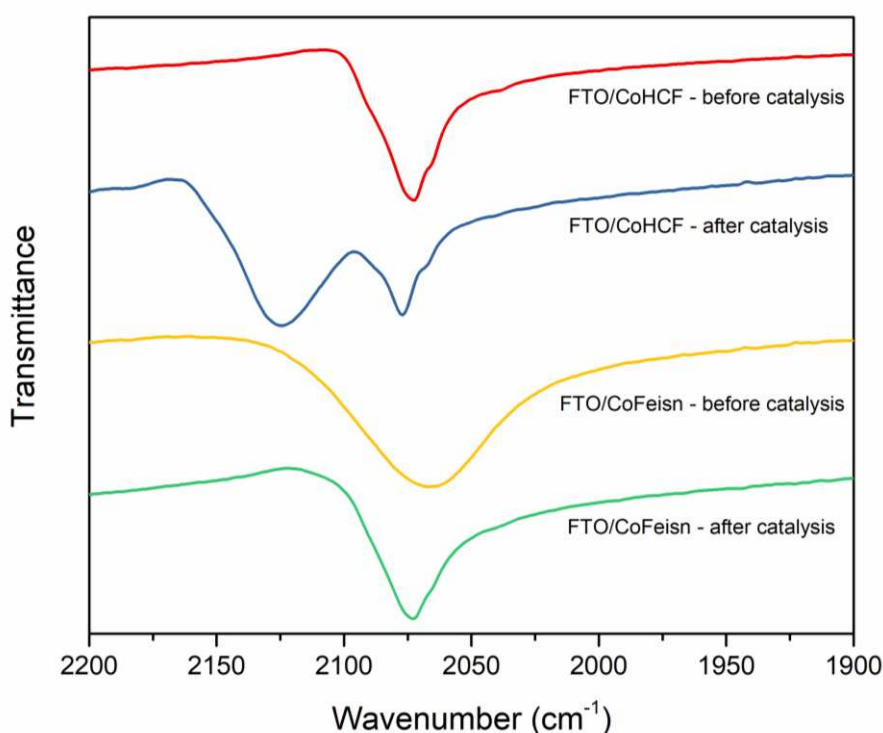


**Figure 37.** FTIR spectra of the modified substrates before and after application in electrochemical water oxidation.

XPS was also used to find more information about the oxidation states of the metal centers and evaluate the effect of the electrolysis. The analysis of iron shows that in both substrates (Figure 38 and Figure 40) it was possible to observe peaks with maxima around 721 and 708 eV, assigned to  $\text{Fe}_{2p1}$  and  $\text{Fe}_{2p3}$ , respectively<sup>[81]</sup>. This

confirm the presence of iron (II) from the cyanidoferrate moieties indicating that the precursors maintain their redox state after the formation of the cobalt hexacyanidoferrate framework. The cobalt range was also evaluated (Figure 39 and Figure 41) and the results indicated that cobalt (III) was present in all the structures due to peaks maxima around 796 and 786 eV, assigned to  $\text{Co}_{2p1}$  and  $\text{Co}_{2p3/2}$ , respectively [81,82]. These results suggest that a partial oxidation of the cobalt sites occur in the formation of the coordination polymer. The spectra of the substrates before and after application in water electrolysis were very similar, indicating that the materials have an interesting redox stability.

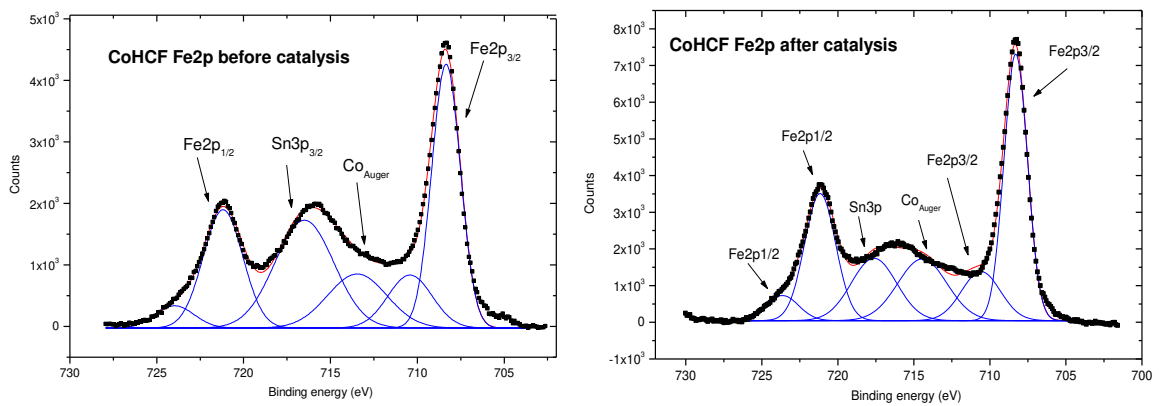


**Figure 38.** XPS spectrum of the Fe 2p range of FTO/CoHCF electrode before and after water electrolysis.

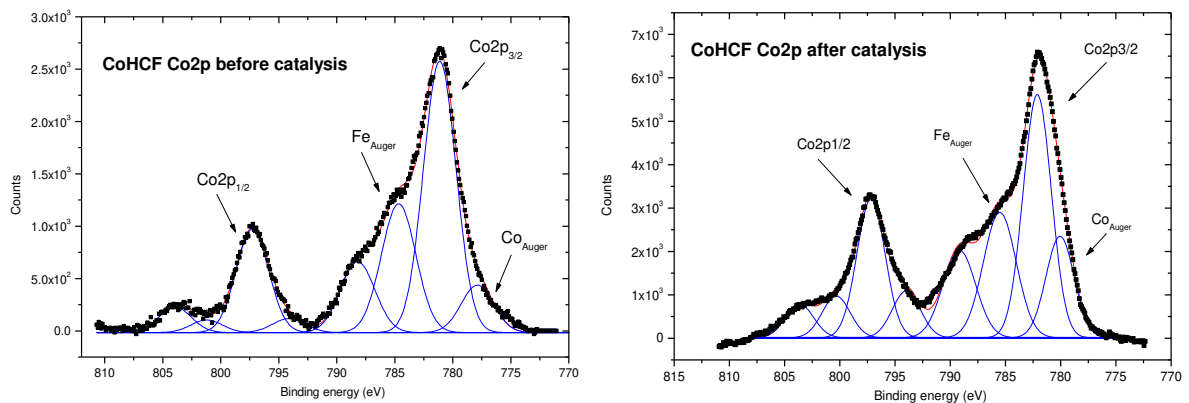


**Figure 39.** XPS spectrum of the Co 2p range of FTO/CoHCF electrode before and after water electrolysis.

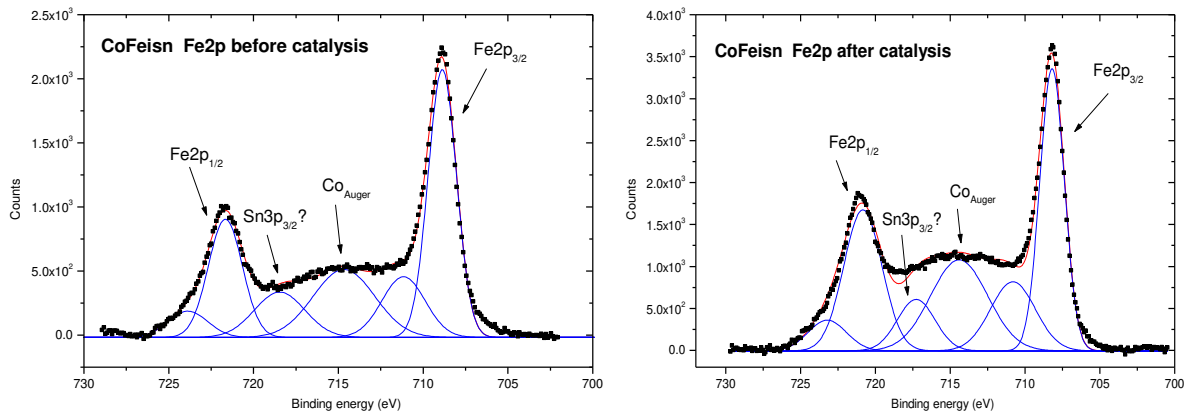


**Figure 40.** XPS spectrum of the Fe 2p range of FTO/CoFeisn electrode before and after water electrolysis.

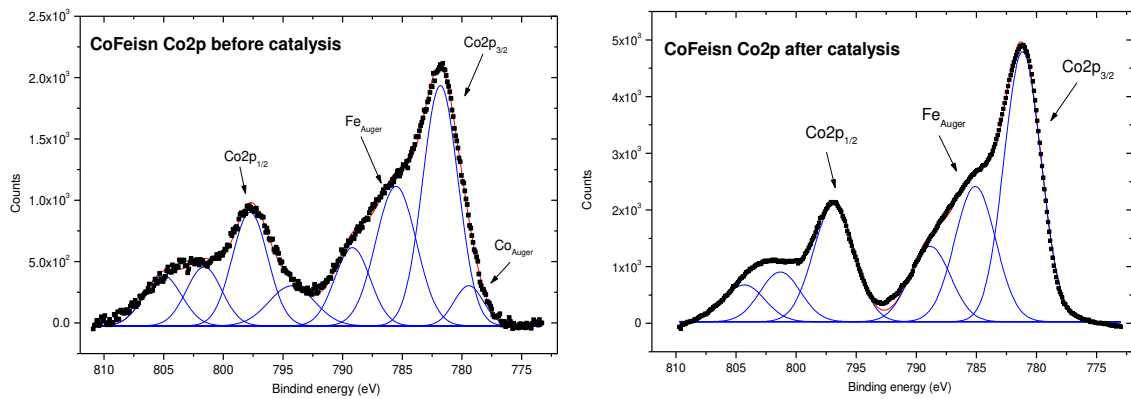


**Figure 41.** XPS spectrum of the Co 2p range of FTO/CoFeisn electrode before and after water electrolysis.

The effect of the catalysis was also evaluated using scanning electron microscopy. For both modified substrates, EDX analysis before the electrocatalysis showed that the catalysts were confined in some regions on the surface of FTO, as shown by Figure 42 and Figure 43.

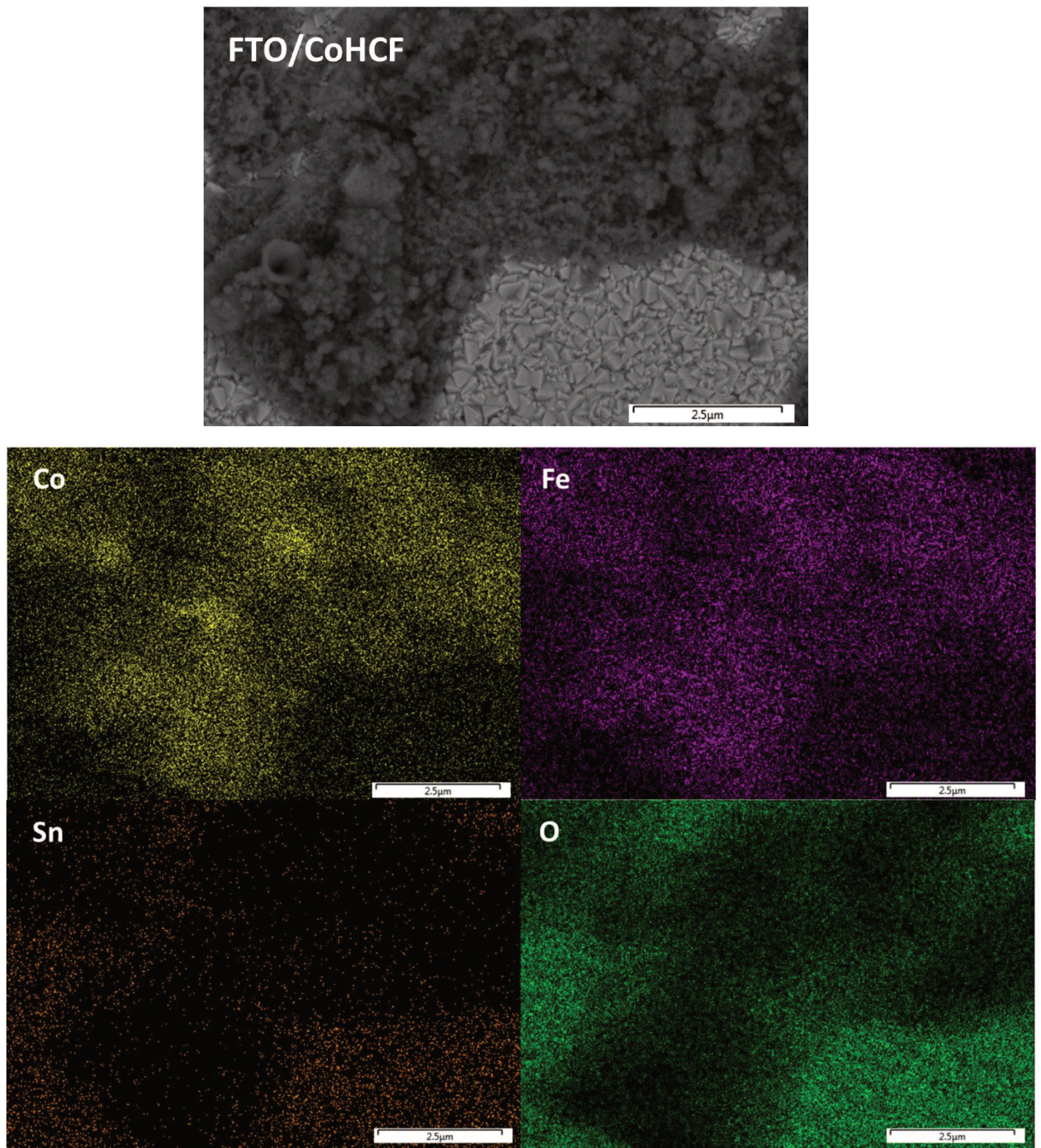


**Figure 42.** SEM micrographs and EDS analysis of FTO/CoHCF electrode.

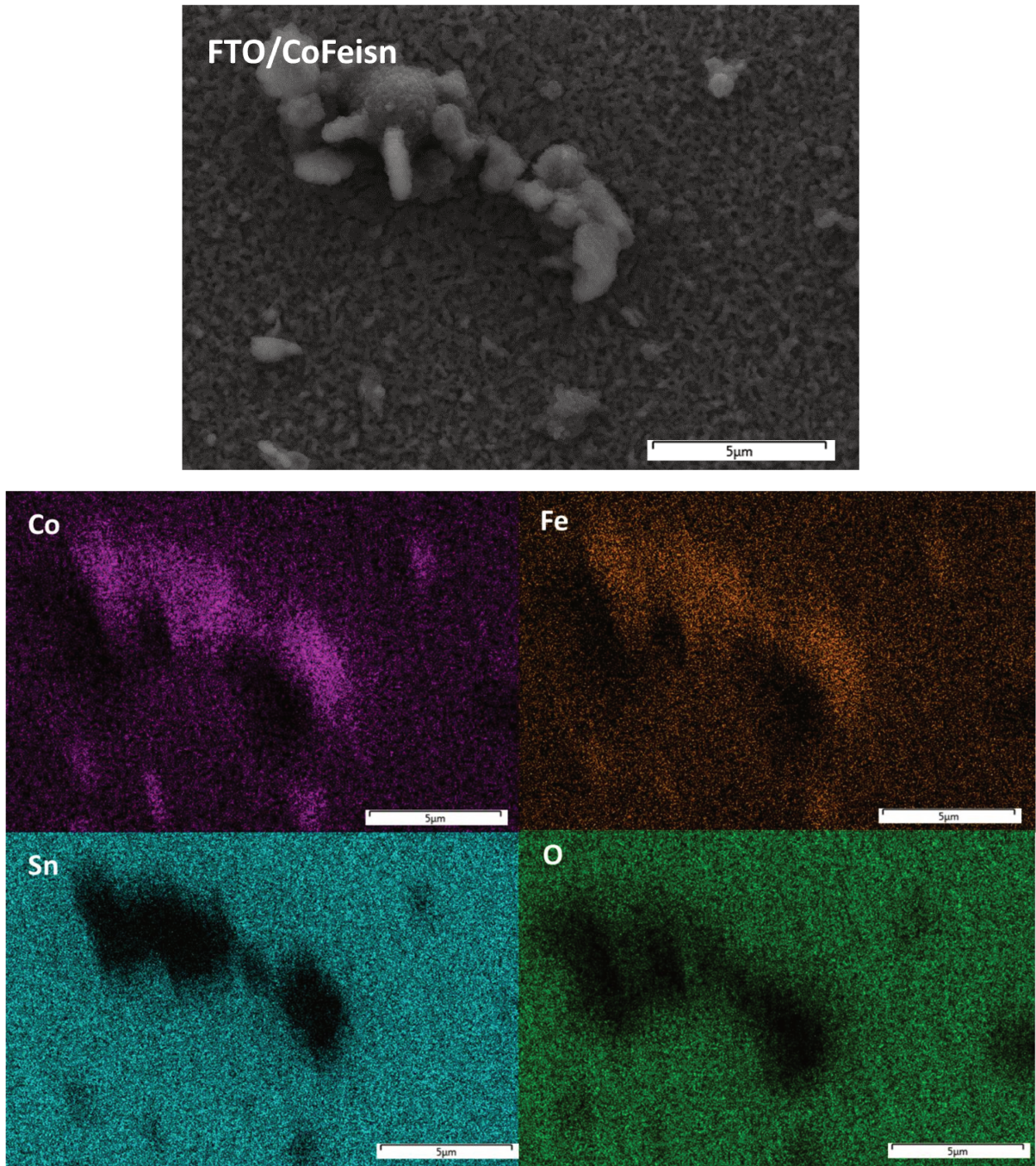


**Figure 43.** SEM micrographs and EDS analysis of FTO/CoFeisn electrode

Before their use, the substrates presented organized and localized structures distributed through the surface of the FTO layer (Figure 44). After the electrocatalysis, the structures present on the electrodes were partially removed, indicating that some loss in the activity of the material can be attributed to the leaching of the catalysts from the substrate surface.

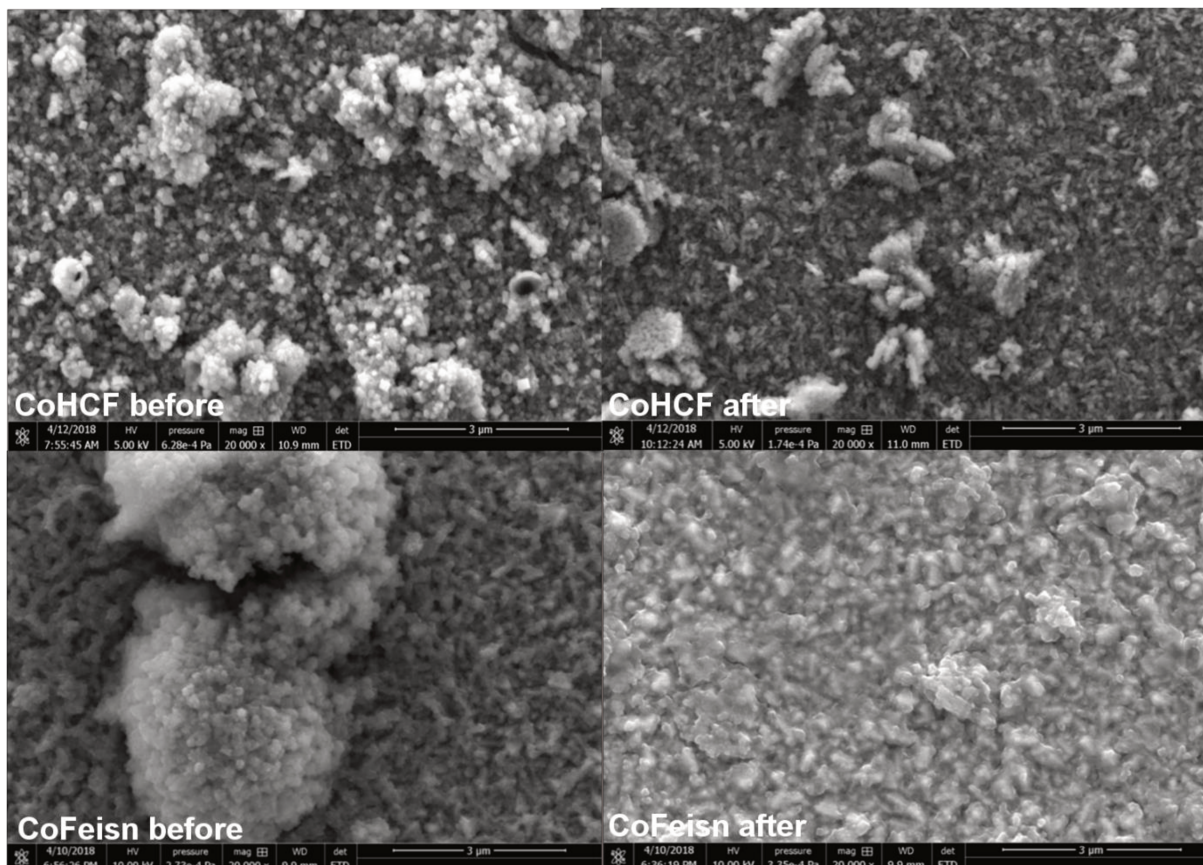


**Figure 44.** Micrographs of the substrates used in the electrocatalytic experiments. The substrates FTO/CoHCF and FTO/CoFeisn were evaluated before (A and C) and after the catalysis (B and D), respectively.

### 2.4.3 Oxygen production measurements

The results showed that the modified substrates were able to produce oxygen according to a  $4e^-$  Faradaic process, as shown in Figure 45A. The red line represents the theoretical oxygen production as obtained from the total charge that passed through the system during the chronopotentiometry experiment. The results indicate that the catalytic process was efficient and that no parallel reactions were occurring in the electrochemical cell. The small difference observed between the curves may be explained by experimental factors during the measurement, such as adsorption of oxygen molecules on the surface of the working electrode that can hinder the catalytic sites. The potential on the working electrode showed good stability at 1.2

V vs SCE during 1 hour of electrocatalysis (Figure 45B), indicating good stability of the catalyst under these conditions.

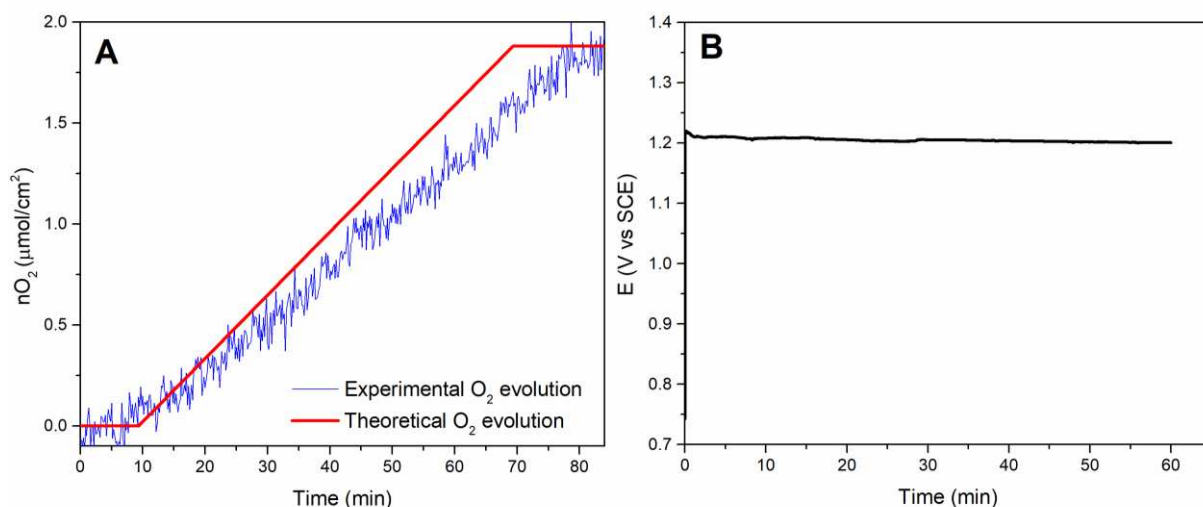


**Figure 45.** (A) Oxygen evolution and theoretical faradaic production at  $j = 0.2 \text{ mA/cm}^2$ . (B) Chronopotentiometry of FTO/CoFeisn with  $j = 0.2 \text{ mA.cm}^{-2}$  at PBS pH 7.1 containing  $1 \text{ mol.L}^{-1} \text{ KNO}_3$  as supporting electrolyte.

## 2.5 Conclusion

The coordination polymer produced showed interesting activity towards OER in a wide range of pH, including neutral conditions. The effect of the large surface area provided by the pentacyanidoferrate precursors was also observed in the activity of the coordination polymers when applied to water oxidation. The Tafel analysis showed that the material has a higher catalytic current when compared to traditional cobalt hexacyanoferrate, even though the mechanism for the OER is similar for both if one considers the Tafel slopes obtained. The higher number of cobalt catalytic sites available, can also be explained by the structural defects created in the polymer network due to the presence of the organic moiety, which lowers the crystallinity of the material. The oxygen evolution studies also showed that the catalytic current was a result of the water oxidation, as the faradaic efficiency was comparable to the theoretical values. The mechanism of the OER for these materials is suggested to be very dependent on the electronic density of iron sites, which influences the catalytic active cobalt neighbor sites.

### **3. Pentacyanidoferrate-based coordination polymers applied to photoanodes for water oxidation reaction**

#### **3.1 Introduction**

##### **3.1.1 Solar energy**

Each year, approximately 36 000 TW of solar energy reach the Earth's crust. This means that only 1% of the crust on Earth needs to be covered with just 10%-efficient photoelectrochemical cells (PEC) to generate the equivalent of 36 TW per year, which is sufficient to supply world annual demand by the year 2050. Artificial photosynthesis is a promising technology not only to harvest solar energy but also as a means of storage, in producing energy-rich chemical fuels such as hydrogen or hydrocarbons via processes such as water splitting or CO<sub>2</sub> utilization<sup>[83]</sup>.

Among the various chemical fuels, hydrogen exhibits 3–4-fold higher mass energy density compared to gasoline and can be utilized either through direct combustion or in hydrogen fuel cells. Even though water splitting devices have recently been reported to operate with an STH (solar-to-hydrogen) efficiency of 30% through coupling a photovoltaic cell and an electrolyser, most research efforts are concentrated on the development of direct low-cost, highly stable water splitting materials for use in PEC cells. This is due to two major driving forces. Firstly, a low overpotential is needed to drive the PEC water splitting, resulting in a higher STH conversion efficiency. Secondly, PEC water splitting requires a much simpler and space-saving construction with fewer components (wires, electrodes, reactor, etc.); thus, the cost of the PV–electrolyser system is estimated to be at least US \$8 per kg but can be reduced to ca. US \$3 per kg by integrating both a light harvester and a water splitting photocatalyst in a single system (PEC cell). The US department of Energy has said that the price of hydrogen must reach US\$2–3 kg<sup>-1</sup> (including production, delivery and dispensing) before it can compete with gasoline for use in passenger vehicles<sup>[84]</sup>. New generations of devices that employ either direct photoreactors or spatially separated photovoltaic cells and electrolyzers may render solar hydrogen generation commercially viable, thus enabling a sustainable hydrogen economy.

Figure 46 illustrates the implementation of a sustainable solar water-splitting power plant for safe, clean and efficient hydrogen production and utilization. This vision involves the assistance of commercially available renewable energy sources such as wind, solar and tidal to assist in powering the plant and thus reducing operating costs. The facility could be implemented in any seashore or off-shore location where seawater can be pumped and filtered, including platforms, tankers and floating or fixed ports. This seawater would be injected into photocatalytic cells for the generation of hydrogen, which can then be transported to fuelling stations with limited environmental issues relating to the implementation of large-area power station<sup>[84]</sup>.

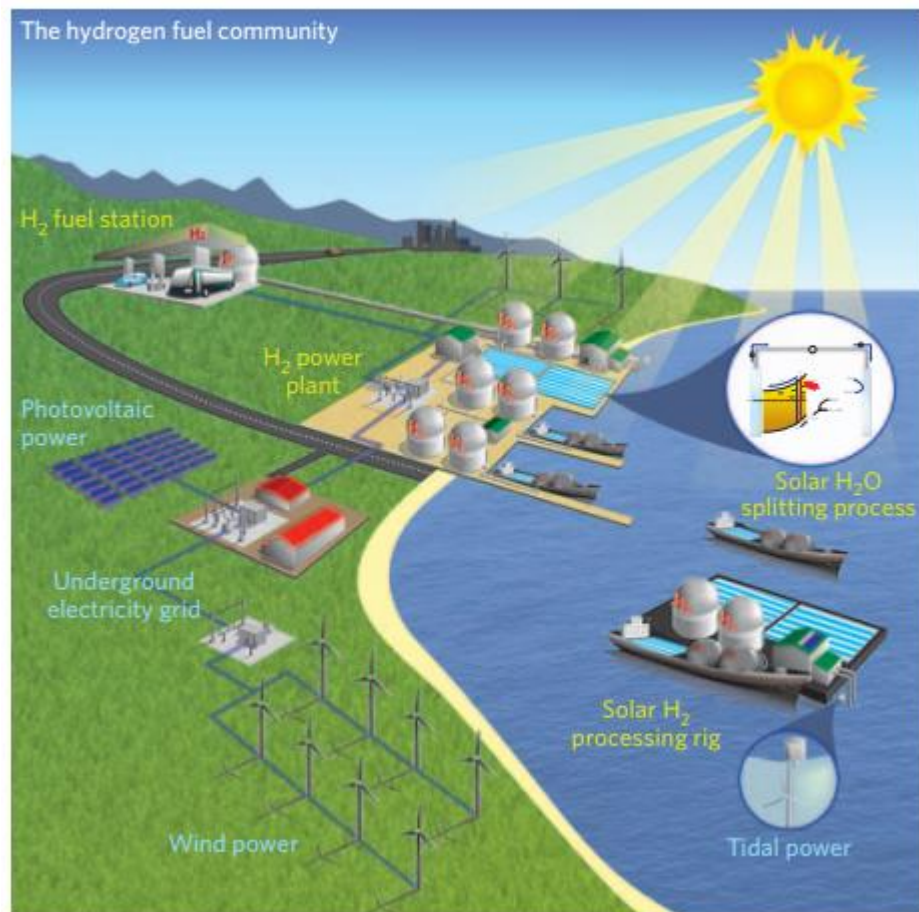


**Figure 46.** Sustainable hydrogen fuel community based on PEC systems<sup>[84]</sup>

Over the past few years, research efforts have resulted in the emergence of new generations of visible-light-active heterostructures that combine advances in

nanoscience such as confinements effects, innovative novel materials composition and low-cost fabrication techniques. All of these developments represent excellent candidates for efficient hydrogen generation, and some operate without any additives and/or at reduced or zero bias.

However, in order to be economically viable, the industrial production of hydrogen by solar water-splitting should deal with some challenges such as long-term stability in water and under concentrated illumination, toxicity to individuals and the environment, manufacturing costs and standardization. A further challenge is translating laboratory-scale academic research into scalable, manufacturable technologies, including considerations of packaging, large-area processing and outdoor testing<sup>[84]</sup>.

### **3.1.2 Photochemical water splitting**

The production of hydrogen using sunlight was first demonstrated in the advent of the oil crisis in 1972 by Fujishima and Honda<sup>[59]</sup>. They used TiO<sub>2</sub> with a band gap of 3.2 eV as the photoanode material, and their device was only sensitive to 0.5% of the solar spectrum and had little prospect to become a viable means for solar hydrogen production<sup>[85]</sup>.

In photocatalytic water splitting there is a largely positive change in the Gibbs free energy. Since this reaction is similar to the one that occurs in the photosynthetic system, it is also known as artificial photosynthesis<sup>[54]</sup>. A typical photocatalysis starts with the absorption of photons to form electron–hole pairs. Many heterogeneous photocatalysts have semiconductor properties.

When a photon with energy higher than the band gap reaches the semiconductor, electrons and holes are generated in the conduction and valence bands, respectively. This triggers the electrochemical reactions, where H<sup>+</sup> is reduced by electrons to produce H<sub>2</sub> and water molecules are oxidized by the holes to form O<sub>2</sub>. When using semiconductors for water splitting, one should take into consideration the width of the band gap and the energy of conduction and valence bands.

The bottom level of the conduction band (CB) must be more negative than the redox potential of  $\text{H}^+/\text{H}_2$  (0 V vs. NHE), while the top level of the valence band (VB) should be more positive than the redox potential of  $\text{O}_2/\text{H}_2\text{O}$  (1.23 V). Therefore, the theoretical minimum band gap for water splitting is 1.23 eV that corresponds to light of about 1100 nm<sup>[54][86]</sup>. However, the band structure is just a thermodynamic requirement but not a sufficient condition for a semiconductor to be used in this application, since redox properties of the material should be considered when developing a photocatalytic system. A general example of a PEC system, considering the energy levels of the photoanode and the cathode is presented in Figure 47.

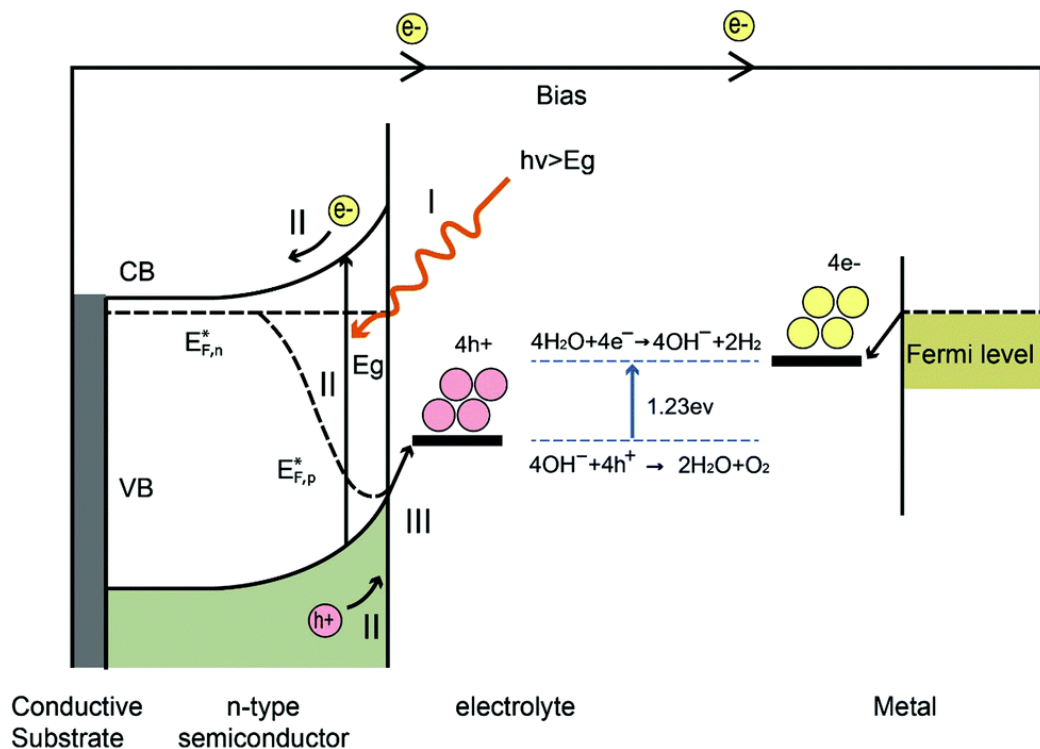


**Figure 47.** Representation of a PEC cell based on a n-type semiconductor and a metal counter electrode<sup>[83]</sup>.

The following steps of the photocatalysis is charge separation and migration of photogenerated carriers, where the crystallinity and particle size may affect the performance of the material. A large number of defects in the structure should increase the frequency of charge recombination, decreasing the catalytic activity. Smaller particles enables photocarriers to react fast due to increase in the surface area, so charge recombination is less frequent<sup>[54]</sup>. Thus, a good material to be used as a

photoanode should provide good charge separation and transport properties, besides being stable in aqueous environment<sup>[86]</sup>.

Finally, one should consider the effects that may affect the reactions that occur on the surface of the material, including reactive sites and available active area. Electrons and holes produced from incident light may recombine if active sites for redox reaction do not exist on the surface. Then, co-catalysts can be introduced to increase the number of sites for both hydrogen and oxygen evolution reactions. A general view of the necessary properties of a photocatalyst is presented in Figure 48.

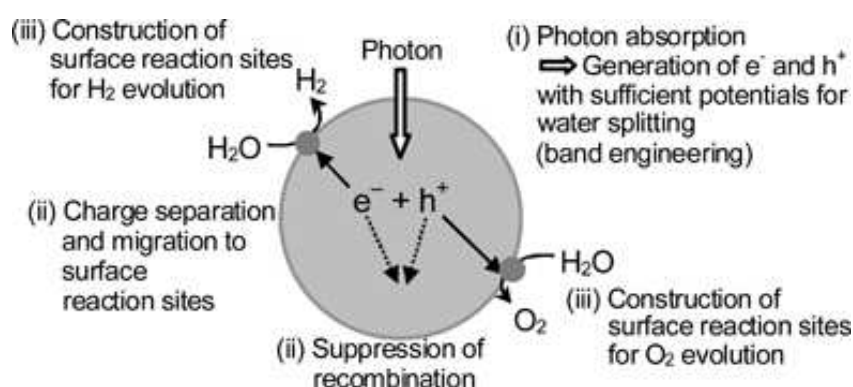


**Figure 48.** Main processes required for photocatalytic water splitting<sup>[54]</sup>.

### 3.1.3 Bismuth vanadate

The use of a  $\text{BiVO}_4$  photocatalyst for solar water oxidation was first reported by Kudo et al<sup>[87]</sup>. Monoclinic bismuth vanadate ( $\text{BiVO}_4$ ) is an interesting n-type semiconductor to be used in photoanodes for water splitting reaction. It has an indirect bandgap energy of approximately 2.4-2.5 eV (~500-520 nm band edge) with absorption into the visible and UV range of light and also a direct bandgap (ca. 2.7 eV).<sup>[88]</sup> Its very negative CB position may compensate for this disadvantage as not many n-type semiconductors that can utilize visible light have a CB edge position that is as negative as that of  $\text{BiVO}_4$ . Thus, it provides holes that can oxidize water on the valence band while the CB is close to the energy level of  $\text{H}_2$ .

Bismuth vanadate occurs naturally as the mineral pucherite but depending on the synthesis method in laboratory it adopts either the scheelite or zircon-type

structures (Figure 49). The photocatalytic properties are affected by the crystal structure, as there are a significant different in the bandgap energies of each system, which are 2.4 eV and 2.9 eV for scheelite and zircon-type respectively, as proposed by Kudo *et al.* In the first, the bandgap transition is due to the charge transfer transition from O 2p orbitals to empty V 3d. In the scheelite structure, the bandgap is reduced because the 6s state of  $\text{Bi}^{3+}$  appears above the O 2p and the transition from Bi 6s<sup>2</sup> (or hybrid Bi 6s<sup>2</sup>-O 2p orbitals) to the V 3d becomes possible (Figure 50)<sup>[86]</sup>.

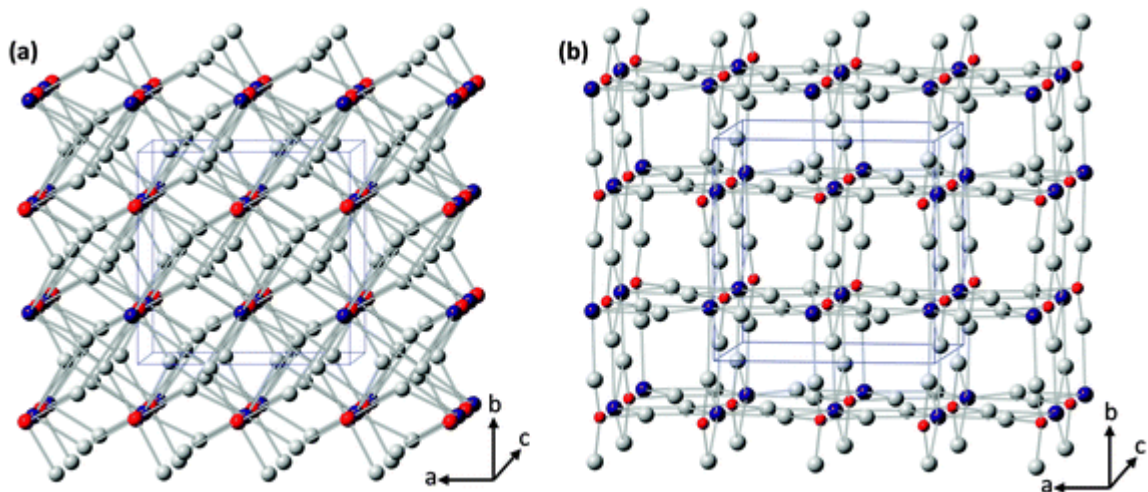


**Figure 49.** Possible crystal structures of bismuth vanadate prepared in laboratory. a) Tetragonal scheelite. b) Zircon-type structure. (Red: V; purple Bi; Gray: O)<sup>[86]</sup>.

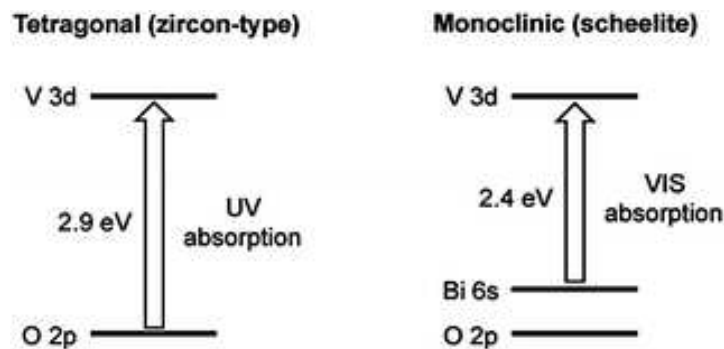


**Figure 50.** Band structure proposed for bismuth vanadate in different crystal systems<sup>[86]</sup>.

Recent studies have been focused on the application of  $\text{BiVO}_4$  as a photoanode for photoelectrochemical cells, despite of the excessive electron-hole recombination, poor charge transport and water oxidation kinetics that this material

provide. Its theoretical solar-to-hydrogen conversion efficiency ( $\eta_{\text{STH}}$ ) approaches 9.2% with maximum photocurrent of  $7.5 \text{ mA/cm}^2$  under standard AM 1.5 solar light irradiation<sup>[89]</sup> but because of the aforementioned phenomena the experimental efficiencies are lower than expected.

Many strategies have been developed in order to enhance the photocatalytic properties of  $\text{BiVO}_4$ , for example controlling the morphology of the particles. Increasing the porosity is an interesting way to increase surface area where the redox reactions occur and to reduce the electron-hole recombination since the distance needed for the charge carriers to react is lower. On the other hand, porosity can have effects on the number of surface states, defects sites and grain boundaries, which can lower the photocatalytic activity. Shape and exposed facets of the catalyst are other factors to be considered because they can affect the thermodynamic and kinetic factors of the photoanode reactions<sup>[89]</sup>. Thus, one should care about the exposed planes in order to maximize the efficiency of the photoreaction.

Another strategy that can be employed to enhance the photocatalytic performance of the photoanode is to create composite structures with an additional semiconductor or a conductor in order to improve charge carrier separation, photon absorption or charge transportation. Creating heterojunctions can promote fast electron injection from the CB of  $\text{BiVO}_4$  into the CB of another semiconductor, which is located at a more positive potential and reduce electron-hole recombination. In this sense, a very common semiconductor used is  $\text{WO}_3$ , due to its stability and position of the CB at  $+0.42 \text{ V}$  vs RHE, which enables easy electron injection. Good results were also obtained for heterojunctions produced with  $\text{BiVO}_4$  and  $\text{SnO}_2$  deposited on the surface of FTO (fluorine-doped tin oxide) substrate and also carbon materials.

The improvement of charge transfer in a FTO substrate is shown in Figure 51, and is also related to the distance travelled by the charge carriers to react after being produced by light incidence. In front-side illumination the electrons need to travel across the entire thickness of the to the  $\text{BiVO}_4/\text{FTO}$  interface. In back-side illumination holes need to travel across the entire thickness to the  $\text{BiVO}_4/\text{H}_2\text{O}$  interface in order to react. IPCE experiments showed that there is a higher efficiency of the photocatalysis when illumination occurs by the back-side which suggests that the electron mobility is slower than holes. Van der Krol *et. al* suggested that this effect is due to the low

interconnection of the vanadate tetrahedra, which does not allow electrons to move easily in the  $\text{BiVO}_4$  structure<sup>[90]</sup>.

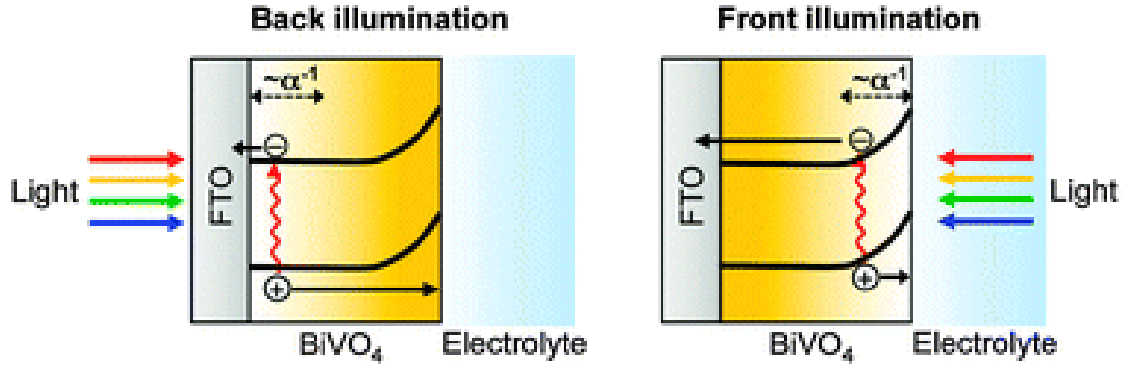


**Figure 51.** The influence of side illumination of FTO/ $\text{BiVO}_4$  modified substrates, indicating the difference of the distance that electrons and holes must travel<sup>[86]</sup>.

The catalytic activity of a material can be studied by comparing the photocurrent obtained in water oxidation with that produced in a hole acceptor solution, where the reaction occurs faster. In this situation it is assumed that all the holes produced participate in the redox reaction and no surface recombination occur. In this sense, it is possible to estimate the maximum charge transfer efficiency of a catalyst. The photocurrent density in aqueous solution is defined as:

$$j_{\text{H}_2\text{O}} = j_{\text{max}} \cdot \eta_{\text{abs}} \cdot \eta_{\text{CS}} \cdot \eta_{\text{CT}} \quad (\text{Eq. 40})$$

where with  $j_{\text{max}}$  is the maximum attainable photocurrent,  $\eta_{\text{abs}}$  the light absorption efficiency,  $\eta_{\text{CS}}$  the charge-separation efficiency of excited electron-hole pairs and  $\eta_{\text{CT}}$  the charge-transfer efficiency<sup>[82][91]</sup>. The light absorption is a semiconductor property that cannot be easily modified, but the last two parameters can be affected by modification with an OEC. In a hole acceptor solution, the charge transfer is maximum ( $\eta_{\text{CT}} = 1$ ) and the photocurrent can be described by:

$$j_{\text{HS}} = j_{\text{max}} \cdot \eta_{\text{abs}} \cdot \eta_{\text{CS}} \quad (\text{Eq. 41})$$

Thus, the  $\eta_{\text{CT}}$  in a solution is given by:

$$\eta_{CT} = \frac{j_{H_2O}}{j_{HS}} \text{ (Eq. 42)}$$

Studies using BiVO<sub>4</sub> in water oxidation in hole acceptor solutions showed that despite of the interesting electronic properties it has poor catalytic properties for water oxidation. An interesting way to improve the kinetics of water oxidation in this situation is to modify the surface of BiVO<sub>4</sub> with oxygen evolution catalysts (OECs). CoPi (cobalt phosphate) is a catalyst that was employed as a modifier of BiVO<sub>4</sub> and showed good results as it enhanced the magnitude of photocurrent, lowered the onset potentials, and increased the stability the photoanodes. This was explained by the reduction of surface recombination and increase in the effective hole consumption in water oxidation<sup>[86][92]</sup>.

### 3.1.4 Prussian blue and photocatalysis

Simultaneous detection of H<sub>2</sub> and O<sub>2</sub> during photolysis and the photo-oxidation of water were reported in two separate studies using Prussian blue and tris(2-2'-bipyridyl) ruthenium(II) complex as co-sensitizer<sup>[93]</sup>. Other authors report the co-photo-generation of H<sub>2</sub> and O<sub>2</sub> with visible light and Cu-HCF<sup>[69]</sup>.

An interesting approach was performed by Galán-Mascarós *et.al* by using cobalt hexacyanoferrate (CoHCF) as an oxygen evolution catalyst to modify a mesoporous BiVO<sub>4</sub> to obtain an efficient photoanode for water splitting, which increased the current densities obtained when compared to bare material, with considerable long-term stability. These materials have low absorption in the UV-vis region which also makes them very good candidates to be combined with chromophores for a photocatalytic process<sup>[82]</sup>. In this work, the authors used DFT calculations to create a model that explained the lowering of the onset potential of water oxidation, based on the good overlap between Co t<sub>2g</sub> and HOMO of water. The general result of the photocatalysis is presented in Figure 52.

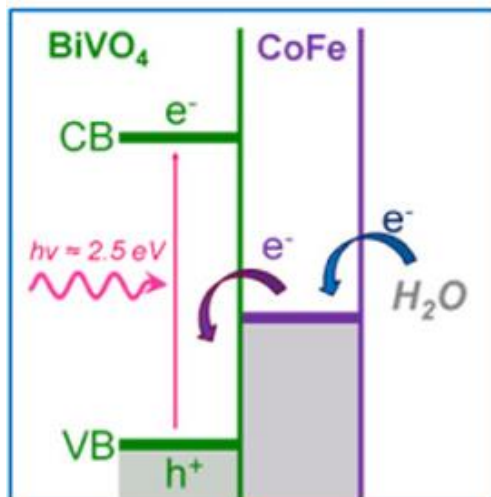


**Figure 52.** Simplified diagram of the photocatalytic process using an FTO/BiVO<sub>4</sub>/CoFe modified substrate<sup>[82]</sup>.

Fukuzumi *et al.* investigated the photocatalytic water oxidation performances of a series of Co-Pt PBAs in the presence of the well-defined [Ru(bpy)<sub>3</sub>]<sup>2+</sup>/S<sub>2</sub>O<sub>8</sub><sup>2-</sup> couple. A systematic study performed with [Co(CN)<sub>6</sub>]<sup>3-</sup> and [Pt(CN)<sub>6</sub>]<sup>4-</sup> groups in different stoichiometries clearly showed the number of active sites to be highly dependent on the number of defects<sup>[94]</sup>.

### 3.2 Motivation

The recent results obtained by a system composed by bismuth vanadate and cobalt hexacyanidoferrate provided a very efficient photoanode applied to water oxidation reaction. Thus, one can consider using the same strategy with the pentacyanidoferrates and evaluate how electronic structure and defects created using these precursors affect the activity of the whole system. In this study, the comparisons were performed taking into consideration the donor/acceptor character of the ligands and also their size, as shown in Figure 53.

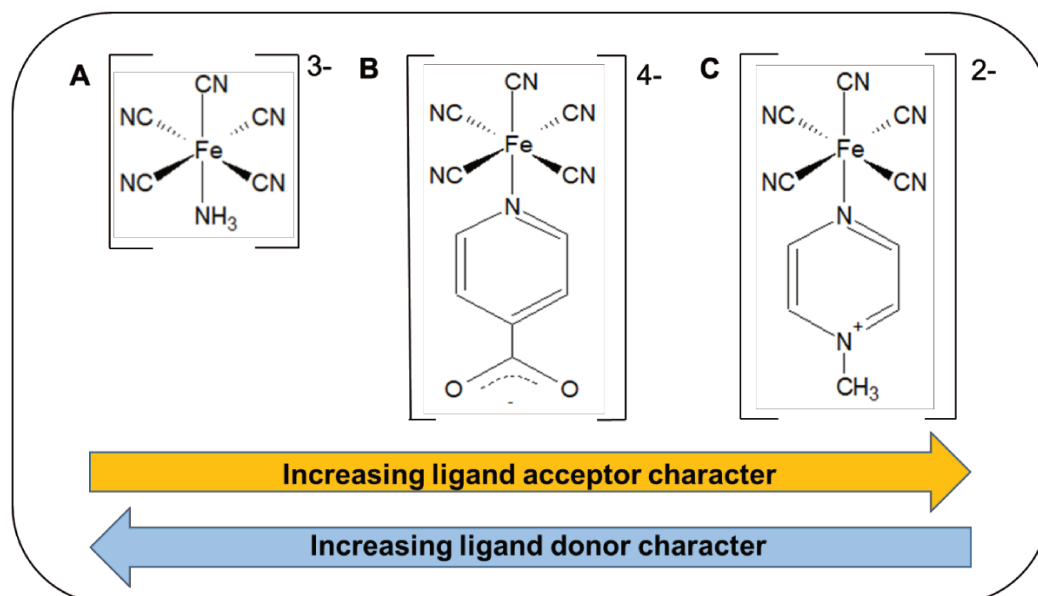


**Figure 53.** Structures of the pentacyanidoferrates used as precursors of ECPs. A)  $[\text{Fe}(\text{CN})_5\text{NH}_3]^{3-}$ , B)  $[\text{Fe}(\text{CN})_5(\text{isn})]^{4-}$ , C)  $[\text{Fe}(\text{CN})_5(\text{mpz})]^{2-}$ .

### 3.3 Experimental part

#### 3.3.1 Synthesis of pentacyanidoferrates precursors

**$\text{Na}_3[\text{Fe}(\text{CN})_5\text{NH}_3] \cdot 3\text{H}_2\text{O}$ . (CoFeNH<sub>3</sub>)** The complex was obtained as described in session 1.2.1.

**$\text{Na}_4[\text{Fe}(\text{CN})_5(\text{isn})] \cdot 5\text{H}_2\text{O}$  (isn = pyridine-4-carboxylate) (CoFeisn).** The complex was obtained as described in session 2.2.1.

**N-Methylpyrazinium Iodide (mpz-I)**<sup>[27]</sup>: Pyrazine (C<sub>4</sub>H<sub>4</sub>N<sub>2</sub>, 2.0 g) was dissolved in methyl iodide (10 mL), the color changing to light red. The solution was kept at room temperature, without stirring and in the dark for 1 week, turning into a yellow solid. This solid was filtered and recrystallized using ethanol (150 mL) at 60 °C. The solution was filtered while hot and cooled to room temperature. The product was crystallized in an ice bath, forming large yellow needles that were filtered again with

ice-cooled ethanol (15 mL). Yield: 75 %. Elemental analysis calculated for  $C_5H_7N_2I$ : C 27.05, H 3.18, N 12.62; Found C 27.00, H 3.27, N 12.60.

**$Na_2[Fe(CN)_5(mpz)] \cdot 4H_2O$  (mpz = methylpyrazinium)  $CoFempz$** <sup>[27]</sup>

Amminepentacyanidoferrate (0.2 g) was dissolved in water (1 mL) and then mixed with a solution of the ligand (1 mL) in five-fold excess. The solution was cooled in an ice bath for 30 min in the absence of light and whilst stirring. The solution was treated with NaI (1.0 g) and, after complete dissolution, ethanol (30 mL) was added slowly, under intense stirring, until complete precipitation of the complex. The solid was filtered by using a vacuum pump, washed with ethanol, dissolved again in a solution of the ligand in two-fold excess, treated with further NaI (1.0 g), filtered, and stored in a desiccator. A constant weight was obtained after 1 week of drying. The complex is very hygroscopic. Yield: 86 %. Elemental analysis calculated for  $C_{10}H_{15}FeN_7Na_2O_4$ : C 30.09, H 3.79, N 24.57; Found C 29.97, H 3.90, N 23.81.

### 3.3.2 Preparation of FTO/ $BiVO_4$ substrates

Before modification, FTO substrates of 1 x 2.5 cm were cleaned by immersion in a soap solution and sonication for 10 minutes. After that, the substrates were rinsed with milliQ water to remove any residual material. The procedure was repeated using isopropanol and milliQ water as cleaning solvents. Then the substrates were transferred to an oven at 400 °C for 30 minutes for annealing.

The electroactive surface areas of the substrates were limited to a 1.5 cm<sup>2</sup> area using a tape. Bismuth vanadate was deposited on the surface of FTO substrate in three steps. Bio-Logic VMP3 multichannel potentiostat/Galvanostat was used in this step. First, a metallic film of bismuth was electrodeposited using a solution of 20mM  $Bi(NO_3)_3$  in ethylene glycol by passing a 0.06 C.cm<sup>-2</sup> charge at -1.8 V vs Ag/AgCl, followed by a rest time of 2s eight times. A black film was observed after the procedure was completed. After that, the electrodes were rinsed carefully with ethanol.

The conversion to bismute vanadate was made by adding 90 μL of a  $VO(acac)_2$  solution in DMSO on the surface of the modified substrates and heating at

80 °C on a plate in order to remove the solvent. After that the substrates were transferred to an oven at 500 °C for 2h (2°C/min) and a yellow film was observed. Finally, after cooling to room temperature, the substrates were immersed in a 1.0 mol.L<sup>-1</sup> NaOH solution for 30 minutes under stirring.

### **3.3.3 Deposition of cobalt cyanidoferrates on FTO/BiVO<sub>4</sub>**

In this step the four different cyanidoferrate precursors were used in order to obtain Prussian blue-like structures on the surface of bismuth vanadate (HCF, PCF-NH<sub>3</sub>, PCF-isn and PCF-mpz). The deposition was performed by dipping cycles. The FTO/BiVO<sub>4</sub> substrates were first immersed in a 5.0 x 10<sup>-3</sup> mol.L<sup>-1</sup> aqueous solution of CoCl<sub>2</sub> for 10 minutes under stirring, followed by dipping in a 5.0 x 10<sup>-3</sup> mol.L<sup>-1</sup> aqueous solution of one of the cyanidoferrates precursors, under stirring. A total number of six dipping cycles was performed for each substrate.

### **3.3.4 SEM microscopy**

The morphology of the modified substrates was evaluated using a JEOL JSM-6400 scanning electron microscope operating at 20 kV.

### **3.3.5 Photoelectrochemical studies**

The electrochemical cell was obtained by using the modified FTO substrates as working electrodes, Ag/AgCl (3 mol.L<sup>-1</sup>) as reference electrode and a platinum mesh as counter electrode. Geometrical areas of the FTO substrates were calculated using ImageJ software and the value was used to normalize the current

values obtained in the experiments, which were described as current densities values ( $j$ ) in  $\text{mA}\cdot\text{cm}^{-2}$ . Most of the experiments were conducted in a  $0.1 \text{ mol}\cdot\text{L}^{-1}$  phosphate buffer solution (PBS) pH 7.1. Also, some experiments were performed in a hole scavenger solution prepared by adding  $1 \text{ mol}\cdot\text{L}^{-1}$   $\text{Na}_2\text{SO}_3$  to the PBS solution aforementioned. Cyclic voltammetry experiments were performed at  $50 \text{ mV}\cdot\text{s}^{-1}$  scan rate. Linear scan voltammetry was performed at  $1 \text{ mV}\cdot\text{s}^{-1}$ . Chronoamperometry studies were performed by applying  $0.61 \text{ V}$  vs Ag/AgCl for several hours. The electrochemical setup was coupled to a  $450 \text{ W}$  Xe lamp in order to obtain a  $100 \text{ mW}\cdot\text{cm}^{-2}$  (1 sun) illumination. Experiments using chopped light were performed using a shutter. The substrates were irradiated on the FTO side of the substrates, since conduction in  $\text{BiVO}_4$  is well-known to be limited by its small electron diffusion length<sup>[82]</sup>.

## 3.4 Results and Discussion

### 3.4.1 SEM microscopy

The electrodeposition of bismuth vanadate allows the large deposition of the Prussian blue analogs inside its structure. The use of mild deposition conditions, such as ambient temperature, neutral solutions for the coordination polymer layer also avoids the production of cobalt oxide/hydroxide derivatives and modifications on the structure of both bismuth vanadate and fluorine tin oxide during the preparation step. The number of dipping steps used was based on previous studies<sup>[82]</sup> and it was confirmed that considerable photocurrents can be reached from this methodology. The SEM micrographs (Figure 54) show that  $\text{BiVO}_4$  deposited on the FTO shown spread agglomerates over the surface, indicating that the film was not completely spread on the substrate. This behavior was also observed in the electrodeposition of the Prussian blue analogs as described in previous studies<sup>[32]</sup>. From the micrographs it is possible to observe that the concentration of  $\text{CoFeNH}_3$  was considerably higher than the other Prussian blue analogs. EDX spectra of the samples did not show differences between

bare and modified  $\text{BiVO}_4$  which may be due to the thin layer of the PBAs obtained using this method.

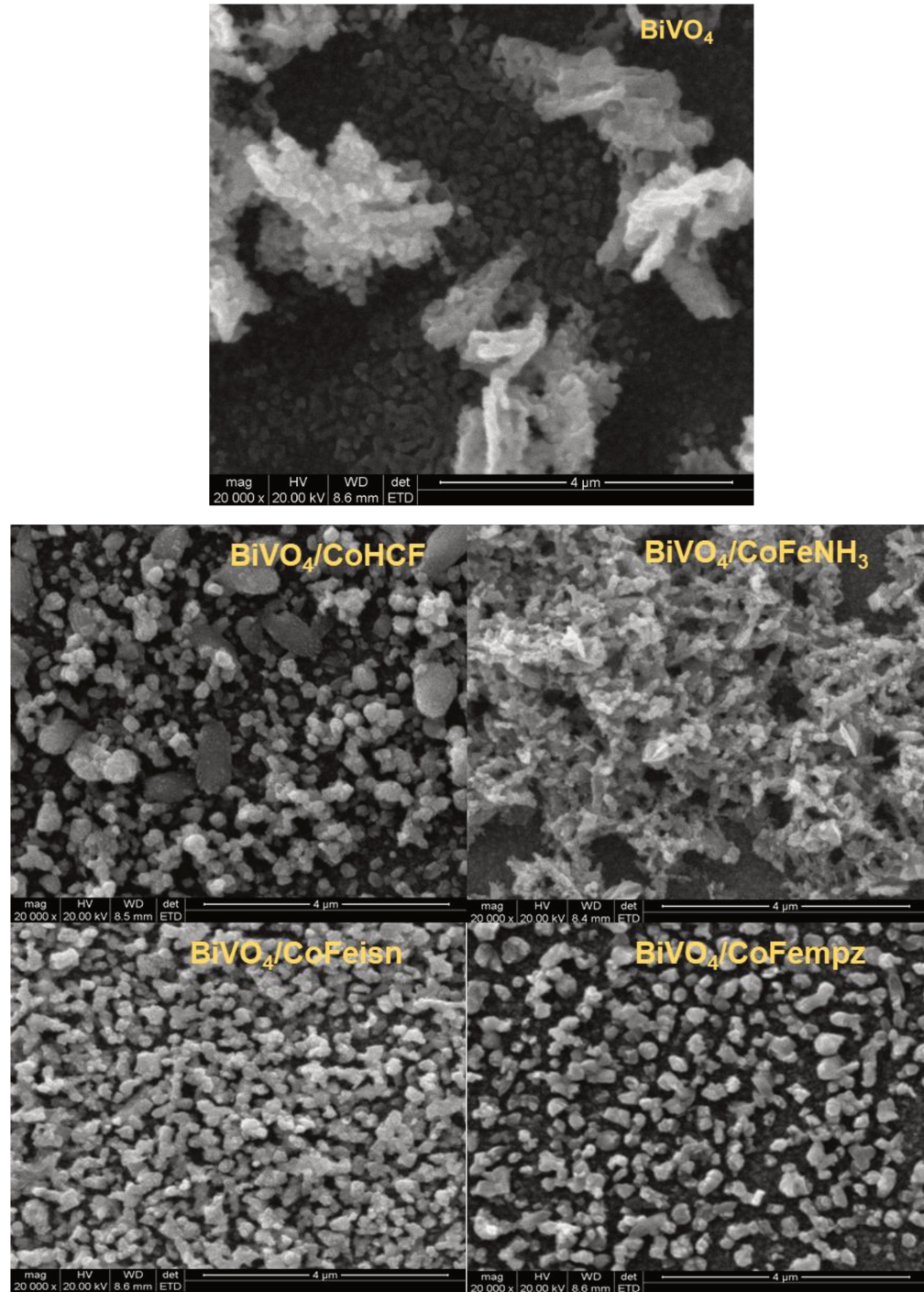


**Figure 54.** SEM microscopies of FTO/ $\text{BiVO}_4$  substrates modified with different cyanidoferrate coordination polymers at 20000 X magnification.

### 3.4.2 Photoelectrochemical studies

Cyclic voltammograms of the photoanodes were obtained under 1 sun illumination and in the dark. The stability of the modified substrates was evaluated by 5-10 cyclic voltammograms under illumination until a stable profile was observed. This procedure was necessary since not all the substrates were eligible for the catalytic studies and benchmarking due to the heterogeneous nature of FTO substrates and the corresponding bismuth vanadate layer. The results are presented in Figure 55 and show that all the catalysts increased the observed photocurrent when compared with the bare bismuth vanadate. The higher catalytic current was observed for the CoFeNH<sub>3</sub> coordination polymer, reaching current densities higher than 2.0 mA.cm<sup>-2</sup> above 1.6 V vs RHE. Furthermore, there is a large shift of the onset potential to cathodic values when compared with the bare BiVO<sub>4</sub> modified substrate, as shown in Table 7. The coordination polymers CoFeNH<sub>3</sub> and CoFeisn showed the higher shifts, which indicates that in these materials the electron-hole separation is more efficient<sup>[92]</sup>.

CoFeNH<sub>3</sub> interestingly showed a considerable redox activity in the dark, as a quasi-reversible redox pair is observed with  $E^0 = 1.1$  V vs RHE. These results suggest that the material has the highest electroactive surface area of the series, which is very desirable when it comes to the enhancement of catalytic activity of Prussian blue analogs. These results can be explained also by considering the electronic nature of the ligand NH<sub>3</sub>. In this series, it is the most donor ligand, which means that it provides more electrons to the polymer structure than the N-heterocyclic ligands such as isonicotinate or N-methylpyrazinium. Thus, it enables more electrons to react with holes produced in the VB of bismuth vanadate, increasing the efficiency of the whole system. On the other hand, the smaller increase in the catalytic current was observed with the CoFempz catalyst, which is the most acceptor ligand of the series. A comparison between cyclic voltammograms of the photoanodes under illumination is also presented in Figure 56.

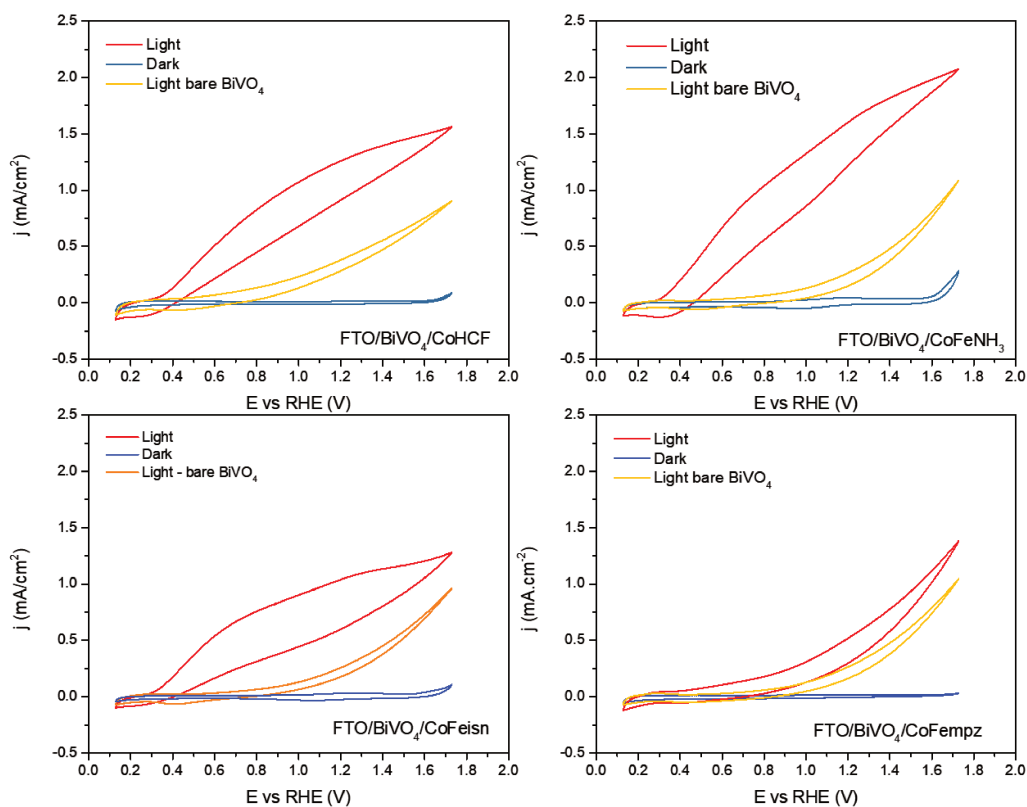


**Figure 55.** Cyclic voltammograms of FTO/BiVO<sub>4</sub> substrates in the dark and under illumination (1 sun), in PBS pH 7.1. Scan rate 50 mV.s<sup>-1</sup>.

**Table 7.** Comparison between onset potentials for  $j = 0.1 \text{ mA.cm}^{-2}$  of the different photoanodes obtained by cyclic voltammetry in PBS 7.1, scan rate 50 mV.s<sup>-1</sup>. Potentials are given in V vs RHE.

Sample	Modified substrate	Bare BiVO <sub>4</sub>	$\Delta E$
FTO/CoHCF	0.38	0.71	0.33
FTO/CoFeNH <sub>3</sub>	0.35	0.93	0.58
FTO/CoFeisn	0.36	0.93	0.57
FTO/CoFempz	0.57	0.94	0.37

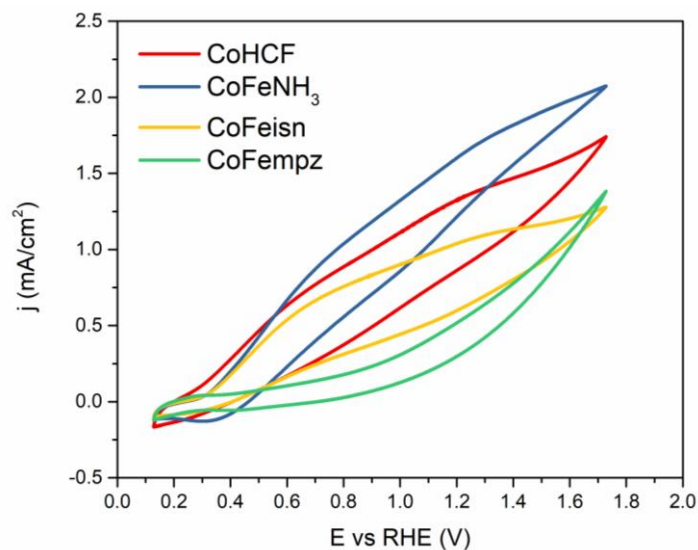


**Figure 56.** Cyclic voltammety under illumination (1 sun) of the FTO substrates modified with  $\text{BiVO}_4$  and Prussian blue analogs obtained using different cyanidoferrate precursors. Scan rate  $50 \text{ mV}\cdot\text{s}^{-1}$  in PBS buffer  $\text{pH} = 7.1$ .

Linear scanning voltammetry was performed in low scanning rate in order to obtain quasi steady state situation (Figure 57). The experiments were performed at  $1 \text{ mV}\cdot\text{s}^{-1}$  and the onset potential was chosen as the necessary applied voltage to reach  $j = 0.1$  or  $0.3 \text{ mA}\cdot\text{cm}^{-2}$  for each of the substrates (Table 8). Except by CoFempz, all the catalysts showed a typical catalytic behavior of  $\text{BiVO}_4$  photoanodes, specially at lower potential values. However, the highest current densities were also observed for the CoFeNH<sub>3</sub> catalyst.

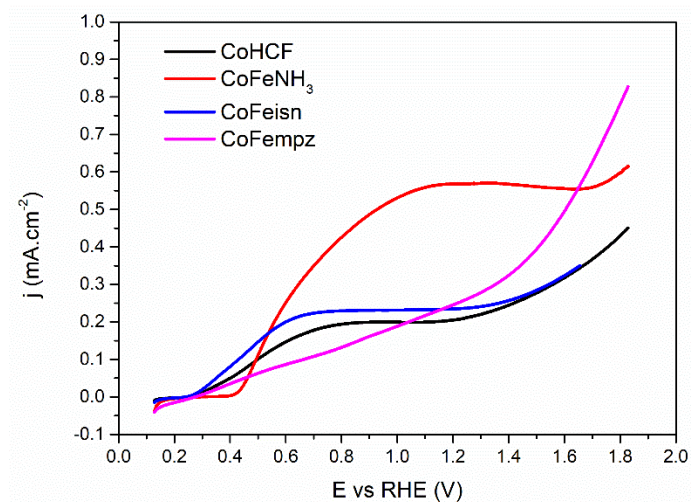


**Figure 57.** LSV of the modified FTO substrates under illumination. Scan rate  $1 \text{ mV}\cdot\text{s}^{-1}$ .

**Table 8.** Onset potentials obtained from the linear scanning voltammetries.

<b>Substrate</b>	<b>Onset Potential (V vs RHE) j= 0.1 mA.cm<sup>-2</sup></b>	<b>Onset Potential (V vs RHE) j= 0.3 mA.cm<sup>-2</sup></b>
FTO/CoHCF	0.50	1.57
FTO/CoFeNH <sub>3</sub>	0.49	0.65
FTO/CoFeisn	0.43	1.57
FTO/CoFempz	0.66	1.36

The photoanodes were also studied under a chopped light, and the results are presented in Figure 58. In this situation the higher current densities were observed for CoFeNH<sub>3</sub> and CoFeisn. After each illumination step it is possible to observe a faster exponential decay of the anodic current, which is attributed to fast charge recombination. An interesting effect observed in all the photoanodes and more pronounced in CoFeNH<sub>3</sub> is the cathodic current produced in the dark which is attributed to the reduction of cobalt by the electrons in the BiVO<sub>4</sub> conduction band<sup>[82][92]</sup>.

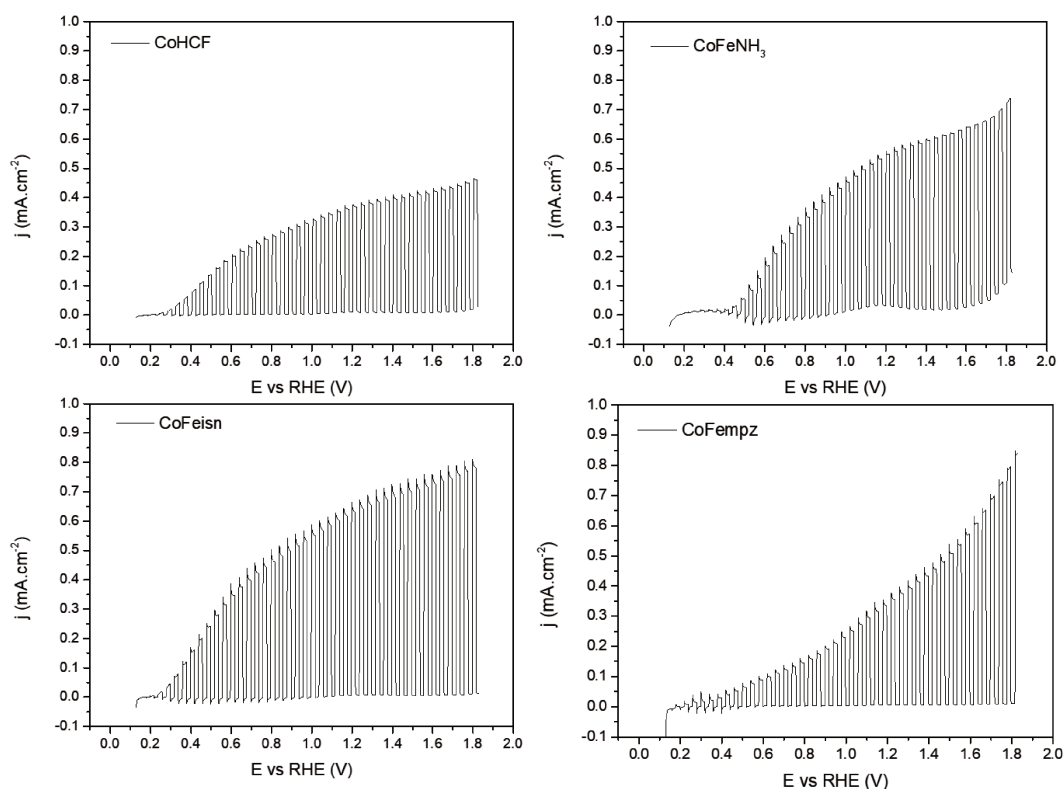


**Figure 58.** Linear sweep voltammetry of modified FTO substrates under chopped light ( $T = 2s$ ). Scan rate  $10 \text{ mV}\cdot\text{s}^{-1}$  in PBS  $\text{pH} = 7.1$ .

### 3.4.3 Photoelectrochemistry in hole scavenger solution

The performance of the photoanodes were also evaluated in a hole scavenger solution, where no electron-hole recombination occurs in the semiconductor/liquid interface. Previous studies showed that the photocatalytic behavior of bare  $\text{BiVO}_4$  can be enhanced in these conditions, which also reflects the low efficiency of this material when applied to of water oxidation. The effect of the hole scavenger was demonstrated for all the different substrates, with a considerable increase of the current densities, as shown in Figure 59. An analysis of the charge transfer efficiency showed that, except by the CoFempz, all the cyanidoferrates provided  $\eta$  values higher than 50% (Figure 60), which shows that all the coordination polymers enhanced the poor kinetics of bismuth vanadate. These values are also very close to the reported in the literature, which is around 80%<sup>[82]</sup>. CoHCF showed the highest value for charge transfer efficiency, indicating that the absence of defects may

influence this property of the materials. The values of charge transfer efficiency and the optimum potentials are presented in Table 9.

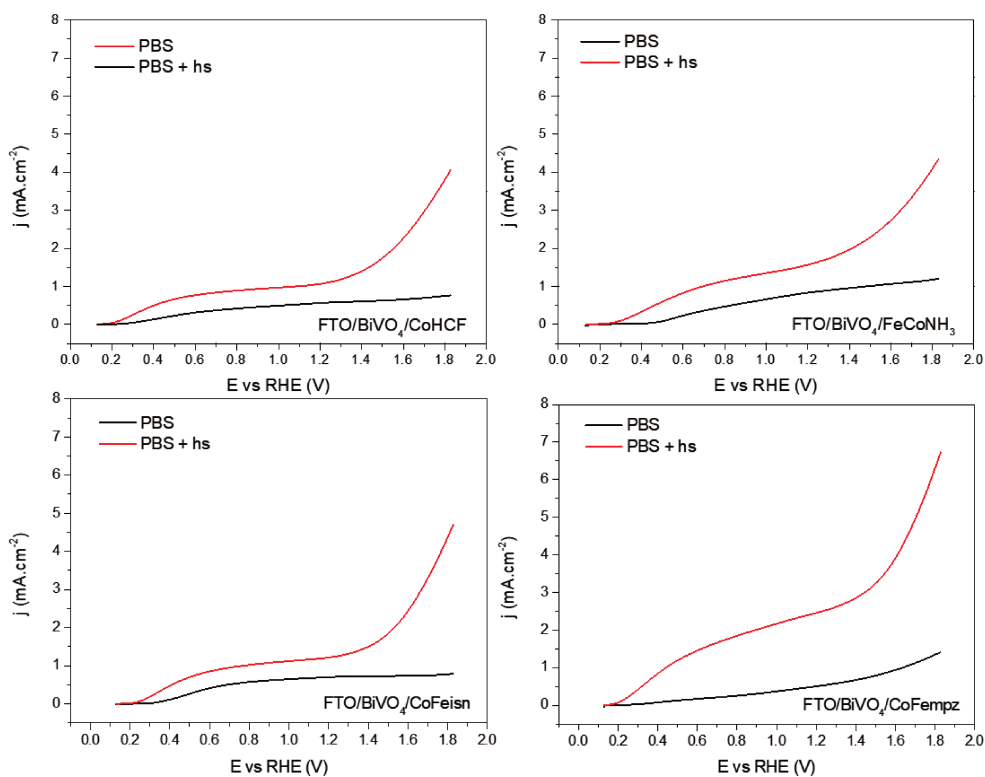


**Figure 59.** Linear sweep voltammeteries of modified substrates in PBS solution and in the presence of a hole scavenger  $\text{Na}_2\text{SO}_3$   $1 \text{ mol.L}^{-1}$ . Scan rate  $10 \text{ mV.s}^{-1}$ .

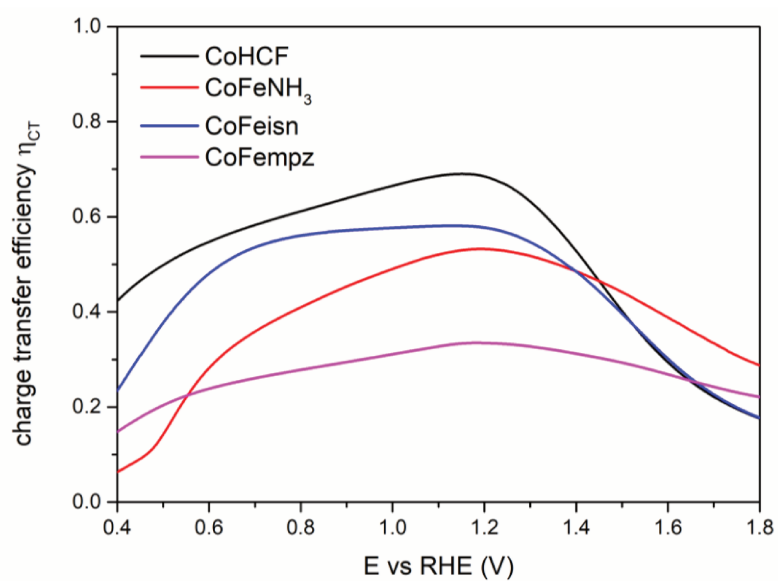


**Figure 60.** Calculated charge transfer efficiency for the different substrates.

**Table 9.** Optimum potentials and maximum charge transfer efficiency obtained for the different photoanodes.

FTO Electrode	Optimum potential (V vs RHE)	$\eta$ (charge transfer efficiency)
CoHCF	1.16	0.69
CoFeNH <sub>3</sub>	1.20	0.53
CoFeisn	1.12	0.58
CoFempz	1.18	0.33

#### 3.4.4 Long term stability

The stability and the activity of the photoanodes under irradiation was studied through a long-term electrolysis at 1.23 V vs RHE. The results in Figure 61 showed that the bare BiVO<sub>4</sub> produced the lower photocurrent after 15 hours of electrolysis. All the substrates containing the cyanidoferrates increased considerably the photocatalytic current. Both electrodes modified with CoHCF and CoFeisn showed a high anodic current that reached a stable value after the first hours of the experiment. Since the profiles are similar between all the substrates, it is possible to assume that the loss of activity may be due to some deactivation of FTO or BiVO<sub>4</sub> layers<sup>[82]</sup>. However, the most interesting profile was obtained by the CoFeNH<sub>3</sub> modified substrate, which showed the highest current densities and good stability after almost 16 hours of electrolysis. In all the chronoamperometric studies it was possible to observe spikes of current, that may be attributed to some surface phenomena such as oxygen bubbles adsorption on the electrode.

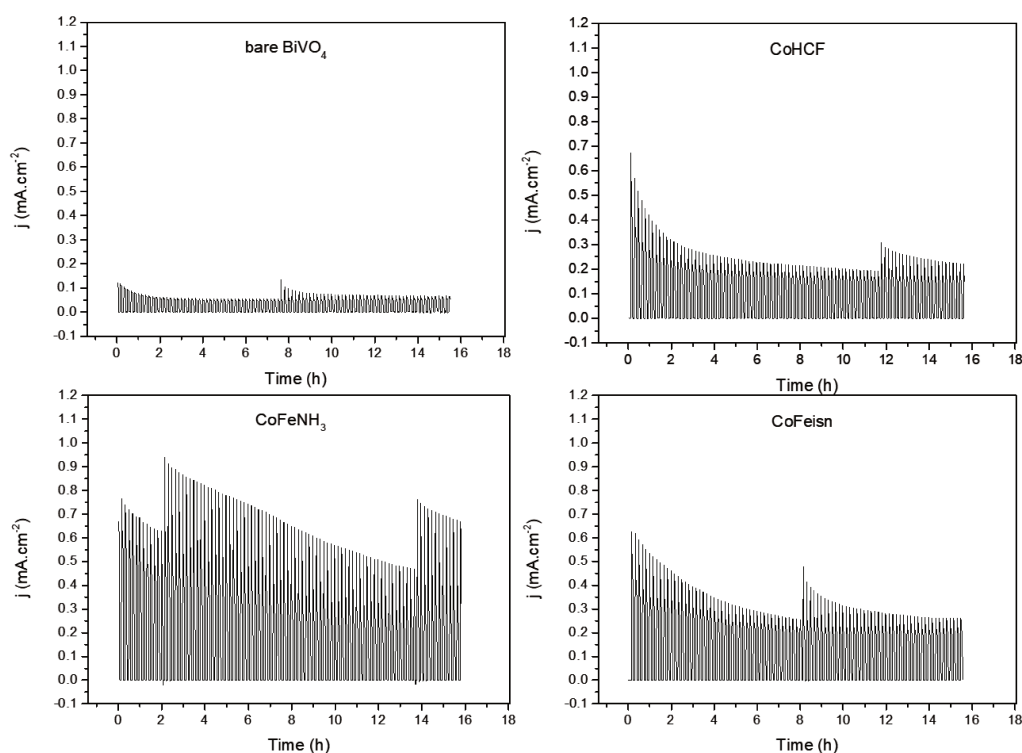


**Figure 61.** Chronoamperometry of the photoanodes at 1.23 V vs RHE under illumination during several hours.

### 3.5 Conclusion

The photoanodes obtained using the pentacyanidoferrate precursors improved the photocatalytic activity of bismuth vanadate by increasing the produced photocurrent and the charge transfer efficiency. This was explained both by an increment in the surface area of the catalyst due to the presence of different organic moieties in the polymer structure and by electronic effects of these molecules. It was shown that higher catalytic currents were obtained by the polymer containing the most donor ligand in its structure, which is  $\text{CoFeNH}_3$ . The PB analog produced using the pentacyanidoferrate precursor containing the most acceptor ligand showed the lower catalytic activity and indicates that electronic density on the iron atoms can affect drastically the activity of the materials.

## 4. General Conclusions and perspectives

The electrochemical and structural properties of Prussian blue and its analogs make this class of materials very versatile, with applications in sensors, electrocatalysis and photochemical setups. However, when one prepares Prussian blue analogs using different precursors such as pentacyanidoferrates, these properties are slightly modified, which can be attributed to the influence of different ligands.

The effects of the ligands cannot be attributed mostly to a single factor. This is because the polymeric network of Prussian blue analogs is a complex structure that can be affected by many features. However, it is clear that pentacyanidoferrate introduces several structural defects in the framework and this may cause an enhancement of the surface active area, as denoted by the results of oxygen reduction and water oxidation. On the other hand, by increasing the number and size of the defects, there may be a lowering in the mechanical resistance of the films, which make them less resistant to the catalytic conditions. Thus, it is necessary to balance these properties in order to reach a stable and efficient catalyst.

Considering the electronic influence of the ligands, the results showed that they can be fundamental in understanding the electrochemistry of the corresponding coordination polymers. When compared to traditional cyanide, isonicotinate which is an acceptor ligand improved the current density obtained for the coordination polymer. However, in the photocatalytic oxidation of water, the most donor ligand ( $\text{NH}_3$ ) provided the best performance. Therefore, according to the application there will be a most appropriate precursor.

There are still many studies that could provide more information about the Prussian blue obtained from the pentacyanidoferrates. *In operando* techniques including vibrational and x-ray spectroscopies would certainly give information about the structure and redox states of the metallic sites in each situation. DFT calculations could also give valuable information about electronic structure of the precursors and the polymers.

In summary, the pentacyanidoferrates showed interesting properties as precursors of electroactive coordination polymers that should be explored in a near future. Understanding the influence of different ligands in the final structure of the

material can enable one to modulate their activities according to the desired application.

## 5. References

- [1] M. B. Zakaria, T. Chikyow, *Coord. Chem. Rev.* **2017**, *352*, 328–345.
- [2] S. Kitagawa, R. Matsuda, *Coord. Chem. Rev.* **2007**, *251*, 2490–2509.
- [3] S. Kitagawa, R. Kitaura, S. Noro, *Angew. Chemie Int. Ed.* **2004**, *43*, 2334–2375.
- [4] K. Ariga, V. Malgras, Q. Ji, M. B. Zakaria, Y. Yamauchi, *Coord. Chem. Rev.* **2016**, *320–321*, 139–152.
- [5] H. J. Buser, A. Ludi, W. Petter, D. Schwarzenbach, *J. Chem. Soc. Chem. Commun.* **1972**, 1299.
- [6] H. J. Buser, D. Schwarzenbach, W. Petter, A. Ludi, *Inorg. Chem.* **1977**, *16*, 2704–2710.
- [7] M. Ware, *J. Chem. Educ.* **2008**, *85*, 612.
- [8] F. S. Hegner, J. R. Galán-Mascarós, N. López, *Inorg. Chem.* **2016**, *55*, 12851–12862.
- [9] A. A. A. Karyakin, O. V. Gitelmacher, E. E. Karyakina, *Anal. Chem.* **1995**, *67*, 2419–2423.
- [10] D. Moscone, D. D'Ottavi, D. Compagnone, G. Palleschi, A. Amine, *Anal. Chem.* **2001**, *73*, 2529–2535.
- [11] N. A. Sitnikova, M. A. Komkova, I. V. Khomyakova, E. E. Karyakina, A. A. Karyakin, *Anal. Chem.* **2014**, *86*, 4131–4134.
- [12] Z. Chu, Y. Liu, W. Jin, *Biosens. Bioelectron.* **2017**, *96*, 17–25.
- [13] D. Jiang, Z. Chu, J. Peng, W. Jin, *Sensors Actuators B Chem.* **2016**, *228*, 679–687.
- [14] A. A. Karyakin, *Electroanalysis* **2001**, *13*, 813–819.
- [15] F. Ricci, G. Palleschi, *Biosens. Bioelectron.* **2005**, *21*, 389–407.
- [16] K. Itaya, N. Shoji, I. Uchida, *J. Am. Chem. Soc.* **1984**, *106*, 3423–3429.

- [17] N. Ghasdian, Y. Liu, R. McHale, J. He, Y. Miao, X. Wang, *J. Inorg. Organomet. Polym. Mater.* **2013**, *23*, 111–118.
- [18] F. M. Matsumoto, M. L. A. Temperini, H. E. Toma, *Electrochim. Acta* **1994**, *39*, 385–391.
- [19] S. H. Toma, J. A. Bonacin, K. Araki, H. E. Toma, *Eur. J. Inorg. Chem.* **2007**, *2007*, 3356–3364.
- [20] A. L. B. Formiga, S. Vancoillie, K. Pierloot, *Inorg. Chem.* **2013**, *52*, 10653–63.
- [21] H. E. Toma, C. Creutz, *Inorg. Chem.* **1977**, *16*, 545–550.
- [22] H. E. Toma, J. M. Malin, *Inorg. Chem.* **1973**, *12*, 2080–2083.
- [23] H. E. Toma, J. M. Malin, *Inorg. Chem.* **1973**, *12*, 1039–1045.
- [24] C. C. Corrêa, S. A. V. Jannuzzi, M. Santhiago, R. A. Timm, A. L. B. Formiga, L. T. Kubota, *Electrochim. Acta* **2013**, *113*, 332–339.
- [25] C.-H. Nieh, S. Tsujimura, O. Shirai, K. Kano, *Anal. Chim. Acta* **2013**, *767*, 128–33.
- [26] B. M. Pires, S. A. V. Jannuzzi, A. L. B. Formiga, J. A. Bonacin, *Eur. J. Inorg. Chem.* **2014**, *2014*, 5812–N5819.
- [27] M. C. Monteiro, K. C. F. Toledo, B. M. Pires, R. Wick, J. A. Bonacin, *Eur. J. Inorg. Chem.* **2017**, *2017*, 1979–1988.
- [28] M. Shao, Q. Chang, J.-P. Dodelet, R. Chenitz, *Chem. Rev.* **2016**, *116*, 3594–3657.
- [29] L. Du, C. Du, G. Chen, F. Kong, G. Yin, Y. Wang, *ACS Appl. Mater. Interfaces* **2016**, *8*, 15250–15257.
- [30] Y. Jiao, Y. Zheng, M. Jaroniec, S. Z. Qiao, *Chem. Soc. Rev.* **2015**, *44*, 2060–2086.
- [31] W. E. Mustain, J. Prakash, *J. Power Sources* **2007**, *170*, 28–37.
- [32] B. M. Pires, F. E. Galdino, J. A. Bonacin, *Inorganica Chim. Acta* **2017**, *466*, 166–173.

- [33] G. Brauer, *Handbook of Preparative Inorganic Chemistry*, Academic Press, New York, **1963**.
- [34] H. T. S. Britton, R. A. Robinson, *J. Chem. Soc.* **1931**, 1456–1462.
- [35] A. Bard, L. Faulkner, *Electrochemical Methods*, John Wiley & Sons Inc., New York, **2012**.
- [36] M. A. Malik, P. J. Kulesza, R. Wlodarczyk, G. Wittstock, R. Szargan, H. Bala, Z. Galus, *J. Solid State Electrochem.* **2005**, *9*, 403–411.
- [37] M. C. Gallo, B. M. Pires, K. C. F. Toledo, S. A. V. Jannuzzi, E. G. R. Arruda, A. L. B. Formiga, J. A. Bonacin, *Synth. Met.* **2014**, *198*, 335–339.
- [38] J. Turkevich, P. C. Stevenson, J. Hillier, *Discuss. Faraday Soc.* **1951**, *11*, 55–75.
- [39] R. A. Timm, J. A. Bonacin, A. L. B. Formiga, H. E. Toma, *J. Braz. Chem. Soc.* **2008**, *19*, 287–292.
- [40] H. Gökce, N. Öztürk, M. Taşan, Y. B. Alpaslan, G. Alpaslan, *Spectrosc. Lett.* **2016**, *49*, 167–179.
- [41] J. A. Bonacin, A. L. B. Formiga, V. H. S. de Melo, H. E. Toma, *Vib. Spectrosc.* **2007**, *44*, 133–141.
- [42] F. S. Nunes, L. S. D. S. Bonifácio, K. Araki, H. E. Toma, *Inorg. Chem.* **2006**, *45*, 94–101.
- [43] S. A. V. Jannuzzi, B. Martins, M. I. Felisberti, A. L. B. Formiga, *J. Phys. Chem. B* **2012**, *116*, 14933–14942.
- [44] Z. Wang, H. Yang, B. Gao, Y. Tong, X. Zhang, L. Su, *Analyst* **2014**, *139*, 1127–1133.
- [45] P. C. Pandey, A. K. Pandey, *Electrochim. Acta* **2013**, *87*, 1–8.
- [46] L. Zhou, S. Wu, H. Xu, Q. Zhao, Z. Zhang, Y. Yao, *Anal. Methods* **2014**, *6*, 8003–8010.
- [47] W. Chen, S. Cai, Q.-Q. Ren, W. Wen, Y.-D. Zhao, *Analyst* **2012**, *137*, 49–58.
- [48] S. S. Kumar, J. Joseph, K. L. Phani, *Chem. Mater.* **2007**, *19*, 4722–4730.

- [49] L. Xu, G. Zhang, J. Chen, Y. Zhou, G. Yuan, F. Yang, *J. Power Sources* **2013**, *240*, 101–108.
- [50] C. Kent, J. J. Concepcion, C. J. Dares, D. Torelli, A. J. Rieth, A. S. Miller, P. G. Hoertz, T. J. Meyer, *J. Am. Chem. Soc.* **2013**, *135*, 8432–8435.
- [51] S. E. Hosseini, M. A. Wahid, *Renew. Sustain. Energy Rev.* **2016**, *57*, 850–866.
- [52] W. Wang, X. Xu, W. Zhou, Z. Shao, *Adv. Sci.* **2017**, *4*, 1600371.
- [53] B. Rohland, J. Nitsch, H. Wendt, *J. Power Sources* **1992**, *37*, 271–277.
- [54] A. Kudo, Y. Miseki, *Chem. Soc. Rev.* **2009**, *38*, 253–278.
- [55] J. D. Blakemore, R. H. Crabtree, G. W. Brudvig, *Chem. Rev.* **2015**, *115*, 12974–13005.
- [56] N.-T. Suen, S.-F. Hung, Q. Quan, N. Zhang, Y.-J. Xu, H. M. Chen, *Chem. Soc. Rev.* **2017**, *46*, 337–365.
- [57] M. E. G. Lyons, R. L. Doyle, M. P. Browne, I. J. Godwin, A. A. S. Rovetta, *Curr. Opin. Electrochem.* **2017**, *1*, 40–45.
- [58] M. B. Stevens, L. J. Enman, A. S. Batchellor, M. R. Cosby, A. E. Vise, C. D. M. Trang, S. W. Boettcher, *Chem. Mater.* **2017**, *29*, 120–140.
- [59] B. M. Hunter, H. B. Gray, A. M. Müller, *Chem. Rev.* **2016**, *116*, 14120–14136.
- [60] T. Reier, H. N. Nong, D. Teschner, R. Schlögl, P. Strasser, *Adv. Energy Mater.* **2017**, *7*, 1601275.
- [61] I. Roger, M. A. Shipman, M. D. Symes, *Nat. Rev. Chem.* **2017**, *1*, 0003.
- [62] Y. Gorlin, T. F. Jaramillo, *J. Am. Chem. Soc.* **2010**, *132*, 13612–13614.
- [63] I. Cesar, A. Kay, J. A. G. Martinez, M. Grätzel, *J. Am. Chem. Soc.* **2006**, *128*, 4582–4583.
- [64] M. W. Kanan, D. G. Nocera, *Science (80-. )*. **2008**, *321*, 1072–1075.
- [65] J. G. McAlpin, Y. Surendranath, M. Dinca, T. A. Stich, S. A. Stoian, W. H. Casey, D. G. Nocera, R. D. Britt, *J. Am. Chem. Soc.* **2010**, *132*, 6882–6883.
- [66] J. D. Blakemore, H. B. Gray, J. R. Winkler, A. M. Müller, *ACS Catal.* **2013**, *3*,

2497–2500.

- [67] J. R. Galán-Mascarós, *ChemElectroChem* **2015**, *2*, 37–50.
- [68] S. Goberna-Ferrón, W. Y. Hernández, B. Rodríguez-García, J. R. Galán-Mascarós, *ACS Catal.* **2014**, *4*, 1637–1641.
- [69] N. R. de Tacconi, K. Rajeshwar, R. O. Lezna, *Chem. Mater.* **2003**, *15*, 3046–3062.
- [70] L. Huang, X. Ge, S. Dong, *RSC Adv.* **2017**, *7*, 32819–32825.
- [71] C. Xuan, J. Wang, W. Xia, Z. Peng, Z. Wu, W. Lei, K. Xia, H. L. Xin, D. Wang, *ACS Appl. Mater. Interfaces* **2017**, *9*, 26134–26142.
- [72] S. Pintado, S. Goberna-Ferrón, E. C. Escudero-Adán, J. R. Galán-Mascarós, *J. Am. Chem. Soc.* **2013**, *135*, 13270–13273.
- [73] L. Han, P. Tang, A. Reyes-Carmona, B. Rodríguez-García, M. Torrens, J. R. Morante, J. Arbiol, J. R. Galán-Mascarós, *J. Am. Chem. Soc.* **2016**, *138*, 16037–16045.
- [74] B. Rodríguez-García, Á. Reyes-Carmona, I. Jiménez-Morales, M. Blasco-Ahicart, S. Cavaliere, M. Dupont, D. Jones, J. Rozière, J. R. Galán-Mascarós, F. Jaouen, *Sustain. Energy Fuels* **2018**, *2*, 589–597.
- [75] E. P. Alsaç, E. Ülker, S. V. K. Nune, Y. Dede, F. Karadas, *Chem. - A Eur. J.* **2017**, *24*, 4856–4863.
- [76] M. Aksoy, S. V. K. Nune, F. Karadas, *Inorg. Chem.* **2016**, *55*, 4301–4307.
- [77] Y. Surendranath, M. Dincă, D. G. Nocera, *J. Am. Chem. Soc.* **2009**, *131*, 2615–2620.
- [78] F. Zhao, Y. Wang, X. Xu, Y. Liu, R. Song, G. Lu, Y. Li, *ACS Appl. Mater. Interfaces* **2014**, *6*, 11007–11012.
- [79] Z. Gao, G. Wang, P. Li, Z. Zhao, *Electrochim. Acta* **1991**, *36*, 147–152.
- [80] Y.-H. Fang, Z.-P. Liu, *ACS Catal.* **2014**, *4*, 4364–4376.
- [81] R. O. Lezna, R. Romagnoli, N. R. De Tacconi, K. Rajeshwar, *J. Phys. Chem. B* **2002**, *106*, 3612–3621.

- [82] F. S. Hegner, I. Herraiz-Cardona, D. Cardenas-Morcoso, N. López, J.-R. Galán-Mascarós, S. Gimenez, *ACS Appl. Mater. Interfaces* **2017**, *9*, 37671–37681.
- [83] C. Jiang, S. J. A. Moniz, A. Wang, T. Zhang, J. Tang, *Chem. Soc. Rev.* **2017**, *46*, 4645–4660.
- [84] Y. Tachibana, L. Vayssieres, J. R. Durrant, *Nat. Photonics* **2012**, *6*, 511–518.
- [85] I. Cesar, K. Sivula, A. Kay, R. Zboril, M. Grätzel, *J. Phys. Chem. C* **2009**, *113*, 772–782.
- [86] Y. Park, K. J. McDonald, K.-S. Choi, *Chem. Soc. Rev.* **2013**, *42*, 2321–2337.
- [87] A. Kudo, K. Ueda, H. Kato, I. Mikami, *Catal. Letters* **1998**, *53*, 229–230.
- [88] B. Lamm, B. J. Trześniewski, H. Döscher, W. A. Smith, M. Stefik, *ACS Energy Lett.* **2018**, *3*, 112–124.
- [89] Z. F. Huang, L. Pan, J. J. Zou, X. Zhang, L. Wang, *Nanoscale* **2014**, *6*, 14044–14063.
- [90] Y. Liang, T. Tsubota, L. P. A. Mooij, R. van de Krol, *J. Phys. Chem. C* **2011**, *115*, 17594–17598.
- [91] H. Dotan, K. Sivula, M. Grätzel, A. Rothschild, S. C. Warren, *Energy Environ. Sci.* **2011**, *4*, 958–964.
- [92] T. H. Jeon, W. Choi, H. Park, *Phys. Chem. Chem. Phys.* **2011**, *13*, 21392.
- [93] P. A. Christensen, A. Harriman, P. Neta, M.-C. Richoux, *J. Chem. Soc. Faraday Trans. 1 Phys. Chem. Condens. Phases* **1985**, *81*, 2461.
- [94] Y. Yamada, K. Oyama, R. Gates, S. Fukuzumi, *Angew. Chemie Int. Ed.* **2015**, *54*, 5613–5617.